Title
Plasma Interactions and Electron Dynamics for Volumetrically Complex Materials

Author
Ottaviano, Angelica

Publication Date
2023

Peer reviewed|Thesis/dissertation

UNIVERSITY OF CALIFORNIA

Los Angeles

Plasma Interactions and Electron Dynamics for Volumetrically Complex Materials

A dissertation submitted in partial satisfaction
of the requirements for the degree
Doctor of Philosophy in Mechanical Engineering

by

Angelica Ottaviano

2023

ABSTRACT OF THE DISSERTATION

Plasma Interactions and Electron Dynamics
for Volumetrically Complex Materials

by

Angelica Ottaviano
Doctor of Philosophy in Mechanical Engineering
University of California, Los Angeles, 2023

Electron dynamics and plasma-infusion are crucial for understanding plasma and material recycling, cooling, and the plasma-material interactions (PMI) for plasma facing surfaces for applications such as fusion energy and space propulsion. Notably, we have shown that new materials such as volumetrically complex materials (VCMs) can improve plasma device performance and lifetime and may provide a versatile design space for plasma-facing components such as inner walls and high-power electrodes.

The objective of this dissertation is to investigate the key PMI of VCMs by examining and characterizing the effects of electron dynamics occurring at the near-surface plasma region with focus on SEE and ion-induced sputtering. This work uses a combination of experimental, computational, and analytical methods. Much of this work uses reticulated foams as a representative material architecture to investigate PMI behavior across a wide range of the VCM design space.

Secondary electron emission (SEE) yield analyses using a new scanning electron microscope (SEM) method revealed up to 43% suppression from foam compared with flat. Foam ligament-to-pore aspect ratio showed the presence of an optimal geometric configuration, which is in agreement with current and past analytical models. Using SEM techniques, the importance of sample trans-

parency and backplate yield contributions on overall target yield in plasma-facing regimes was also established. These results showed that geometric transparency can be used to assess the effective transparency to plasma species. Angular dependence revealed multi-scale behavior in that foams with um features exhibit loss of angular dependence much like fuzzes, while large foams (mm) are directional much like fibers and velvets. Electron spectroscopy showed that backscattered electron suppression is 80% more than low energy SEE suppression in carbon foams, while low energy SE generation may be enhanced. An analytical model for ion-sputtering of foams was modified to employ SEE physics and calculate SEE yields, which were then compared with experimental results.

A dedicated, compact, hollow-cathode generated plasma facility was developed to expose biased foam (100 – 600 V) to investigate plasma infusion regimes using electrostatic probing, optical emission spectroscopy, and in-situ sputter yield monitoring. A new diagnostic developed for real-time and in-situ surface profilometry is used to monitor the surface morphological evolution of foams during plasma exposure. Combined with ex-situ surface analysis techniques, plasma-foam experiments and analysis of inter-foam deposition and sputterant transport within pore layers have shown that plasma infusion is key for predicting back vs forward material sputtering. In addition, user facility was used in a collaboration project with UCLA Physics to investigate the effect of biased tungsten foams in a pulsed He plasma on material erosion and arcing in comparison with a planar surface. It was found that tungsten-based VCMs can withstand up to 600 V negative bias in a continuous and pulsed plasma environment, with significant reduction of arcing events when comparing to planar tungsten.

The dissertation of Angelica Ottaviano is approved.

Yevgeny Raitses

Troy A. Carter

Jaime Marian

Artur Davoyan

Richard E. Wirz, Committee Chair

University of California, Los Angeles

2023

$\pi\lambda\alpha\sigma\mu\alpha$: (Greek) to form, to mold.

To my friends, family, and pasta: the things which have formed and molded me.

TABLE OF CONTENTS

List of Figures

List of Tables

ACKNOWLEDGMENTS

I would first like to thank my PhD advisor, Professor Richard Wirz for his guidance, support, encouragement, expertise and mentorship. Thanks to you I have been able to learn much more than I ever expected outside of pure research and coursework: from participating in proposal writing and assisting with undergraduate course teaching, to being a more confident presenter. Your passion for plasma technologies, aerospace engineering and infusion of modeling with experimental techniques has provided me with a unique skill set which I will benefit from for my entire career.

I would also like to thank external mentors and my doctoral committee: Dr. Yevgeny Raitses, who has been believing in me since well before graduate school, infecting me with vigour (and rigour) for all things interesting, and teaching me how to be a better physics researcher along the way. Professors Bruce Koel and Troy Carter have also been fundamental support to my success and boundless sources of expertise in surface science and plasma physics. Their kind disposition has been a leading example for my personal growth. Professors Jaime Marian and Artur Davoyan have graciously kept up with my work throughout the years at UCLA, and have provided me with invaluable insights along the way. Collaboration has always been the key to my success.

Next I would like to thank my family: Mom, Papà, Daisy, my grandparents Nonna Paola, Nonno Vittorio, Noni, and Nonno Tito, as well as the rest of the Ottaviano-Masoni clan. I would be nowhere near where I am now without my family. Thank you for letting me bore you to death with infinite phone calls about plasma, fusion, and propulsion while adding spice (and space!) to your lives with my many ups and downs.

My most heartfelt gratitude goes out to my lab cohort: Anirudh Thuppul, Mary Konopliv, Patrick Crandall, Gary Wan, Stephen Samples, Adam Collins, Nolan Uchizono, Peter Wright, Gary Li, Graeme Sabiston, Henry Huh, Phil Travis, Thomas Look, McKenna Davis, and the rest of the comrades at the Princeton Plasma Physics Laboratory, including Tasman Powis, Shota Abe, Willca Villafana, and Evan Ostrowski. Lab shenanigans have been at the very core of surviving this PhD

experience, especially during the infamous year of 2020. I would also like to thank the countless technicians and undergraduate students who have helped, as well as my former co-workers at TAE Technologies for their support.

I wish to thank Dino Orucevic with his unwavering love and unparalleled patience, as well as his special family. My dear friends who are far and near have always supported me, put up with me, immensely enriched me, and because of them I continue to become a more grounded, aware, and serene academic researcher. My friends always remind me that I have home outside of geographical bounds. This certainty helps me survive incredible distances.

Lastly, I'd like to wish a special thank you to the women in the field who have inspired and helped me accomplish this degree: Tania Schindler, my former supervisor and laser-guru at TAE Technologies, Mary Konopliv, my partner in nerdism, dance, fluid-dynamics, plasma physics, conferences, travel, Russian language classes, fashion choices, adventures and beyond, Prof. Angela Capece (TCNJ) and Dr. Marlene Patino (UCSD) for laying down so much groundwork in the field of SEE, and Prof. Donna Sheng with Prof. Ana Cadavid (CSUN) who started me on this journey. You are all wonderful, top quality people and incredible scientists!

Inoltre e infine, dedico questo lavoro alla famiglia, ai parenti, e agli amici in Italia. Sopratutto alla mia Nonna Paola (Jones) che per me è un'estrema forza della natura ed esempio di bontà, di grinta, di buon appetito, di voglia di vivere nel vero senso di *vivere*... e di grande *fortuna* con le pinelle! La Nonna Paola, la quale mi ha ospitato per completare la fase finale di scrittura durante un'avventurosa ma meravigliosa primavera romana circondata da piccioni, caffè, risate, dolcezze, pasta, porchetta, carciofi, papaveri, amici, e gli amati zii Silvia e David. Papà: adesso potrò andare finalmente a lavorare alla fabbrica dei Plasmon!

Funding: UCLA, ARPA-E U.S. Department of Energy (Award No. DE-AR0001378)

VITA

2014	Intern at Deutsches Elektronen-Synchrotron DESY, Hamburg
2014-2015	Undergraduate DOE fellow, Princeton Plasma Physics Laboratory
2016	B.S. Physics, California State University, Northridge
2017	Intern at the Swiss Plasma Center, Lausanne
2018-2020	Diagnostic Specialist, TAE Technologies Inc.
2020-2022	Jr. Scientist, TAE Technologies Inc.
2018-2023	Graduate Student Researcher, UCLA
2020	M.S. Mechanical Engineering, UCLA
2021	Teaching Assistant, MAE 161B Space Technologies, UCLA
2022-2023	Visiting Graduate Student, PCRF Grant, Princeton Plasma Physics Laboratory

PUBLICATIONS

A. Ottaviano Y. Raitses, E. Ostrowski, G. Wan, S. Abe, B. Koel and R. E. Wirz, *Direct measurement and spectroscopic analysis of secondary electron suppression mechanisms from non-planar surfaces.* In Preparation (2023) .

A. Ottaviano, R. E. Wirz, *Secondary electron emission of reticulated foam materials.* Journal of Applied Physics 133.10 (2023):103302

A. Ottaviano, A. Thuppul, J. Hayes, C. Dodson, G. Z. Li, Z. Chen, & R. E. Wirz, *In situ microscopy for plasma erosion of complex surfaces.* Review of Scientific Instruments, 92(7), 073701 (2021)

A. Ottaviano, S. Banerjee, and Y. Raitses. *A rapid technique for the determination of secondary electron emission yield from complex surfaces.* Journal of Applied Physics 126.22 (2019): 223301

A. Ottaviano, T. M. Schindler, K. Zhai, E. Parke, E. Granstedt, M. C. Thompson, TAE Team, *Characterization and calibration of the Thomson scattering diagnostic suite for the C-2W field-reversed configuration experiment.* Review of Scientific Instruments 89.10 (2018): 10C120

C., Jin, A. Ottaviano, Y. Raitses, *Secondary electron emission yield from high aspect ratio carbon velvet surfaces.* Journal of Applied Physics, 122(17), (2017) 173301.

CHAPTER 1

Introduction and Motivation

The following chapter outlines the importance of the general research area of the dissertation: plasma-material interactions. The main applications are magnetic confinement fusion and electric propulsion, although other motivations are also described.

1.1 Plasma-Material Interactions

The field of plasma-material interactions (PMI) is a growing area of research which has proven to be critical to improving the performance of plasma devices and prolonging their lifetimes. In some cases, solving PMI-related challenges may be enabling to break-through advances in advanced fusion energy concepts. For magnetic confinement fusion, ion-induced sputtering and the associated component erosion can deteriorate plasma conditions and limit device lifetime by affecting limiters or divertor regions where plasma ions are in contact with a material surface [10, 11, 12, 13, 14] . For both applications, the reintroduction of sputtered material into the bulk plasma can also lead to increased impurities and contamination that reduces the overall device performance and efficiency [15, 16, 17]. To withstand the extreme conditions to which plasma-facing components are subjected to, novel types of materials and surfaces must be developed, understood, and optimized. Volumetrically complex surfaces (VCMs) have recently been shown to have unique properties in plasma environments, such as maintaining sustained reduced sputter yield and geometrically reduce SEE [18, 9]. Figure 1.1 summarizes the ion and electron interactions on a plasma-facing surface relevant to this work.

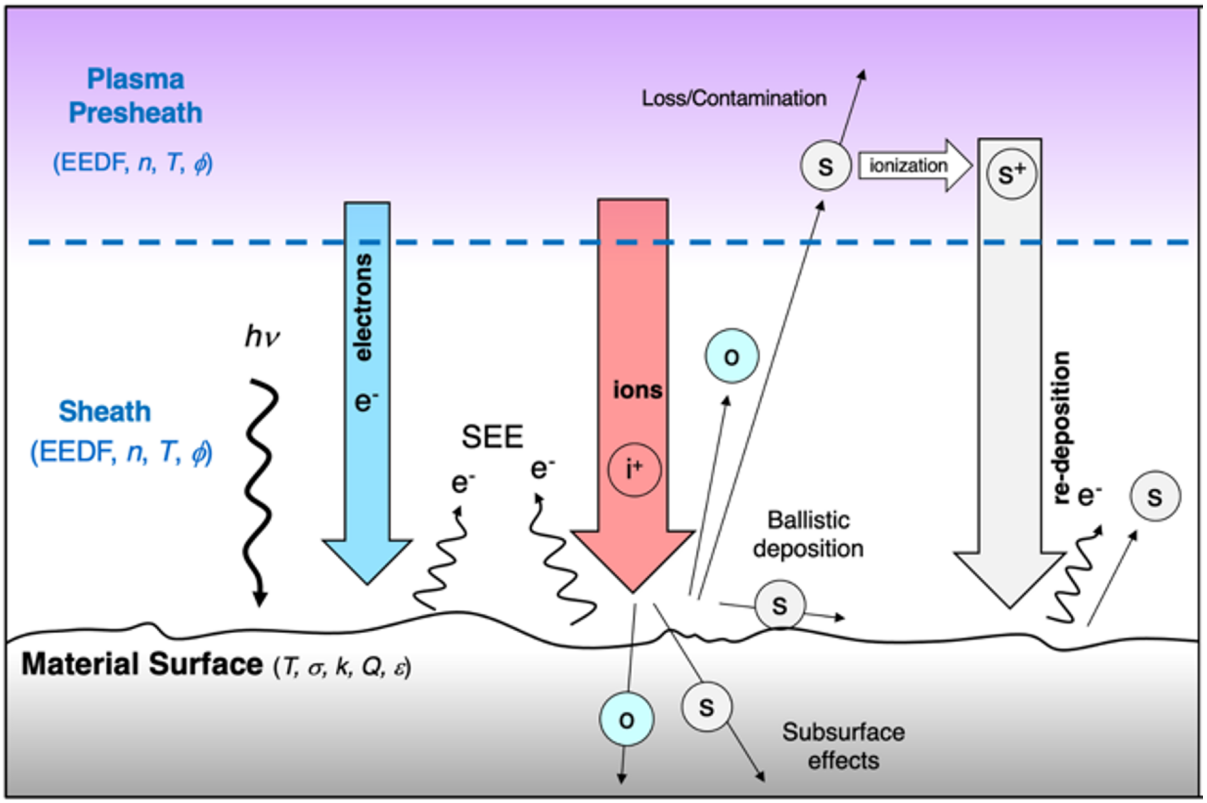

Figure 1.1: Main surface and sub-surface interactions for materials in plasma environments of interest to the work presented in this document.

Complex featured surfaces have recently been studied for their low sputtering yield and reduced secondary electron emission (SEE) properties due to the trapping of emitted particles in their cavities [19, 20, 21, 22, 23, 24]. Complex surfaces include velvets, nano-fuzz formations, fractal-feathered surfaces, grooves, and volumetrically porous VCMs of materials such as tungsten, graphite, carbon, or molybdenum. These complex surfaces exhibit only temporary sputter yield reduction [25, 26]. In contrast, VCMs have recently been demonstrated as an attractive option for plasma-facing surfaces due to their ability to exhibit persistent sputter yield reduction [18, 17]. This persistent yield reduction is due to the volumetrically complex structure of VCM that continually presents a complex surface geometry to the plasma even after tens of hours of plasma exposure. Additionally, VCMs can exhibit a plasma-infused regime where the plasma at least partly infuses into the VCM and exhibits unique sputtering behavior [27].

1.2 Motivation and Potential Impact

The performance of plasma-facing materials is strongly correlated to the ejection of atoms and electrons from their surfaces. Unlike other materials with complex surface structures, such as fuzzes or featured solid surfaces, where the trapped elements sputter away during plasma exposure, VCMs maintain structural complexity and exhibit a sustained sputter yield reduction.. VCMs undergoing ion bombardment deposit and redeposit sputterants onto the structure itself, reducing mass loss rates and contamination of the surrounding plasma, while possibly mitigating PMI-driven instabilities, material erosion and degradation, plasma contamination, and bulk plasma cooling.

SEE yield from VCMs has previously been evaluated using scanning electron microscopy [28], where the qualitative results have shown a reduction in yield up to $\approx$4%, in agreement with theoretical findings [29, 23, 4]. Further SEE yield experiments at the Low Temperature Plasma Research Facility would allow for direct comparison of different materials and VCM geometries scanned across a wide primary electron energy range (10 - 1000 eV), thus providing crucial information for a complete model on SEE through complex structures.

In addition to investigating SEE yield as a function of surface geometry, this research proposes to characterize the evolution of SEE yield through the lifetime of a plasma-facing material. This is of high importance to the plasma community because significant changes to SEE yields over time may affect plasma sheath behavior, thus changing the fundamental performance of certain plasma-facing components. Full understanding of electronic response within porous materials can offer numerous promising capabilities towards many areas of plasma-related technology including, but not limited to fusion energy, space propulsion, space environment, materials processing, particle accelerator, and multipactor effect research. Recent advances in manufacturing VCMs from refractory metals make VCMs attractive candidates for fusion energy applications for cooling, and general self-healing purposes [10, 30, 31].

By characterizing the electron emission behavior of VCMs, it will also be possible to better understand plasma sheath physics and ion sputtering from VCMs, as these are dynamic and in-

terrelated processes. This would be the first demonstration of the effect of a material's complex surface evolution under plasma ion bombardment on its SEE yield. Figure 1.2 shows the dynamically interrelated SEE and ion sputtering processes of PMI. Immediate applications of this research include:

- Development of advanced fusion materials and high-power electrodes
- Robust electrodes for high thrust in-space propulsion concepts
- Novel electrodes for battery technologies and fuel cells
- Plasma-facing components in non-fusion applications
- Plasma material processing
- Radiofrequency components to mitigate multipacting effect
- Particle accelerator components

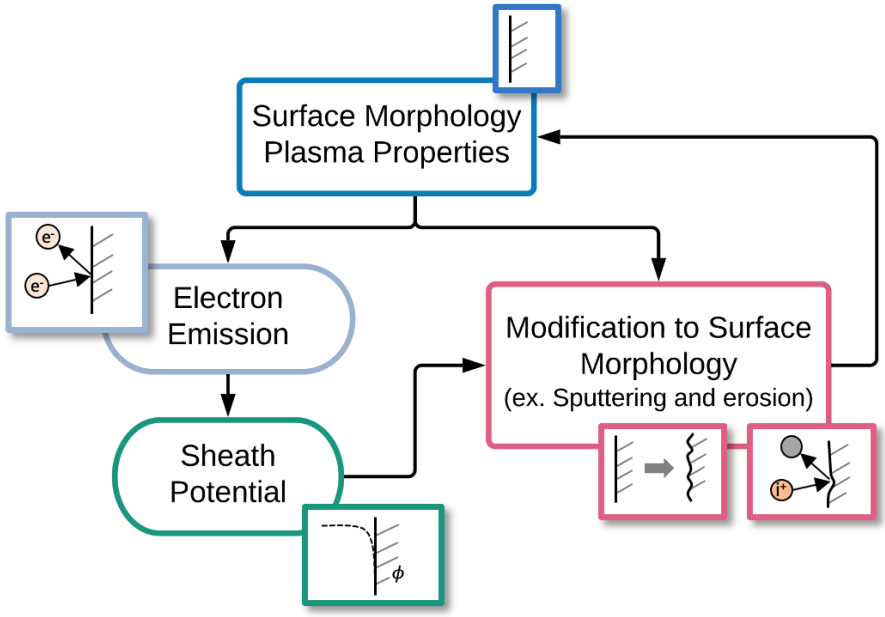

Figure 1.2: Dynamic and interrelated processes of PMI research include SEE, ion-induced sputtering, sheath modification and surface evolution of a plasma-facing material.

It is important to make the distinction between sputtering and erosion: sputtering is the mechanical removal and ejection of surface atoms due to momentum exchange between incoming particles and the material surface, while erosion is the measure of surface recession of a material during sputtering. A grooved surface for example may have low sputtering yield compared to a planar surface due to particle trapping in the surface features, but the erosion rate or surface recession may be the same as that of a planar surface.

Careful material engineering may enable the miniaturization of conventional electric propulsion (EP) devices (e.g. Hall-effect thrusters), as well as the development of high-power and advanced thruster concepts (e.g. magnetoplasmadynamic thrusters and nuclear fusion propulsion). Recent studies have successfully demonstrated self-healing of materials in conditions representative of those found in plasma thrusters [32, 33, 30, 34]. Self-healing is the ability of a materials to restore its original structural integrity after damage in response to changes in the operating regime,

which does not disturb the working capacity of the system. Plasma has also been shown to nucleate nano- and micro- particles directly in the discharge. Direct synthesis and deposition of complex nanostructures (e.g. carbon nanotubes, graphene, and nanoflakes) have been demonstrated in Hall thruster-like plasma conditions [35].

Another important aspect of PMI research for EP purposes is the investigation of facility effects. Secondary electrons emitted from chamber walls and electron transport of these electrons are a common issue in EP testing as they may suppress instabilities and enhance thrust measurements [36]. Sputtering of chamber wall materials is also an unwanted PMI facility effect as deposited materials can alter the diagnostic sensitivities and resulting measurements and lead to the deposition of conductive coatings on dielectric surfaces. PMI is not only important for the effects of ejected particles from wall materials, but also in the design and development of effective beam dump materials for slowing down ions. In electrospray thrusters, PMI chemistry is very important, specifically SEE due to ion and complex molecule interactions with walls, diagnostics, beam dumps, accelerator and extractor grids. This can limit and degrade the performance of electrospray thrusters. Secondary electrons can neutralize and degrade the propellant as they back-stream to the emitter as well as alter the plume potential profile [14].

1.2.1 Complex Surfaces in Plasma-Material Interactions

It has been shown that materials with complex nano-, micro- and even mm-sized features can reduce both SEE and ion-induced sputtering by trapping emitted particles in the regions between their cavities. These materials include fibrous velvets, grooved surface, irregularly roughened surfaces and porous surfaces [24, 37, 38, 4, 39, 40]. Jin et al [41] showed experimentally that the SEE yield of carbon velvets are reduced by up to 65% compared with a planar surface, and Huerta et al [38] have shown that a porous material can also reduce SEE yield values by up to 75% compared with a planar surface via a trapping mechanism. Li et al [42, 43] showed that micro-architectured molybdenum surfaces have a sputtering yield reduced by 45% compared with a planar surface, but approached the planar surface value as the features were eroded away. For this

reason, volumetrically porous materials have been recently considered. By having a volumetrically structured bulk material, the sputtering reduction by geometric means is distributed throughout the interior of the material as opposed to being isolated on the surface. In addition, sputtering occurring inside the VCM mesh network causes non-linear sputtering deposition processes that may provide a lower thickness erosion rate. Previous computational work with high energy sputtering of nano-VCMs has predicted an effective sputtering yield reduction [44].

As thruster research trends towards higher powers (100 kW to 10 MW) and advanced concepts such as MPD thrusters and fusion thrusters, the need for renewable electrode systems increases. At high temperatures and current densities, the recycling of evaporated and sputtered cathode material in the plasma becomes important. Sputtered atoms and molecules are ionized in the near-cathode plasma and then return as ions to the cathode followed by surface recombination. This cycle then may repeat itself resulting in an active ion recycling system. In the case when the recycling of high vapor pressure materials in the plasma is less than 100%, the material losses could be replenished by feeding liquid metal through the cathode by using materials such as lithium or tin and a porous material to flow the liquid through. Volumetrically porous VCMs therefore are ideal structures for studying not only reduced SEE and sputtering yield, but also for flowing liquid metals through to develop renewable cathode concepts. Figure 1.3 shows the erosion, deterioration and flaking of a complex surface undergoing ion bombardment. Figure 1.4 shows different complex surfaces with varying features sizes studied in recent years as plasma-facing surfaces.

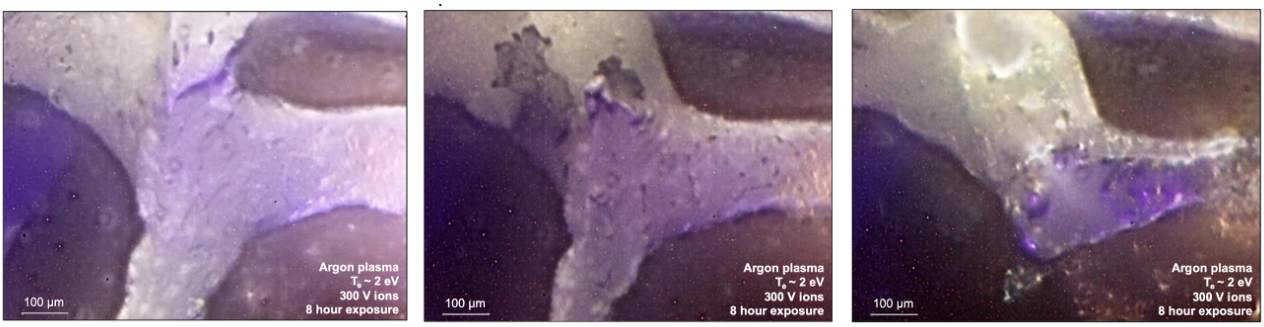

Figure 1.3: Surface erosion of an aluminum VCM ligament captured via long distance microscopy at UCLA [1]

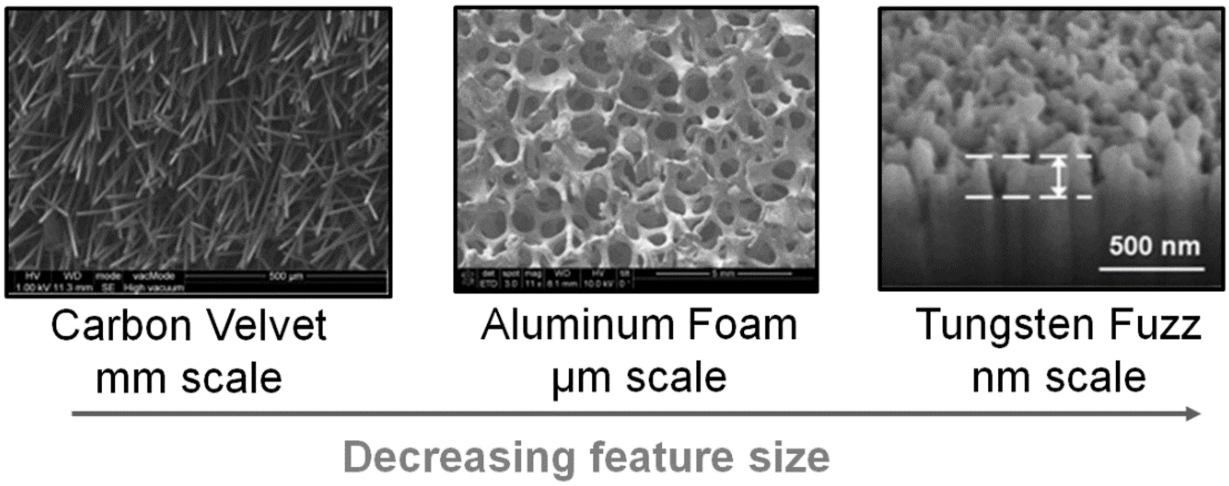

Figure 1.4: Examples of complex surfaces in PMI research: SEM images of carbon velvet, VCM VCM and tungsten fuzz surfaces researched for their SEE reduction and sputter yield reduction properties.

1.3 Dissertation Overview

The remainder of this dissertation is organized as follows: a brief overview of relevant theory which includes the fundamentals of SEE and the basic physics of plasma sheaths. A following section then describes the experimental facilities used so far in this research, including the Plasma-interactions facility at UCLA and the ongoing commissioning of the new Materials Observation and Characterization facility. A novel diagnostic which uses long distance microscopy for in-situ plasma-surface erosion visualization will also be described in the experimental facility section. This section is an adaptation of the recent publication [1]. Next, a section dedicated to the study of SEE from carbon VCM surfaces will describe the methods and highlight results of SEE reduction and geometric trends found using SEM [6]. A fifth chapter will briefly outline two demonstration experiments for plasma infusion and plasma-material transport within VCM surfaces due to partial plasma infusion. Lastly, a summary and future work chapter will include relevant applications and directions for this research in the field of PMI.

CHAPTER 2

Theory

Much of the PMI occurring between a VCM and charged particles or a plasma is dictated by the naturally forming electrostatic sheath at the VCM surface. In some cases, a sheath may be thin compared to the VCM structure and thus conform to its ligaments and allow for some degree of plasma infusion. In this case, in the absence of a magnetic field, ions or electrons are presumed accelerate into the sheath with normal incidence to the VCM surface [45, 46]. If the sheath is very large compared to the VCM geometric structure, then the plasma can be considered as *VCM-facing*, and charged particles are presumed to have oblique incidence almost everywhere on the VCM surface.

The sheath potential and thickness depends on plasma properties, the applied material potential, and particle emissive properties such as SEE [47, 48, 31, 49]. This chapter summarizes the key governing equations for plasma sheaths with particular emphasis on the sheath thickness, L_s, for different PMI configurations, as well as the fundamental theories of SEE. In addition, preliminary theory on plasma infusion through a VCM is detailed in chapter, along with a summary of useful VCM and foam material properties and definitions.

2.1 Plasma sheaths and Debye shielding

Plasma sheaths form at the boundaries between a plasma and a surface due to particles entering and leaving the the plasma device via energy exchanges of the charged species. A plasma will automatically satisfy either particle balance in the case of a floating surface in the plasma, or elec-

trical boundary conditions imposed on the surface in the case of a biased surface. This leads to an electrostatic potential structure to be established to satisfy conditions near the wall, and is referred to as the *sheath* [50]. In practical plasma applications such as ion and Hall-effect thrusters [14], magnetic confinement fusion devices, and low-temperature plasma processing, it is important to be able to calculate the sheath potential structure as it provides the directed wall energy necessary to maintain and improve each application's performance. In the semi-conductor industry for example, the sheath potential can be used as a control for etching and altering the surface of the target material [51] [49]. In magnetic confinement fusion, the plasma-wall interaction is crucial for understanding particle and energy exhaust, recycling and transport. In a variety of plasma experiments, intrusive probes such as Langmuir probes, emissive probes and energy analyzers rely on controlled biasing schemes and the measured electrostatic response of the probe to the plasma. The sheath is crucial because it is the main mechanism via which the plasma ion and electron populations interact with materials. In addition, plasma sheaths are also important in understanding the interaction between space or astrophysical plasmas and objects such as spacecraft and spacecraft diagnostics [52].

Modifying the surface structure or electrostatically biasing material which confines the plasma will cause a modification of the sheath potential [29]. In some practical applications, it is important to account for and appropriately minimize unwanted effects occurring at the walls which can lead to rapid material erosion and reduced device lifetimes, or to reduced performance of the plasma bulk [15]. One of these processes is the emission of electrons from the plasma-facing surface, which can occur both in the case where a material has a significant secondary electron emission yield, or when the material is thermionically emissive [49] [21]. While the very basic properties of ion sheaths are well-established, this chapter will also will analyze the type of sheath generated at a biased electrode surface.

The Debye length in a plasma is the characteristic screening length of electrostatic fields from charges introduced into a plasma. It can be derived by considering a small positive charge, q, in a quasi-neutral plasma where $n_i \approx n_e \approx n_0$. Without a plasma, potential at a distance r from the

charge is $\phi = q/4\pi\varepsilon_0 r$. In a plasma however, electrons and ions in the vicinity respond proportionally to their respective densities and velocities. The electron distribution function with kinetic and potential energy in the presence of a $q\phi$ can be written as:

$$n = \int exp\left(\frac{-\frac{1}{2}mv^2 + q\phi}{k_B T_e}\right) dv_x dv_y dv_z. \tag{2.1}$$

By integrating over v, setting $q = -e$ and applying the limit of $n_e(\phi = 0) = n_0$ yields:

$$n_e = n_0 \exp\left(\frac{e\phi}{k_B T_e}\right) \tag{2.2}$$

which is also known as the *Boltzmann distribution* for electrons. Poisson's equation in one dimension is

$$-\nabla^2\phi = \frac{\sigma}{\varepsilon_0} = -e(n_i - n_e). \tag{2.3}$$

By combining these equations and assuming inertia prevents ions from moving significantly so that $n_i = n_0$, Poisson's equation can be written as:

$$\varepsilon_0 \frac{d^2\phi}{dr^2} = en_0\left[\exp\left(-e\phi/k_B T_e\right) - 1\right]. \tag{2.4}$$

Considering the region where $e\phi/k_B T_e \ll 1$ and applying a Taylor expansion the the exponential, the linear terms in 2.4 have solution

$$\phi = \frac{e}{4\pi\varepsilon_0 r} \exp\left(-\frac{r}{\lambda_D}\right) \tag{2.5}$$

where the characteristic Debye length is defined as:

$$\lambda_D = \sqrt{\frac{\varepsilon_0 k_B T_e}{n_0 e^2}}. \tag{2.6}$$

From classic electrostatics, the term of the Debye potential is recognized as the potential due to a test point charge at a radial distance r while the exponential term describes the plasma response to the test charge [50]. Thus, the potential due to a test charge in a plasma falls away exponentially and the plasma shielding is quite effective Detailed derivations of the Debye shielding effect and the Debye potential can be found across many sources such as in Ref: [50, 14].

2.1.1 Floating surfaces

The simplest sheath case occurs for a floating or unbiased surface facing a plasma. Debye shielding allows for the bulk of a plasma in contact with its container to generally be at a constant potential (*plasma potential*). Because the ion mass is at least two orders of magnitude larger than electrons, there is significant mobility between the two charged species, and electrons will make more collisions with a boundary than ions initially. The bulk plasma will be left with a net positive charge and the wall potential ϕ_w becomes negative with respect to the plasma potential. Ions are then attracted to the wall until equilibrium is established between ion and electron flux. The potential drop at the wall is generally a few times the Debye length and is a space-charge layer known as the plasma sheath. Assuming that ions enter a floating wall sheath at $x = 0$ with an initial velocity v_0, and assuming a collisionless sheath, then conservation of energy requires:

$$\frac{1}{2}m_i v_i^2 = \frac{1}{2}m_0^2 - e\phi(x) \tag{2.7}$$

and ion continuity

$$n_0 v_0 = n_i(x)v_i(x). \tag{2.8}$$

Combining energy conservation and ion continuity gives an expression for the ion density in the sheath:

$$n_i(x) = n_0 \left(1 - \frac{2e\phi}{m_i v_0^2}\right)^{1/2}. \tag{2.9}$$

Poisson's equation is combined with the Boltzmann distribution for electrons to yield a generalized sheath equation:

$$\varepsilon_0 \frac{\partial^2 \phi}{\partial x^2} = e(n_e - n_i) = e n_0 \left[\exp\left(\frac{e\phi}{k_B T_e}\right) - \left(1 - \frac{2e\phi}{m_i v_0^2}\right)^{-1/2}\right]. \tag{2.10}$$

By applying the condition that the sheath potential must be monotonic, that $e\phi \ll k_B T_e$ and that $\phi < 0$, the equality known as the Bohm sheath criterion is derived:

$$v_i > \sqrt{\frac{k_B T_e}{m_i}} \tag{2.11}$$

where $v_B = \sqrt{\frac{k_B T_e}{m_i}}$ is the ion Bohm velocity, or its sound speed. v_B is the minimum ion velocity required to enter the sheath. The pre-sheath is a small quasi-neutral region where ions are accelerated to this speed.

At a floating wall, the incident ion and electron fluxes must balance each other, and in the sheath, the ion flux is considered to be constant and given by $\Gamma_i = n_s v_B$ where n_s is the density at the boundary of the sheath. Equating electron and ion fluxes at the wall with the mean electron speed $v_e = \left(\frac{8k_B T_e}{\pi m_e}\right)^{1/2}$, the ion Bohm velocity and the electron Boltzmann density distribution yields:

$$n_s \left(\frac{kT_e}{m_i}\right)^{1/2} = \frac{1}{4} n_s \left(\frac{8k_B T_e}{\pi m_e}\right)^{1/2} \exp\left(\frac{e\phi_w}{kT_e}\right). \tag{2.12}$$

Solving for the wall potential gives the floating wall sheath potential

$$\phi_w = -\frac{k_B T_e}{e} \ln \sqrt{\frac{m_i}{2\pi m_e}}. \tag{2.13}$$

The floating wall potential is negative with respect to the bulk plasma, and is linearly proportional to the plasma electron temperature, and proportional to the ion-electron mass ratio. For many ion species, it can be found that the floating wall sheath is a few times the Debye length. For example in an argon plasma, $L_s \approx 5\lambda_D$.

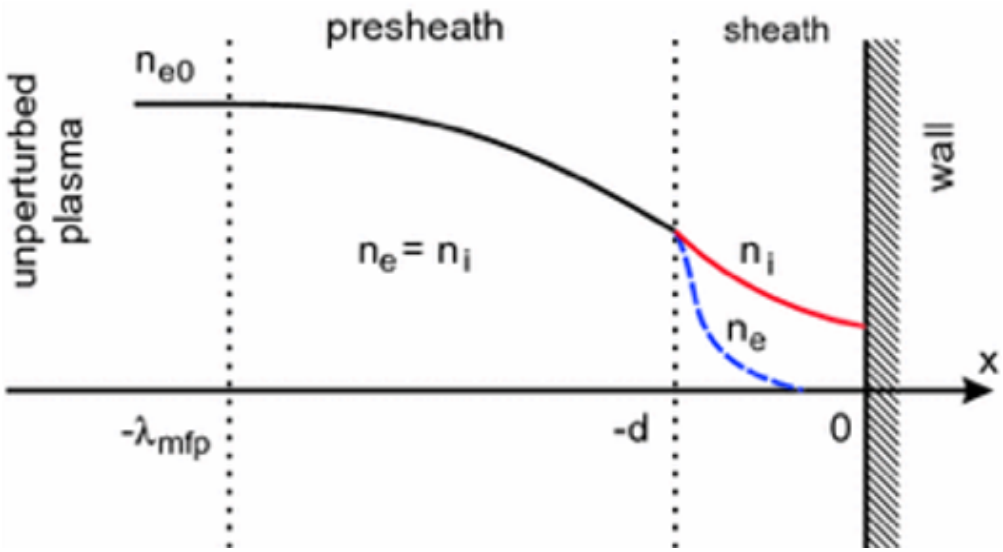

Figure 2.1: The electrostatic sheath structure at a material boundary showing the reduction of potential through a pre-sheath region and the sheath, as well as the difference in ion and electron densities near the wall [2].

2.1.2 Child-Langmuir Sheaths

Plasma boundaries can also be biased at some potential, V. Anodes collect net electron current, while cathodes collect net ion current. Biased sheaths are normally negative in order to reduce the electron flux, while positive sheaths (or electron sheaths) that sit above the plasma potential exist but are rare in their application. Other types of sheaths and sheath phenomena are the anode double layer, or *fireballs*. These are electron sheaths with a large positive bias which have been observed to produce a secondary discharge brighter than the surrounding plasma. Fireballs are believed to occur by an increased ionization near the electrode due to the acceleration of fast electrons into the sheath. Cathode sheaths instead often form double layers, which occur when there is a high

electron current flow as well as ion flow. This type of sheath will be described in more detail in the following section [49].

If the potential across a sheath is large enough to repel any electrons over the length of the sheath thickness $\phi_s >> k_B T_e/e$, then an ion sheath will form. In this sheath, the electron density is zero and there is no effect of electron space charge on the sheath thickness. The ion current density will then be given by

$$J_i = n_i e v_i = n_i e \sqrt{\frac{2e}{m_i}} [\phi_0 - \phi]^{1/2} \tag{2.14}$$

where ϕ_0 is the sheath potential at its edge. By solving Equation 2.14 for n_i and integrating Poisson's equation without any electron density contribution, and multiplying each side by $d\phi/dx$ it can be found that

$$\frac{d\phi}{dx} = 2\sqrt{\frac{J_i}{\varepsilon_0}} \left(\frac{m_i(\phi_0 - \phi)}{2e} \right)^{1/4}. \tag{2.15}$$

Integrating the above equation once more, and indicating ϕ_w as the voltage across the sheath, or the wall potential, and d as the sheath thickness, the Child-Langmuir Law is found:

$$J_i = \frac{4\varepsilon_0}{9} \sqrt{\frac{2e}{m_i}} \frac{\phi_w^{3/2}}{d^2}. \tag{2.16}$$

By applying the Bohm velocity sheath criteria for ions at the edge of the pre-sheath [49], and applying charge continuity and particle force balance at the sheath edge, the Child-Langmuir sheath thickness L_s can also be found in terms of the Debye length for an ion sheath:

$$L_s = \lambda_D \frac{\sqrt{2}}{3} \left(\frac{2e\Delta\phi_s}{T_e} \right)^{3/4}. \tag{2.17}$$

This result suggests that the sheath can be on the order of the Debye length for floating or small wall potentials, but scales nearly linearly with surface bias. The sheath potential itself drops as a

function of the global current balance.

If a surface is positively biased and the electron field is directed from the electrode towards the plasma, an electron sheath may form. In this lesser examined case, an electron Bohm criterion is associated with the electron sheath, where the electron flow speed v_e must satisfy

$$v_e \gg v_{e,B} \tag{2.18}$$

and where $v_{e,B} \approx \sqrt{k_B T_e / m_e}$. This condition is normally satisfied by the electron flux associated with a part of the electron velocity distribution function near the edge of an electron sheath [49, 53], and a pre-sheath is not always necessary. A two-fluid approach similar to the ion sheath derivation can be used to derive the electron sheath potential, assuming there is no ion density in the sheath, and that the sheath is weakly or non collisional. Thus, electrons are assumed to traverse ballistically into the sheath, and by using the usual combination of current balance and Poisson's equation, the Child-Langmuir law can be found for an electron sheath:

$$J_{e,0} = \frac{4}{9}\sqrt{\frac{2e\varepsilon_0}{m_e}}\frac{\Delta\phi_w^{3/2}}{x^2}. \tag{2.19}$$

where $J_{e,0}$ is the electron current density at the sheath edge. The sheath thickness is the same as for an ion sheath.

These two biased wall sheath formulations are important for evaluating and predicting plasma infusion conditions in electrode studies of VCMs.

2.1.3 Double cathode sheaths: ion and electron current fractions

The double sheath structure arises when a cathode plasma-facing surface is emitting electrons. In this case, if the sheath potential is much larger than the cathode temperature, the electrons can be considered cold and emitted with zero velocity. The resulting sheath will be affected by the cathode side as well as the plasma side which contains a distribution of ion velocities as well as plasma

electrons entering the sheath. In ion and Hall-effect thrusters it is common at the cathode and at the accelerator region to have such a scenario where ion and electron currents flow between the plasmas, leading to a double sheath boundary. The double sheath refers to a region where electron space charge dominates one half and ion space charge dominates the other half. At the electron emitting surface, electrons flow from zero-potential to the opposite boundary at a potential ϕ_s. The acceleration of the charged particles through the plasma sheath causes local space-charge effects, thus reducing the electric field at both boundaries. The resulting total spatial variation across the sheath between the two plasma boundaries is larger than the vacuum solution where there is a linear potential variation between the two potentials. The qualitative potential structure is shown in 2.1.

A useful calculation for understanding the relation between the ion and the electron currents in a double-sheath is made by considering momentum balance. Ions are assumed to arrive at the sheath boundary with the Bohm energy of $k_B T_e/2$ and the associated current density $n_p e\sqrt{k_B T_e/m_i}$ where n_p is the charged particle density at the boundary between the sheath and the plasma. The plasma surface is considered to be solid, and electrons have a Maxwellian distribution. The total pressure on the plasma surface is made of the following terms: the ion injection recoil, the pressure due to the Maxwellian electrons, and the momentum of the electrons emitted from the cathode. By balancing equal and opposite forces and assuming that the sheath potential is much larger than the electron temperature ($kT_e/2e\phi_s << 1$), it is found that

$$J_i\left(1+\frac{k_B T_e}{4e\phi_s}\right)-J_i\sqrt{\frac{2k_B T_e}{e\phi_s}}-J_e\sqrt{\frac{m_e}{m_i}}=0 \tag{2.20}$$

and by applying the above assumptions,

$$\frac{J_e}{J_i}=\sqrt{\frac{m_i}{m_e}}\left(1-\sqrt{\frac{2k_B T_e}{e\phi_s}}\right). \tag{2.21}$$

Furthermore, enforcing a positive solution for the electron to ion current ratio leads to the condition

that $\phi_s > 2kT_e/e$. This result deviates significantly from the case of a double sheath with no emitted particle velocity. For no electron velocity, the total momentum balance equation only contains the force on the cathode caused by the recoil of ions emitted from a source existing between two fixed boundaries. The balance equation simply reduces to $J_i/J_e = \sqrt{m_e/m_i}$.

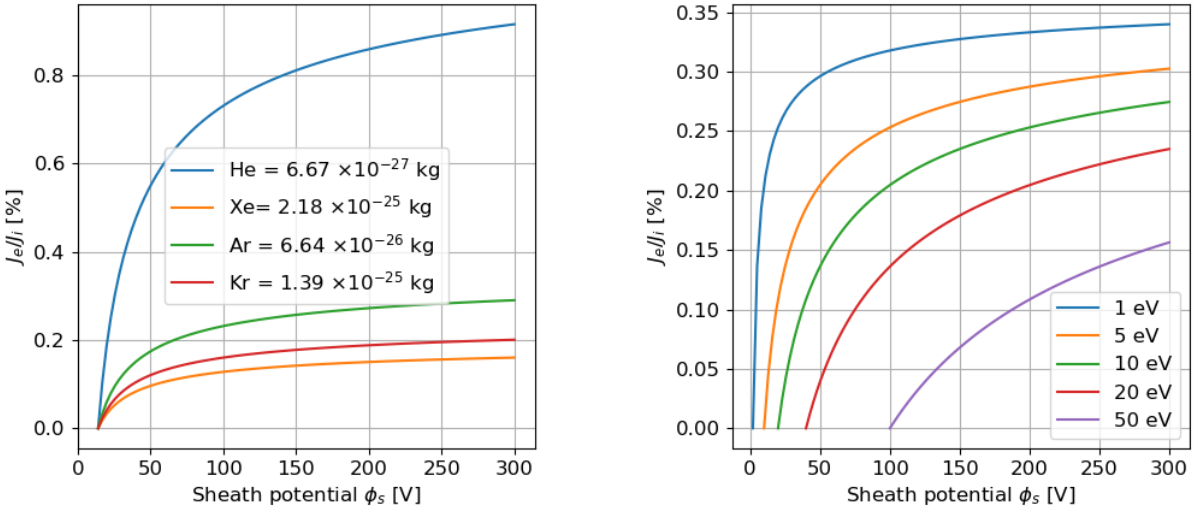

Figure 2.2: [Original] (Left) The ratio of election and ion current densities as a function of sheath potential are shown in a double layer for common plasma species ranging from heavy atoms (xenon) to lighter atoms (helium). (Right) The current density ratio is instead shown for increasing electron temperatures for an argon plasma.

For sheath potentials ranging from $\phi_{s,min}$ to 300 V, the current density ratio J_e/J_i varies substantially from lighter to heavier gases. Helium plasma, which is researched for use in nuclear fusion where D-T (deuterium-tritium) is a commonly used reaction, is approximately two orders of magnitude lighter than xenon. As a function of sheath potential, its fraction of electron current to ion current increases rapidly due to the smaller difference between the helium in electron to ion mobility. The opposite is true for a heavy gas such as xenon. In the accelerator regions of electric propulsion devices such as ion thrusters it is important to consider how the double sheath affects ion acceleration to the grid structures, and to choose the plasma species accordingly. The sheaths at thermionic cathode surfaces are typically large enough to form counter-streaming ion and electron currents and are treated as double layers. Equation 2.21 then becomes useful in calculating the maximum amount of current that can be extracted from the cathode. The maximum amount

of current density emitted from a thermionic cathode would increase the ionization efficiency and therefore the total efficiency of the electric propulsion device and is yet another example of how sheath physics can contribute to affecting the performance of a plasma device [54].

Figure 2.2 is also used to explore how the current density ratio of electrons to ions varies within a plasma of the same species for different electron temperatures. The sheath current density ratio as a function of sheath potential for argon is parametrically shown: for low electron temperatures ($\approx$1eV), a steep increase of ion current density fraction of the ion current occurs. This is a consequence of a larger contribution of the ion recoil onto the cathode surface compared to the electron pressure due to the Maxwellian distribution. For hot electrons up to 50 eV, the variation in ion to electron density ratio is reduced, again due to the relative contribution of mobile electrons compared to ions.

2.2 Volumetrically Complex Surfaces (VCMs)

2.2.1 Pores Per Inch

Volumetrically complex materials, for example reticulated foams, are often described by their geometric properties which include their average ligament diameters, d, their average pore diameters, D, their thickness, t and their aspect ratio:

$$A_R = D/d \tag{2.22}$$

and are shown in Figure 2.3 [55].

The metric for specifying the pore and ligament geometry of open-cell foams often specified by the manufacturer is Pores Per Inch (PPI). The PPI of a foam is defined as:

$$\text{PPI} = \frac{\Lambda}{D+d} \tag{2.23}$$

where Λ is a constant, defined here to be $\Lambda = 1$ inch. Thus, PPI is a linear measure of pore diameters in an inch and will be a geometric foam metric used in this work.

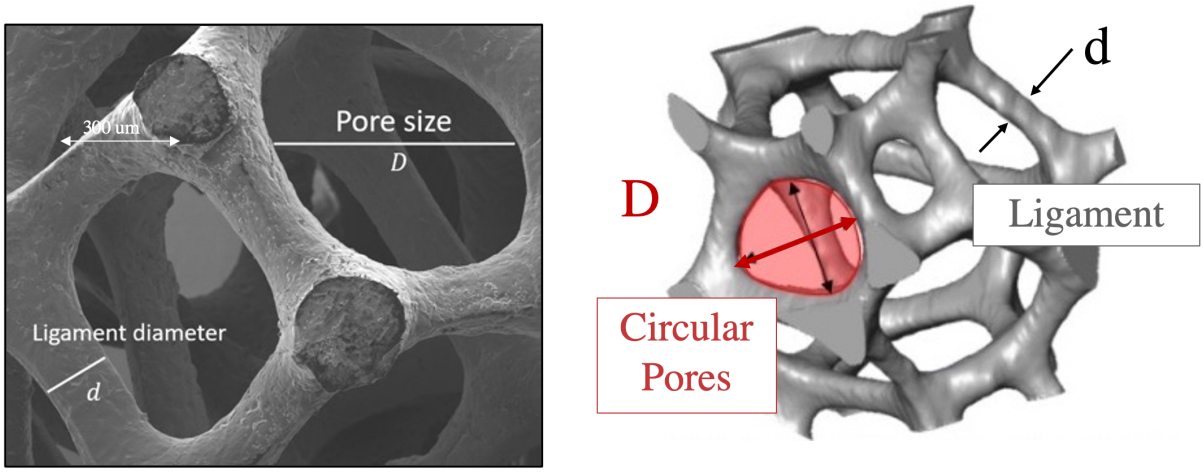

Figure 2.3: Scanning Electron Microscope image of an aluminum foam, indicating d the ligament diameter and D the pore diameter and a 3D rendering of a reticulated foam.

2.2.2 Plasma infusion

Recent studies [9, 38] have shown that there are two regimes of plasma-interactions unique to VCM materials which significantly affect the trajectory and yield of incident plasma electrons and emitted secondary electrons. (1) In the plasma-infused regime the plasma penetrates into the material structure, thus creating a thin sheath which conforms to ligaments below the material surface, and (2) the plasma-facing regime in which the plasma is entirely shielded by a thick sheath which is larger than the characteristic VCM pore or cavity length. In Figure 2.4 the sheath thickness L_s is shown in comparison with the pore size of a VCM D_p for the plasma-infused and plasma-facing cases.

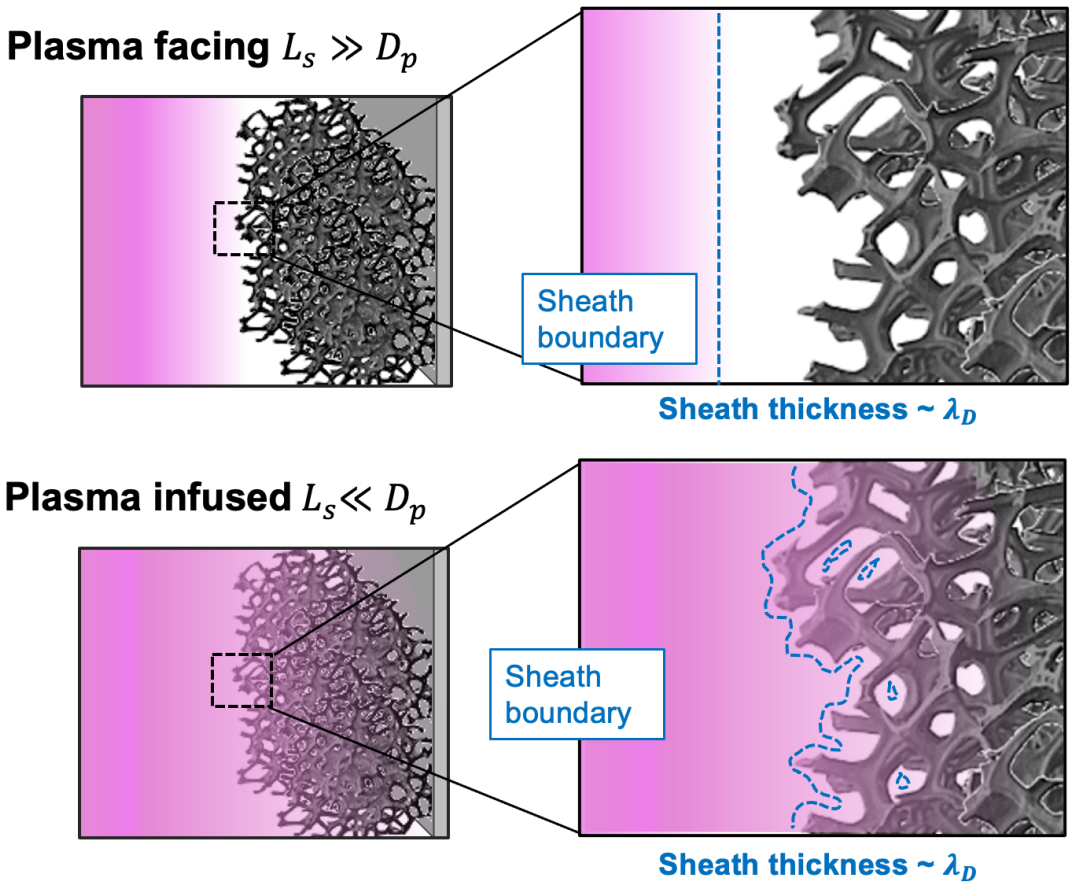

Figure 2.4: Plasma-facing (above) and plasma-infused (below) regimes respectively shown for the case of a sheath thickness, L_s larger than the VCM cavity length (or pore size) D_p and the sheath thickness smaller than the cavity length. These diagrams represent a floating wall sheath which is approximately proportional to the Debye length, λ_D.

2.3 Secondary Electron Emission

2.3.1 Semi-empirical theory and the Universal Curve

Secondary electron emission (SEE) is a phenomenon occurring when with sufficient kinetic energy charged particles are incident on a solid surface causing electrons to be expelled. The emission of secondary electrons from the same side as the incident primary electron side will be discussed.

Secondary electron emission yield depends on the work function of the material as well as properties such as target density and angle of primary electron incidence. Absorption of ions and atoms of electropositive metals on the surface increases the photo-electric and thermionic emission from metals. There isn't yet a single theory which incorporates all SEE phenomena however an elementary approach is that secondary electrons are liberated by the transfer of energy from the primary electrons to the lattice electrons. Primary energy depends on the energy loss by penetration depth, absorption and scattering. The secondary electrons are scattered and subsequently a fraction of these will be lost by absorption before making it out of the surface. The work function of the material has to be overcome therefore for the secondary electron emission to be possible [49, 56].

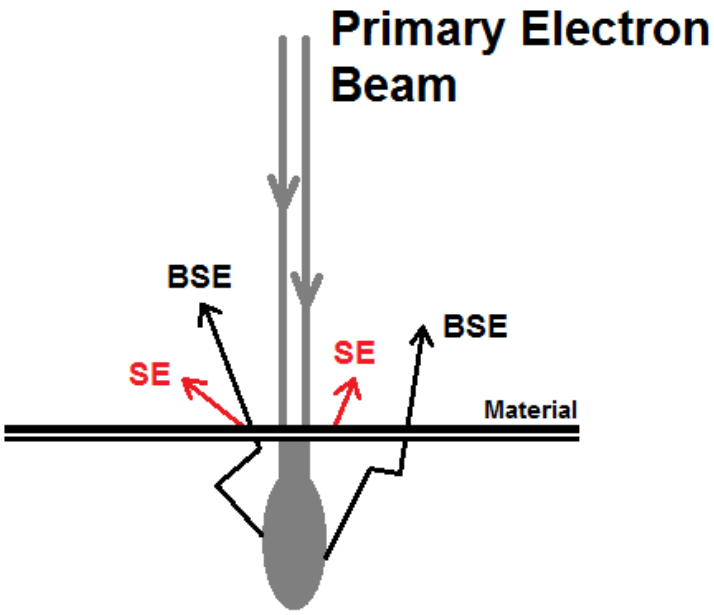

Figure 2.5: Primary electrons are incident on the surface and in turn induce different types of electrons: backscattered electrons (BSE) which originate from elastic and inelastic collisions and secondary electrons originating from BSE and primary electron interactions much closer to the surface of the sample.

A semi-empirical theory can be described in detail to understand the mechanics of secondary electron emission with the following assumptions:

- The amount of secondaries n_{SEE} produced along the path of the primary electron per unit

length is equal to the energy loss of the primary electron divided by the amount of energy (E_{SE}) to produce one secondary electron.

$$n_{SE} = \frac{-dE}{dx}\frac{1}{E_{SE}}$$

- The escape probability of one secondary electron from its generation depth to the surface of the material follows an exponential decay law where β is the decay rate which depends on density properties of the material and is given by

$$P_{escape} = e^{-\beta x}$$

where x is the position below the surface of secondary electron generation.

The primary electrons may or may not experience angular scattering and the rates of their power loss with material depth (dE/dx) are governed by two different expressions:

- For primary electrons which undergo angular scattering, a *constant loss* assumption is made which states that the average loss of energy of the primaries is not dependent on the depth x, and

$$dE/dx = -E_{PE}/R$$

where R is the penetration depth and E_{PE} is the primary electron energy. This accounts for the angular scattering of the primary electron.

- Primary electrons which do not undergo angular scattering have energy loss which is described by the power law

$$dE/dx = -A/E_{PE}^{n-1}$$

where experimentally it has been found that $n = 1.3 - 1.6$. [57]

Then the secondary electron yield as a function of the primary electron energy is [58, 57]

$$\gamma(E_{PE}) = P_{escape}\frac{E_{PE}}{E_{SE}}(1-e^{-\beta R})\frac{1}{\beta}. \tag{2.24}$$

It is therefore described as the product of probability of escape with the density of secondary electrons and an absorption term. Experimentation using Auger and XPS analysis has shown that there is a *universal* energy dependence which is described in the following equation:

$$\boxed{\gamma_s/\gamma_{s,max} = exp\Big\{-\frac{\left[\ln\left(\frac{E_{PE}}{E_{PE,max}}\right)\right]^2}{2\alpha^2}\Big\}} \tag{2.25}$$

This curve represents an empirical equation for the energy dependence of the yield found by fitting a Gaussian function of the logarithm $ln(E_{PE}/E_{PE,max})$ where $\alpha = 1.6$ is the variance to experimental data. $\delta_{s,max}$ and $E_{PE,max}$ are the peak secondary electron yield and where with what primary beam energy that peak occurs for a given material. [20]

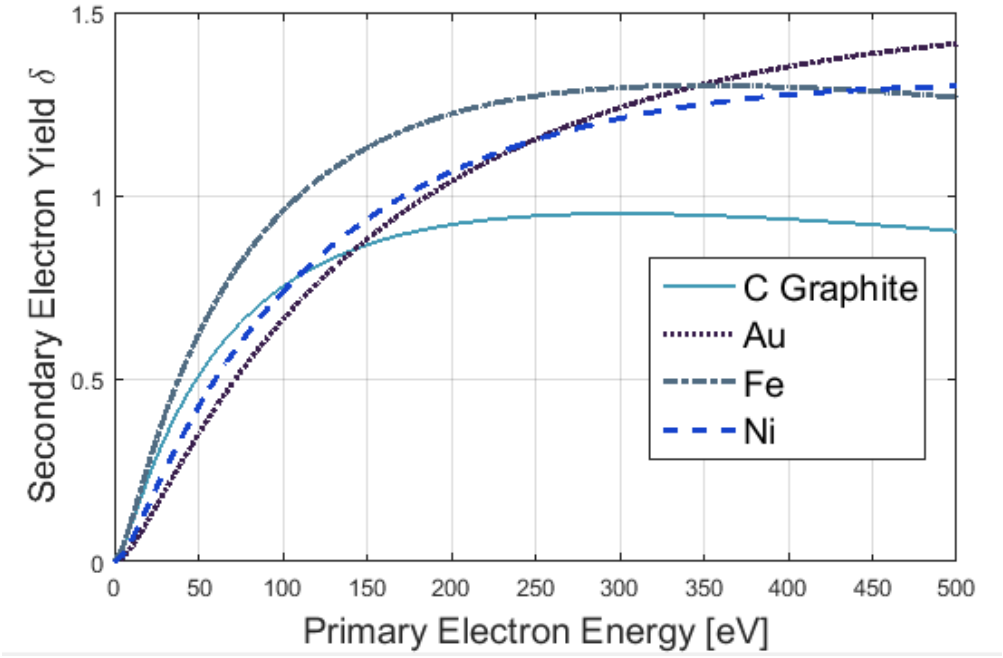

Figure 2.6: Universal Curve shown for different metals with incident primary electron beam ($\theta = 0^o$ to the normal) including carbon graphite.

2.3.2 Angular dependence of SEE

Another dependence which is important to consider in the study of secondary electron yield is the angle at which the primary electron beam is incident on the sample. It has been found experimentally [56, 58] that the angular distribution of secondary electrons has very low dependence on the incident beam angle. The angular distribution of secondary electrons is approximately a cosine distribution. Although the angles of the emitted secondaries follow the anisotropic nature of secondary electron generation and do not depend strongly on incident angle, many studies have been made on the secondary electron yield dependence of the primary electron beam angle. It is found than non perpendicular angles of incidence increase the secondary electron yield. If we let x_m be the generation depth which is the depth in the material at which the secondary electrons are generated, the when the primary electron beam falls normally to the materials. the secondary electrons will be x_m distance to travel before they can escape from the surface of the material. When the

primary beam is tiled at some angle θ however, then the distance is reduced by a $\cos\theta$ factor.

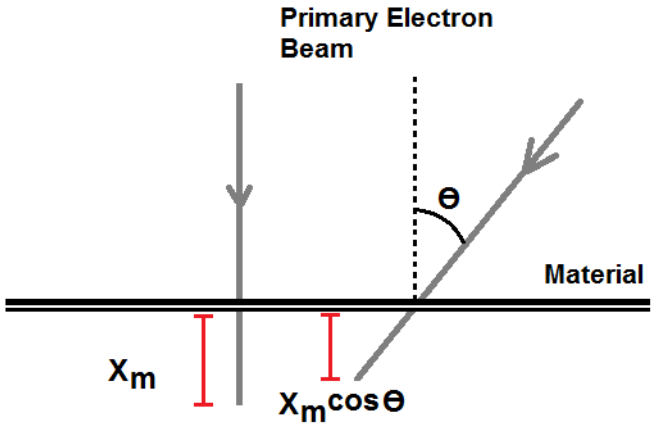

Figure 2.7: Increasing the angle of incidence θ (measured against the normal) will increase the secondary electron yield as the generation depth x_m of the material doesn't change.

To quantify by how much the tilt of the primary electron beam increases the secondary electron yield then the relation between the generation depth and the primary number of incident electrons is

$$\gamma_o = \gamma_{max} e^{-\alpha x_m}$$

where α is a constant proportional to the density of the target material. The secondary electron yield decays exponentially within the material; the dependence on θ is introduced in the exponential factor then

$$\gamma_\theta = \gamma_{max} e^{-\alpha x_m cos\theta} \tag{2.26}$$

This result is important because it shows that the minimum amount of secondary electron yield occurs when the primary electron beam is perpendicularly incident to the sample ($\theta = 0^0$) and is maximized when the beam or primary electron tends towards being parallel ($\theta = 90^0$) with the sample.

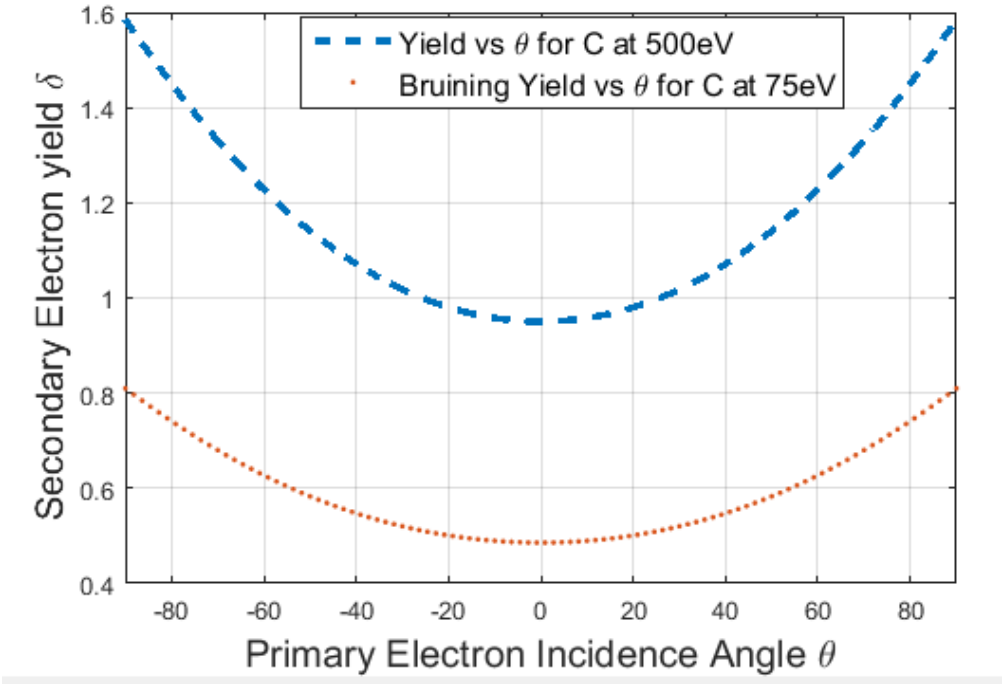

Figure 2.8: The variation of secondary electron yield γ with angle of primary electron beam with the normal to the surface is shown for carbon at two different primary electron energies: 500 eV and 75 eV.

2.3.3 Backscattered Secondary Electrons (BSEs)

Secondary electrons (SEs) are generally divided into 'true' SEs and backscattered electrons (BSEs). True or low energy SEs originate from within the target material and are emitted due to the interaction between an energetic primary electron and by overcoming the material work function. True SEs are generated between 1 – 50 nm below the surface [58] and are conventionally defined to have energies $<$ 50 eV. These low energy electrons may cause electron instabilities and cooling of plasma systems. BSEs are reflected primary electrons which are either inelastically scattered (iBSEs), thus losing some of their energy through the material surface during collisions with core electrons, or elastically backscattered (eBSEs) and which are reflected with the same energy as the incident electrons. Other inelastic scattering products include plasmons, phonons and polaron excitations. Auger electrons may also be emitted following energetic bombardment of a surface,

and the detection of these electrons forms the basis for Auger Electron Spectroscopy (AES). Auger electrons have energy proportional to the transition of an electron from an outer shell to a core hole caused by electron interaction with the surface and are atomic specific. The total SEE yield is defined as:

$$\gamma_{tot} = \gamma_{SE} + \gamma_{BSE} \tag{2.27}$$

where

$$\gamma_{BSE} = \gamma_{iBSE} + \gamma_{eBSE} \tag{2.28}$$

The secondary electron energy spectrum for a primary beam of 20 keV, typical of a Scanning Electron Microscope, is shown in 2.9 and was taken from Ref.[3]. The true low energy electron peak is < 50 eV and the elastic backscattered peak is at the primary energy of 20 keV. In between these two energies are inelastically backscattered electrons.

2.3.4 Secondary electron emission effect on the plasma sheath

As previously seen, the sheath potential at the plasma vessel wall (thruster channel) is modified in the presence of secondary electron emission. It has been found that in SPT plasma thrusters, where the channel is made of dielectric ceramics, there is lower electron temperature and longer acceleration regions than in TAL thrusters. The potential drop on the sheath and pre-sheath will cause an increased loss of electrons to the wall and these losses depend strongly on the yield of the SEE. Studies on the modification of electron temperature distribution have also been done where an increased value of the peak temperature T_e as well as kinetic effects of the back flow of electrons on the sheath [59, 60, 61]. To summarize the potential drop at the sheath by using ion and electron current balances, where A is the wall area, the ion current is:

$$I_i = \frac{1}{2} n_i e \sqrt{\frac{k_B T_e}{m_i}} A \tag{2.29}$$

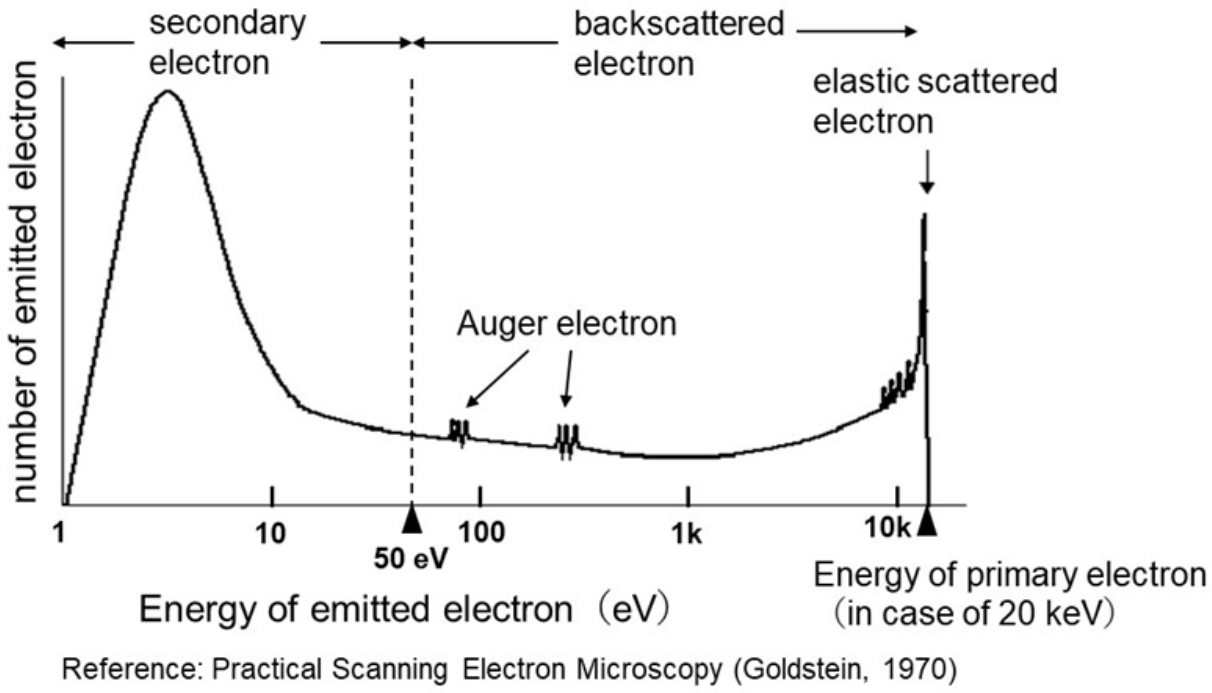

Figure 2.9: A semilog energy spectrum of secondary electrons includes a true secondary electron peak $<$ 50 eV and an elastic backscattered secondary electron peak at the primary electron energy [3].

$$I_e = \frac{1}{4}\sqrt{\frac{8k_BT_e}{\pi m_e}}n_e e A e^{-e\phi/k_BT_e} \tag{2.30}$$

Restating the electrostatic sheath solution that forms between a plasma and a wall to prevent a net flow of current in the absence of any SEE (Eq. 2.13):

$$\phi_w = -\frac{k_BT_e}{e}\ln\sqrt{\frac{m_i}{2\pi m_e}}.$$

When electrons are emitted from the wall however, then the electron current is modified to include the SEE yield factor γ. The ion current remains the same and electron current becomes

$$I_e - \gamma I_e = I_e(1-\gamma)$$

Replacing the derivation and 2.13 with modified electron current for SEE yield it is found that the floating sheath potential is reduced, and assuming the ion Bohm speeds at the sheath edge its new form is:

$$\phi_{SEE} = \frac{kT_e}{e} \ln \left[(1-\gamma) \sqrt{\frac{2m_i}{\pi m_e}} \right] \tag{2.31}$$

Increasing γ decreases the potential drop of the sheath, effectively reducing the overall sheath [31, 60, 49, 62, 63, 64]. A similar formulation can be found for including SEE yield in the electron sheath [49, 53].

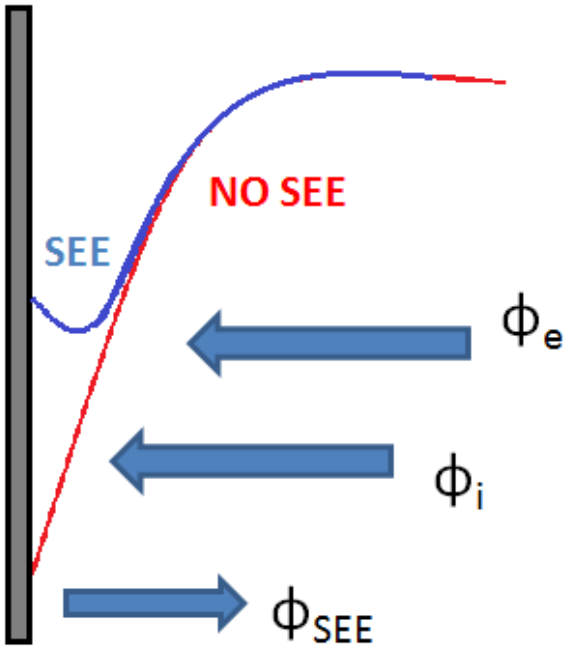

Figure 2.10: Potential drop at the wall is reduced in the presence of SEE.

CHAPTER 3

Research Approach Overview: Analytical, Computational, and Experimental Methods

3.1 Approach Overview

A comprehensive range of experimental and analytical modeling approaches were used to investigate the objective of this thesis. Experiments were conducted across three main laboratories: the Plasma, Energy and Space Propulsion Laboratory within the Mechanical and Aerospace Engineering department at UCLA, the LArge Plasma Device (LAPD) at the Basic Plasma Science Facility within UCLA Physics & Astronomy, and the Nano-synthesis and Surface Science and Technology laboratories at the Princeton Plasma Physics Laboratory. Not only were well-established and known facilities and models used to investigate the PMI and SEE of VCMs, but a dedicated experimental PMI diagnostic, a novel compact PMI device, and a custom SEE model were also developed in the scope of this thesis.

3.2 Experimental Overview

To examine SEE behavior of VCM from reticulated carbon foams, an indirect, a direct and spectroscopy methods were performed experimentally. In the indirect SEE measurement, a Scanning Electron Microscope [3] was used to simultaneously evaluate the SEE yield using a pixel intensity calibration technique described in [40] and the VCM geometry. Key trends and properties such as the VCM transparency to a backplate, τ, were defined and identified and were reported in [6].

A direct method using a sample-collector current measurement with an electron gun as described in [65] was used to evaluate similar foams for their SEE yield properties. To closely examine the energy distribution of emitted true and backscattered secondary electrons, spectroscopy using a Cylindrical Mirror Analyzer with an electron analyzer typically used for Auger spectroscopy was also used in the direct SEE measurement efforts at the Princeton Plasma Physics Laboratory. These methods and results are described in chapter 4.

The PMI experiments on layered Al, Cu and W foams were instead conducted on three devices at UCLA: two steady state hollow cathode generated plasma devices (respectively Pi and MOChA using Xe and Ar plasmas), and a 20 m pulsed linear plasma device producing He plasma with a gridded Mo anode in front of a LaB6 planar cathode. To better understand the erosion of VCMs, a novel diagnostic was developed and commissioned in the Pi facility using a Long Distance Microscope [1]. A smaller, compact MOChA PMI plasma device was commissioned as a part of this thesis with a full PMI and plasma diagnostic suite to perform rapid, iterative PMI experiments on biased and floatign VCMs. Results and experiments conducted on these devices are found in chapter 5.

3.3 Modeling Overview

To inform the experiments conducted on SEE from VCMs, a previously developed analytical model based on Monte-Carlo simulations was used to compare with data and trends [4]. A custom analytical model, AMPS-E was also developed [5] to more precisely analyze SEE and ion-induced SEE from reticulated carbon foams, and to optimize foam geometries and structures for reduced SEE yield configurations.

3.4 AMPS-E Overview

Following is a brief overview of an analytical model developed for calculating electron and ion-induced SEE from an open-cell, reticulated VCM, or foam, and is an adaptation of the work and paper presented in [5].

The Analytical Model for Particle Sputtering (AMPS) is an analytical model developed by Li and Wirz [9] for modeling the ion sputter yield from a reticulated VCM, or foam, with a layer-specific treatment of the foam. The model is described and derived in detail in Chapter 7 of [9] and is based on a cage geometry approximation of a foam structure. Each layer and sub-layer contributes individually to the effective sputter yield and includes properties such as material opacity, effective sputter area and ballistic particle deposition and ligament intersection. AMPS uses the physics of sputtering in its analytical formulation which includes empirical expressions for describing the angular distribution of emitted sputterants, and the angular dependence of sputter yield on primary angle of incidence. This model was modified to be able to treat electron-induced SEE and and ion-induced electron emission (IIEE) by using a cosine angular distribution of emitted electrons and the secant angular dependence on primary incident electron and ion. The electron emission version of the model is referred to as AMPS-E, and also includes energy dependence using the Universal Curve for SEE and energy-fit equations for IIEE.

AMPS-E is written in MATLAB, and has an inputs the foam geometry which includes ligament and pore diameters, respectively d and D, as well as the foam aspect ratio $A_R = D/d$, the number of layers or equivalently the foam thickness, and the primary ion or electron incident energy. The model only considers normally incident electrons. For reticulated foams, the Pores Per Inch linear metric is commonly used to describe the linear pore density of the material. The PPI of a foam is defined as:

$$PPI = \frac{\Lambda}{D+d} \tag{3.1}$$

where Λ is a constant, defined to be 1 inch here.

An important modification to AMPS which is included in AMPS-E is the contribution to SEE yield of the flat backplate. Fig. 3.1 shows the different configurations of a foam with and without a backplate. The output of AMPS-E is therefore:

$$\gamma_{tot} = \gamma_{foam} + \gamma_{backplate}. \tag{3.2}$$

To find the backplate electron yield contribution it is necessary to define the transparency of a foam, τ. This is defined in the plane parallel to an incident particle beam as the ratio of exposed backplate area to the total projected surface area of the foam [6]:

$$\tau = \frac{A_{\text{backplate}}}{A_{\text{total}}}. \tag{3.3}$$

$$\gamma_{backplate} = \tau^2 \cdot \gamma_{flat}. \tag{3.4}$$

A detailed analysis of foam transparency derivation and measurements can be found in 4. It was found by comparing experimental data of backplate SEE yield to transparency measurements that the SEE yield exiting the backplate through the foam is proportional to the square of the transparency. Thus, in AMPS-E:

$$\gamma_{tot} = \gamma_{foam} + \tau^2 \cdot \gamma_{flat}. \tag{3.5}$$

The results derived from this model and a comparison to experimental measurements are described and discussed in chapter 4.

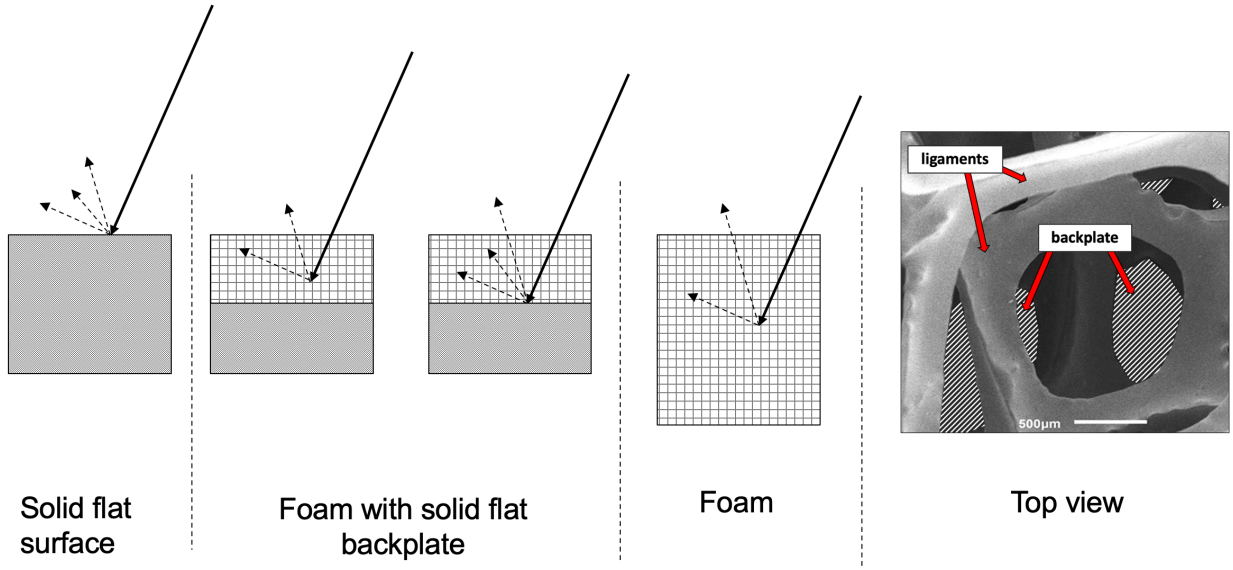

Figure 3.1: Electron emission from a flat surface experiences no geometric trapping, while electron emission from a foam surface typically is reduced due to ligament capture. In many realistic setups and material applications however, a combination a solid backplate and foam results in SEE yield which is between foam and flat plate yields. On the right, an SEM micrograph is shown with a top view shaded backplate area.

CHAPTER 4

Secondary Electron Emission of VCMs

The following chapter describes the research conducted on evaluating SEE from carbon foams using Scanning Electron Microscopy (SEM). This analysis is relevant to electrons incident on a carbon foam surface in the plasma-facing regime.

4.1 SEM experiments and geometric evaluation

4.1.1 Carbon Foam Samples and SEE Evaluation

In recent studies, complex materials with surface featuring such as pillars, fibers, fuzzes, and nanotendril bundles [66, 67] have been shown to reduce emitted particles such as secondary electrons and in some cases, surface sputterants, by trapping them with their features. Such materials have exhibited an overall reduction in SEE when compared with a flat surface. Volumetrically complex materials (VCMs) are open-celled, reticulated porous materials which retain complexity their structure, and are often referred to as foams. It has recently been demonstrated that VCMs have a sustained reduced sputter yield of up to 60% [9] in contrast with materials where surface features are sputtered away during plasma exposure, resulting in a flat surface. With conventional complex surfaces such as fuzzes, the reduced sputter yield tends to that of a flat value with increasing ion fluence. VCMs and foams have also been theorized to reduce SEE, and recent experiments have shown a reduction of yield from copper foams of $\approx$20% [68] compared with a flat surface.

Secondary electrons are divided in two categories: backscattered electrons, and true electrons. Backscattered electrons are generally produced via elastic and inelastic scattering between an en-

ergetic primary electron and the material surface, while true secondary electrons instead are generated via energetic primary particle interaction with a target material atom a few nm's below the surface and have energies <50 eV. True secondary electrons are of particular interest for this work as they are generally responsible for bulk plasma cooling. SEE yield is defined as the ratio between number outgoing (secondary) electrons and incoming (primary) electrons at a material surface.

Related previous work [40] has used a rapid technique to evaluate SEE yield from a complex surface while also measuring geometric properties by using a Scanning Electron Microscope (SEM). Such measurements were performed on a carbon velvet surface and revealed that the surface density of the velvet fibers is a useful measure for predicting SEE yield. This is caused by the non-uniform arrangement of the fibers. A closer manufacturing spacing between fibers will cause the fibers to support each other and effectively trap electrons in the inter-fiber spacing, whereas sparse fibers will tend to bend and add side surface area of the fibers to the total SEE yield. Overall, carbon fibers reduced SEE yield by up to 65%, and an optimized surface fiber density, and as well as angular trends were observed. In this work, we propose the same technique instead on carbon VCMs, or carbon foam surfaces, and compare results with theoretical models. The goal is to characterize SEE yield as a function of surface geometries of the foam such pore and ligament dimensions, ligament orientations. In addition, a new metric for evaluating foams is defined and demonstrated as contributing to SEE yield trends: foam transparency. Unlike materials which are always composed of a solid substrate with features grown or attached to the surface, a foam surface may be partially transparent to a primary electron beam if there is no substrate behind it. Thus, the transparency is defined as the two-dimensional ratio of exposed substrate to the total sample surface area.

The carbon foam, or reticulated vitreous carbon (RVC) samples analyzed were manufactured by ERG Aerospace and are Duocel ® foams. Duocel foams are manufactured using a reticulation process and have a porous, open-celled structure which consists of a network of solid ligaments ([69]). These foams are geometrically self-similar, as is apparent in Fig. 4.1. Each cell is made of structural ligaments and 14 spherical pores which have average diameters respectively d and D, as

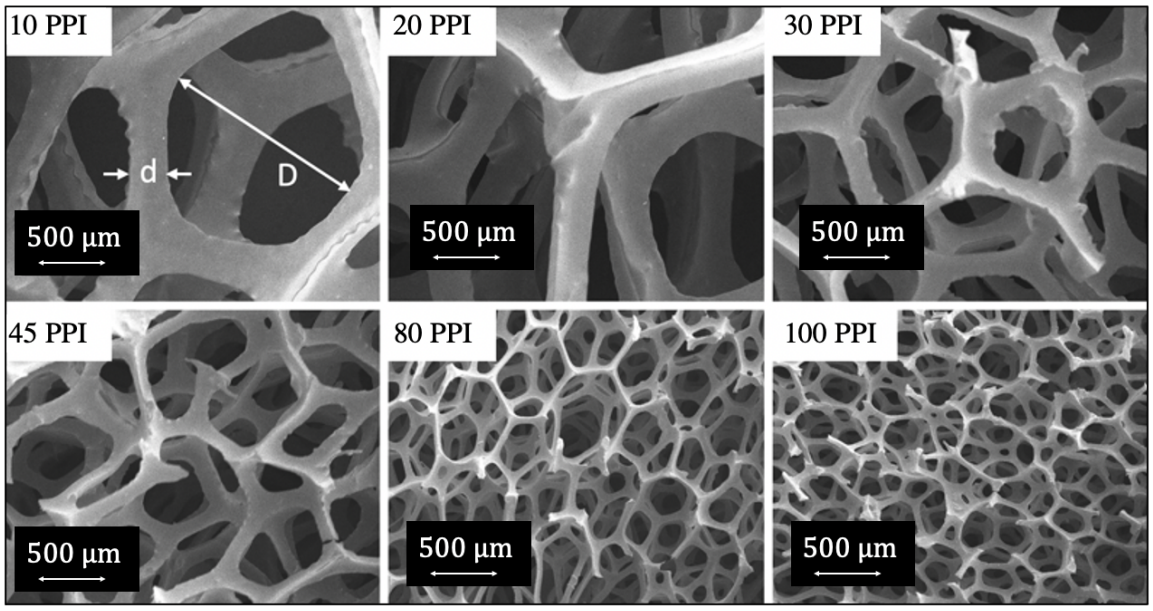

Figure 4.1: SEM images of each PPI foam. The images were acquired with a primary electron energy of 500 eV and have a fixed magnification with a scale size shown in the top left image. The ligament diameter, d and the pore diameter, D are also indicated using 10 PPI foam as an example. Each sample is 6 mm thick (this is the depth in the plane perpendicular to the SEM electron beam).

shown in Fig. 4.1.

The metric for specifying the pore and ligament geometry of open-cell foams specified by the manufacturer is Pores Per Inch (PPI). To reiterate from 2, the PPI of a foam is defined as:

$$\text{PPI} = \frac{\Lambda}{D+d}$$

where Λ is a constant, defined here to be $\Lambda = 1$ inch. Thus, PPI is a linear measure of pore diameters in an inch and will be a geometric foam metric used in this work. The carbon foams analyzed for their SEE properties have PPIs of 10, 20, 30, 45, 80 and 100. These are converted to pores per mm per pore in Table I.

Fig. 4.1 show one SEM image of each PPI foam analyzed in this work. These images are acquired using a low primary electron energy of 500 eV because they are a part of sets of multiple images used for evaluating SEE yield. Another metric for specifying foams is the aspect ratio of

PPI	Pores per mm
10	2.54
20	1.27
30	0.85
45	0.56
80	0.32
100	0.25

Table 4.1: PPI in pores per mm.

pore diameter (D) to ligament diameter (d), D/d. This ratio is roughly fixed at $D/d \approx 5$ for all the PPI foams being analyzed (see Fig. 2).

In addition, each of the six PPI foams has a volume fill density of 3%, a thickness of 6 mm and have a rectangular surface of 3 $\times$ 2 cm. The thickness of the foams was indicated by the manufacturers and carefully measured with calipers before SEE measurements were taken. Table 4.2 shows the average dimensions of the carbon foams for each PPI. D and d were found by measuring up to 10 ligaments and pores for 5 images of each PPI foam. Fig. 4.2 is a graphic representation of the average dimensions of ligament versus pore diameters compared with a best fit line with a slope of 5. The average spread in the dimensions of these foam structural elements is of up to 21%, which can likely be attributed to the manufacturing process. While the parent cells are designed to be uniform, the resulting pores and ligaments may deform during the reticulation process while the foam material solidifies ([70, 71]).

It is important to note that due to the large depth of field of an SEM and the fixed thickness of each foam, images of foam samples with large pore sizes (10 – 80 PPI) also include the flat backplate that the foams are placed onto. This characteristic is described as the *transparency* of the foam, which will be defined in a later section in relation to its contribution to the total SEE yield. The material used as the flat surface base beneath the foams is a 3 mm thick slab of highly oriented pyrolytic graphite (HOPG).

Table 4.2: Pore and ligament dimensions of carbon foams.

Pores Per Inch [PPI]	D [μm]	Std Dev [μm]	d [μm]	Std Dev [μm]	D/d	Std Dev
10	1885	453	351	27	5.42	1.53
20	1471	219	297	38	5.00	0.82
30	723	284	130	18	4.64	2.01
45	447	171	88	18	4.36	2.46
80	282	52	56	6.7	5.92	1.33
100	202	50	41	5.7	4.70	1.18

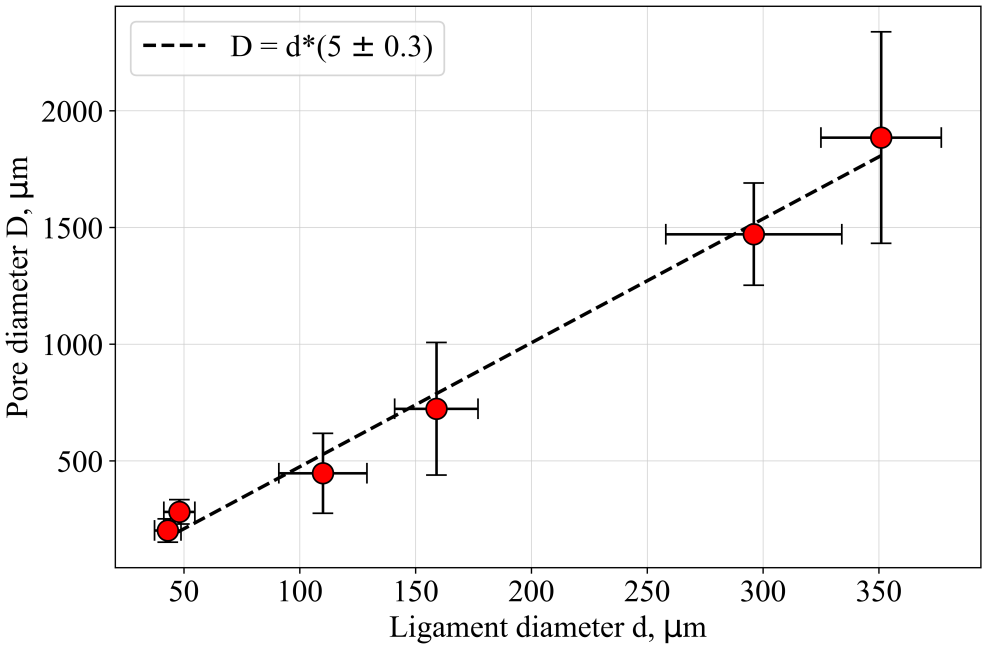

Figure 4.2: Ligament vs pore diameter for each PPI carbon foam. The pore diameters are approximately 5 times larger than the ligament dimensions, with an uncertainty of 6%.

4.2 SEE Determination

The SEM used for imaging and characterizing the SEE of carbon foams was a JEOL JSM-6010. The resolution of the JEOL SEM is $\approx$ 15 nm at 1 kV acceleration voltage, and an Everhart-Thornley type detector collects low-energy secondary electrons. All six PPI carbon foam samples were placed on a flat and smooth HOPG slab and introduced into the SEM chamber simultaneously. To ensure electrical contact between the two, carbon tape was used to bind the edges of the foam and graphite. A second flat HOPG slab with the same thickness as the carbon foams and a rectangular area of 1 $\times$ 3 cm was mounted onto the same stage for SEE calibration. Each of the carbon foams and the calibration graphite were placed adjacent to one another, and their top surfaces were all 6 mm above the stage plane. This was done to ensure that the same working distance could be used for the SEM electron gun and optics. During SEM imaging, the magnification and electron beam spot size were kept fixed, and the digital brightness and contrasts were also maintained fixed such that the entire dynamic range of the image pixel intensity histogram was included.

Each of the foam samples were imaged several times at adjacent locations on each of their surfaces by manually moving the sample stage in the chamber for primary beam energies between 500 eV and 1000 eV. These electron energies are relevant to applications where SEE yield is important to device performance, such as in Hall-effect thrusters ([15]), fusion divertors and limiters ([72]), and RF devices. Lower primary energies than 500 eV are not permitting in the SEM, but it is expected that the reported SEE yield trends with foam geometry will scale linearly for energies down to $\approx$ 150 eV ([73, 74, 75, 76]).

In addition, the 45 PPI and 100 PPI carbon foam samples were tilted using the tilt feature of the SEM stage to examine the angular dependence of SEE yield. Corresponding calibration graphite images were also acquired for each primary electron energy and foam tilt condition.

The SEM foam images were converted to SEE yield values by averaging the SEM-generated foam image grey-scale pixel intensities and then calibrating them with the known SEE yield of the

flat graphite found in previous experiments ([65, 77]). The value for SEE yield of flat graphite used in this work is γ_{flat} = 0.84 for a normal electron beam at 500 eV. The detailed technique for qualitatively determining SEE yield by using SEM imaging is described in Ref. [40].

4.2.1 SEE yield from carbon foams

The total SEE yield was calculated for energies varying from 500 eV to 1000 eV in steps of 100 eV for a 45 PPI carbon foam and a 100 PPI carbon foam. The SEE yields were compared both to theoretical values found by empirical theory ([58]) and to recent experiments conducted on smooth graphite using a direct sample-current method ([65]). The goal of these measurements is to quantify the average reduction in total SEE yield between a flat graphite surface and the carbon foams samples. The average SSE yield of a 45 PPI and 100 PPI foam reduced by 34.7$\pm$8% and 32.5$\pm$3% respectively, as compared to a flat graphite surface. The reduction in yield found for these carbon samples is larger than previously reported values measured from copper foams with 4.6% volume fill density at 100 PPI ([68]). This could be because of the higher volume fill density compared with the carbon foam samples which are 3% dense, or because of the difference in thicknesses between carbon and foam samples. The Cu samples in Ref. [68] have a thickness of $\approx$ 1 mm, compared with the 6 mm carbon foams reported here. Thus, it is possible that the Cu foams had less of a geometric trapping effect on the secondary electrons emitted from the sample holder below the foam. High aspect ratio carbon velvet surfaces (Refs. [40, 65, 78]) with 1.5 mm fiber lengths and packing densities of 4% have lower SEE yield than the studied foams as they can reduce SEE yield by up to 65%. However, foam materials may present other benefits such as sustained reduced sputter yield, stiffness, and applicability to liquid flow concepts.

4.2.2 Effect of PPI on SEE yield

The effect of PPI on SEE yield for each carbon foam sample was investigated with a primary electron beam energy of 500 eV. While the overall reduction of SEE yield between a foam material and

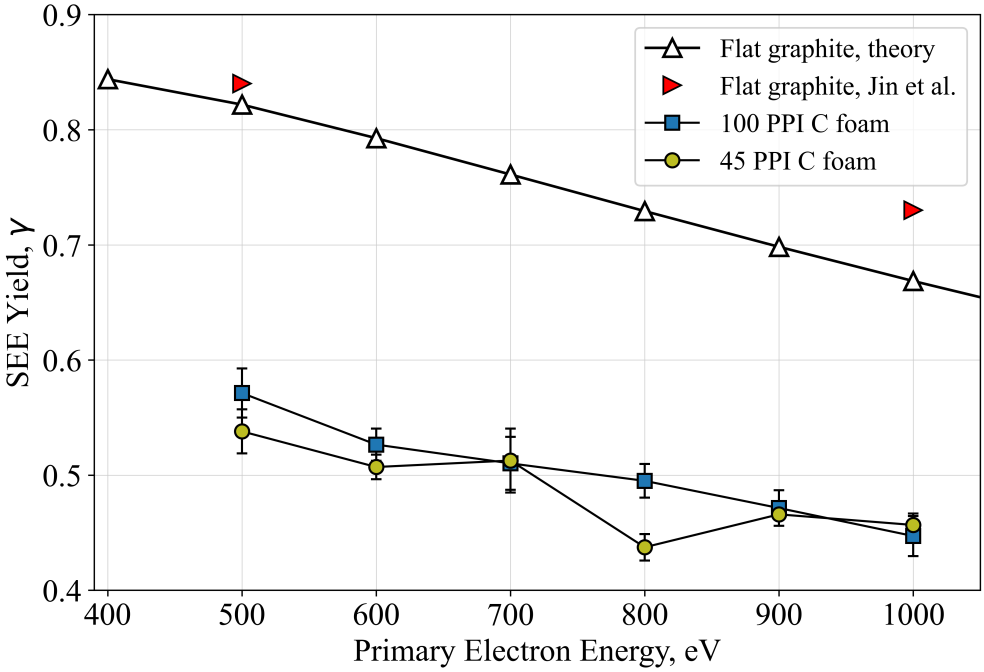

Figure 4.3: Theoretical SEE yield of flat graphite derived from empirical theory (white, triangular markers) and experimental SEE yield values of flat graphite (red triangular markers) are compared with two carbon foam samples as a function of primary electron beam energy. The reduction in SEE yield between flat graphite and carbon foam is 33.6%.

a flat surface has been quantified and reported, the effect of changes in geometry within foams has only been investigated computationally and with analytical theory. These results can be extended to primary electron energies between 150 eV and 1000 eV, where the Universal Energy Curve ([58]) has been measured for similar graphite surfaces ([79, 65]). The reduction of yield with foam geometric variation. should remain the same in this energy range. Each of the six carbon foam samples with varying PPI were imaged 10-15 times at adjacent areas by manually adjusting the SEM stage in the x-y plane, normal to the electron beam. The results are compared with analytical theory developed in 2017 by Swanson and Kaganovich in Ref. [4]. The analytical model developed by Swanson and Kaganovich approximates a foam or fuzz surface as a solid surface with one layer of isotropically aligned fibers placed above. This fiber-approximation foam model is an extension of a previously published model for describing uniformly aligned fiber surfaces, and does not account for tertiary electron interaction. The parameter which was found to characterize SEE yield from a foam is $u = A_{R1}V/2$, where A_{R1} is the aspect ratio $A_{R1} = h/r$, V is the volume fill density, h is the fiber layer height, and r is the radius of the fiber. The h and r parameters are respectively equivalent to the foam thickness and the ligament radius. To apply the Swanson and Kaganovich fiber-approximation foam model to the Duocel foams studied in this paper, a modification to the top layer SEE yield term is made. The Swanson and Kaganovich model is the sum of three SEE yield expressions which describe SEE yield from the top of the fiber layer (γ_{top}), the side surfaces of the fibers (γ_{sides}), and the bottom surface (γ_{bottom}), and each expression considers SEE generation and geometric trapping.

$$\gamma_{\text{total}} = \gamma_{\text{top}} + \gamma_{\text{bottom}} + \gamma_{\text{sides}}. \tag{4.1}$$

In the case of the top surface expression, only SEE generation is considered because this layer does not experience geometric trapping. A modification was made to the Swanson and Kaganovich model to better describe foam top layer SEE yield. For isotropically aligned fibers, it is sufficient to know the packing density (or volume fill density, V) of the fibers to calculate SEE yield from the top layer. For Duocel foams, a modified expression was used which describes the approximate

top surface area of a foam. The original top yield for the fiber foam approximation expression is:

$$\gamma_{\text{top}} = V\gamma, \tag{4.2}$$

where γ is the SEE yield from a flat carbon surface at normal incidence. The modified term for the reticulated open-cell foams analyzed herein is:

$$\gamma\prime_{top} = \frac{(D+d)^2 - \frac{\pi D^2}{4}}{(D+d)^2}\gamma = 1 - \frac{\pi}{4\left(\frac{d}{D}+1\right)^2}\gamma. \tag{4.3}$$

$(D+d)$ is the length across one pore and half a ligament on each side, and $(D+d)^2$ is the total area containing one pore and one surrounding ligament, assuming a circular pore. Equation 4.3 is the ligament area compared to the area of a total pore-ligament unit. The expression for $\gamma\prime_{top}$ is also shown with the ligament to pore diameter ratio term made explicit. For foams with a fixed value of d/D, $\gamma\prime_{top}$ is constant. For these calculations, the actual measurements of d and D were used rather than the approximate fixed ratio of $d/D = 1/5$ so that uncertainty propagation of foam geometries could be evaluated.

The results of the SEM measurements for SEE yield of varying PPI foams, in comparison with modified analytical fiber-approximation foam model from Swanson and Kaganovich is shown in Fig. 5. The flat value of SEE yield is γ_{flat} = 0.84 at 500 eV primary electron energy [65]. The percentage difference between the SEM curve and the modified Swanson and Kaganovich model varies between $\approx$ 50% for low PPI to $<$10% for 80-100 PPI foams. This indicates that at low PPI, a fiber-approximation of foams may not be suitable to predict SEE yield from SEM. In addition, the field of view of an SEM is limited to a few square mm. For the SEM used in these experiments, the maximum field of view for the lowest magnification setting is an area of 4 mm $\times$ 4 mm, which is dimensionally comparable to pore dimensions in the 10 and 20 PPI cases. Thus, 10-15 adjacent images may not be sufficient to comprehensively survey SEE yield from such large pore foams. This is also shown by the large error bars at 10 PPI. It was also noticed in SEM images that for

the physical carbon foams, ligaments can be quite brittle, and the top few layers may break from handling. This would effectively reduce the SEM SEE yield measurements as the non-suppressed top layer contribution (Equation 4.3) would be less than the theoretical value. The trends of SEE yield with PPI for both the SEM and the modified Swanson and Kaganovich model are similar in that they are decreasing with increasing PPI. The lowest SEE yield, in both cases, is found for 100 PPI foams. This result suggests that thinner ligaments and larger pore density is more effective at generating fewer secondary electrons while trapping more secondary electrons. However, the result is not straightforward and further investigation is recommended to assess SEE yield from foams of different geometries. It is apparent from SEM images (Fig. 2) that higher PPI foams have less visible substrate graphite layer, and carbon velvet studies have shown that the flat bottom base layer can have a significant contribution to total SEE yield ([40]). Thus, a further characterization of the geometries of carbon foams was conducted and is described in the following section.

4.2.3 Foam transparency and effect on SEE yield

An important geometric feature of the foams investigated in this work is the presence of a backplate. In realistic material applications, a foam may be mounted onto a substrate or electron-bombarded component. The contribution of a backplate on SEE yield is included in the analytic model developed by Swanson and Kaganovich, well as in previous Monte Carlo simulations developed by Huerta et al. ([29]). We define the foam transparency, τ, in the plane parallel to the primary electron beam and perpendicular to the foam surface. It is the ratio of exposed backplate area ($A_{\text{backplate}}$) to the total projected surface area (A_{total}):

$$\tau = \frac{A_{\text{backplate}}}{A_{\text{total}}} \tag{4.4}$$

100% transparency therefore describes a bare backplate, and 0% transparency describes a foam through which normally incident primary electrons intersect only foam ligaments. Fig. 6 is an SEM image of a 10 PPI foam where the smooth carbon backplate is visible behind the foam. The foam

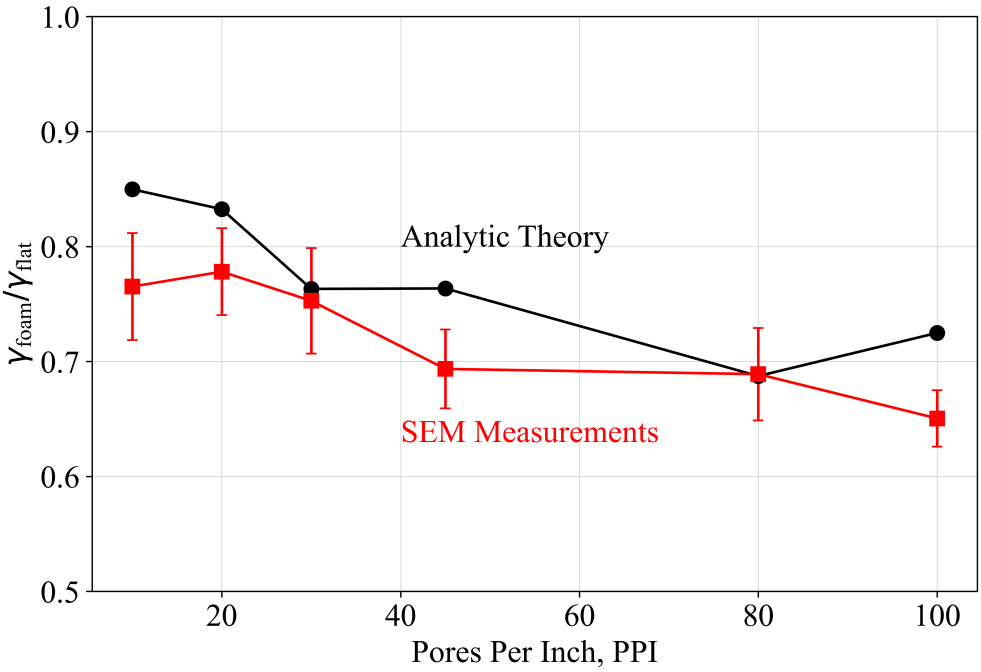

Figure 4.4: SEM derived measurements of SEE yield with varying PPI for Duocel carbon foams are compared with a modified fiber-approximation foam model derived by Swanson and Kaganovich ([4]). The SEM measurement reduction of SEE yield compared to the smooth graphite surface varies from 22.2% to 35.0%. The Low PPI foams show large error bars because in this regime, the SEM field of view is comparable to the dimension of pores. The primary electron beam energy is 500 eV where $\gamma_{flat} = 0.84$.

transparency to a backplate is dependent on the total foam thickness and on the PPI.

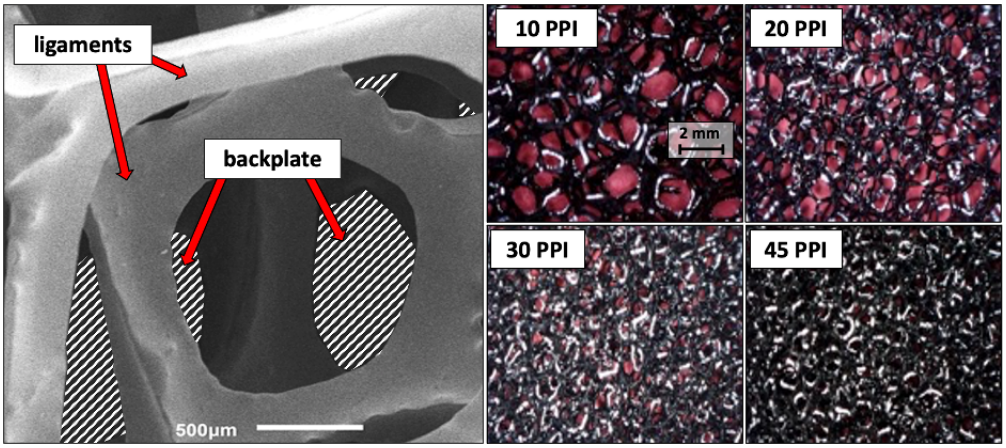

Figure 4.5: (left) An SEM image of a 10 PPI foam with 35% transparency. The transparency is calculated by taking the ratio of backplate area to the total area in the SEM field of view. (right) Optical images of 10, 20, 30 and 45 PPI placed over a bright colored surface. The colored area beneath the foam was used as a threshold in post-processing for removing backplate area and calculating foam transparency.

The foam transparency for each foam was measured using a combination of SEM image analysis and optical imaging, and a simple geometric expression was developed for comparing measurements.

4.2.3.1 Transparency determination using optical imaging

The first method for determining transparency was by using reflection optical microscopy and color-thresholding the background of carbon foam images. 10, 20, 30 and 45 PPI foams were imaged with a microscope with a brightly colored paper substrate placed beneath the foams. Fig. 6 (right) shows examples of optical images used for color-thresholding the backplate. The colored background was thresholded out to determine the percentage of ligament to total carbon foam image area. 10 images of each foam between 10 and 45 PPI were used to find an average transparency and related uncertainty. In the case of 80 and 100 PPI foams, the colored background was not visible through the carbon ligaments due to the microscope resolution. The average transparency of these higher PPI foams is later interpolated from 10 – 45 PPI foam data.

4.2.3.2 Transparency determination using SEM imaging

A major advantage of using SEM for SEE yield measurements is the simultaneous insight on the sample geometry provided by the images. A second method using SEM imaging was developed for determining foam transparency using image thresholding. Close inspection of the pixel intensity distribution histogram from SEM foam images reveals that there exists a Gaussian-like curve at the lower end of the intensity scale. A Gaussian intensity distribution is expected for a bare, smooth plate. Therefore, it can be inferred that the Gaussian-like curve is a combination of the backplate intensities and the foam ligament intensities. Lower PPI foams have a better-defined Gaussian-like backplate intensity distribution, while high PPI foams show only a narrow slice of the Gaussian, and 100 PPI foams barely show any trace of the backplate Gaussian-like distribution. Fig. 7 shows examples of the histograms of pixel intensity distributions for 10, 20, 30 and 80 PPI foams with a Gaussian distribution fit to the first peak on the lower end of the intensities. The intensity of the backplate in grey-scale was chosen to be one standard deviation above the peak of the Gaussian fit. The backplate intensity was used as the threshold for calculating transparency. In terms of image processing, the transparency is the ratio of numbers of pixels below the threshold to the total number of pixels.

The optical and SEM imaging methods were then compared to establish average transparencies for each PPI foam. The expression for describing transparency of a foam should roughly follow an exponential decay proportional to the foam thickness t:

$$\tau = A_0 \exp(-bt) \tag{4.5}$$

with initial area A_0 and decay constant b which will be described using foam geometric parameters pore diameter D and ligament diameter d. The foam aspect ratio A_R, PPI, A_0 and b are defined as follows:

$$A_R^{-1} \equiv \frac{d}{D} \tag{4.6}$$

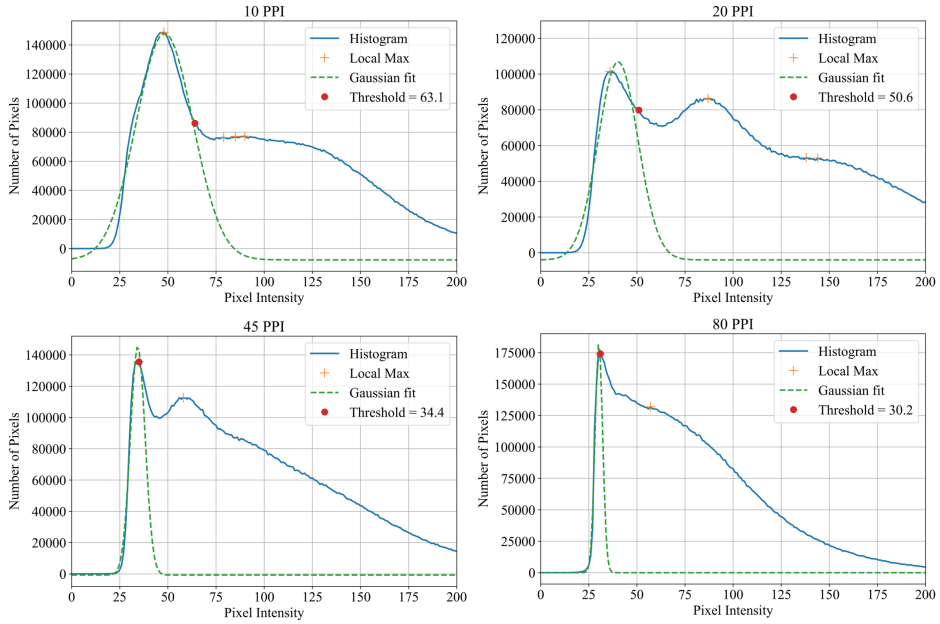

Figure 4.6: Pixel intensity histograms from SEM images of 10, 20, 45 and 80 PPI foams with a Gaussian fit at the first peak in the distribution. The first peak is expected to correspond to the flat backplate pixel intensity Gaussian distribution, and as PPI increases the peak becomes more narrow and less distinct from the foam ligament intensity pixels. The Gaussian fit peak was used for thresholding SEM images and determining transparencies.

$$\text{PPI} = \frac{25400}{D+d} \tag{4.7}$$

$$A_0 = \frac{\pi\left(\frac{D}{2}\right)^2}{(D+d)^2} = \frac{\pi}{4(A_R^{-1}+1)^2} \tag{4.8}$$

$$b = \frac{A_R^{-1}\,\text{PPI}}{24500} = \frac{A_R^{-1}}{D+d} \tag{4.9}$$

where d, D, t are in microns, and the initial coefficient A_0 is the transparent open area of a single layer with one circular pore and ligament unit. Fig. 8 shows the averaged foam transparencies with the exponential decay fit as well as transparency curves for smaller and larger thicknesses than the measured samples respectively of 3 mm and 10 mm. The transparency of a foam to a backplate is a metric for evaluating SEE yield which incorporates the thickness of the sample and the PPI of the foam into a single parameter. It has been shown by optical and SEM imaging validation that Equation 4.9 is a simple expression which can determine the transparency of a foam for given pore and ligament diameters, and foam thickness.

4.2.3.3 Foam transparency and SEE yield

The average foam transparency was compared to SEE yield in Fig. 9, showing a variation in SEE yield of under 20% for the samples tested. Between 15% and 30% transparency, the SEE yield increases by only $\approx 5\%$. This result is helpful to inform the design of foam surfaces mounted onto backplates when there is high transparency. This could be the case for low PPI foam designs or in devices where a confining wall thickness is limited. A thin foam can still suppress SEE yield sufficiently even with a $\approx 30\%$ backplate material transparency.

Establishing a method to determine sample transparency using only SEM images is also used to separate the foam ligament and backplate SEE yield contributions. This can simply be done in the same post-image processing step as when thresholding SEM images as described in Section

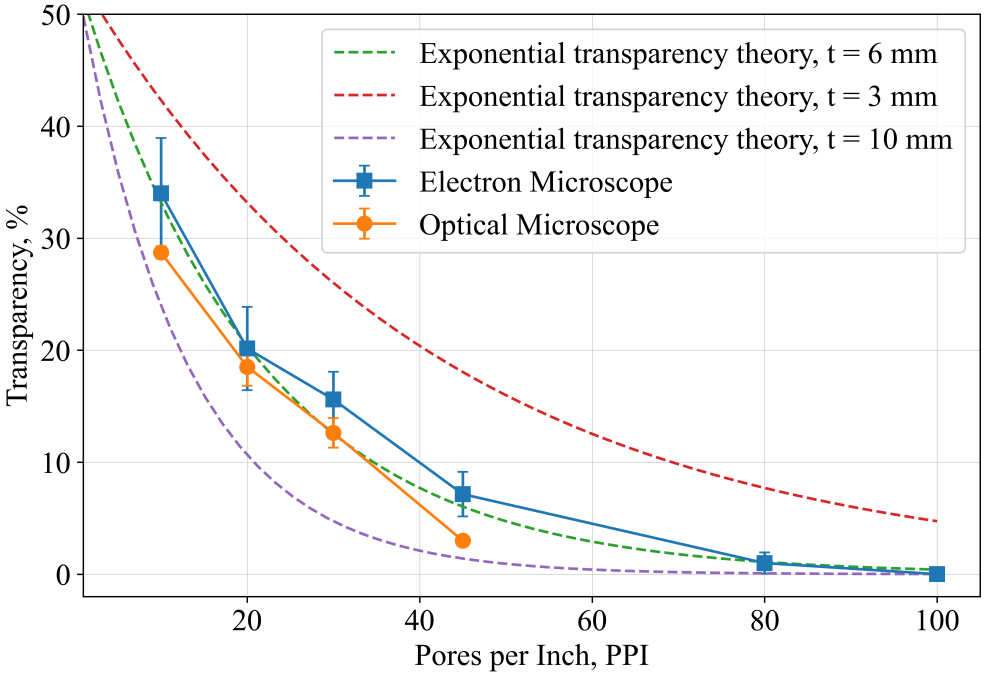

Figure 4.7: Transparency measurements from SEM and optical images are compared to an exponential decay described in Equation 4.9 The exponential decay theory shows that the transparency decays exponentially from the first pore layer. Foams with thickness of 3 mm are predicted to maintain higher transparency for each PPI than foams with 6 mm and 10 mm thicknesses.

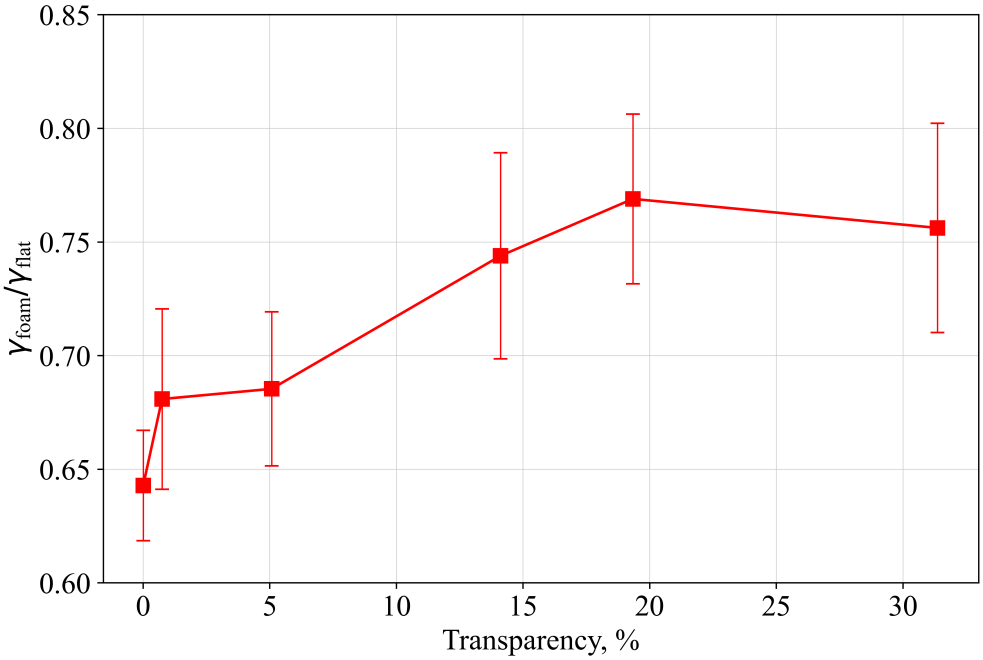

Figure 4.8: Average sample transparency with SEE yield. Each data point indicates a different PPI foam, from 100 PPI at $\approx 0\%$ transparency to 10 PPI at $>30\%$ transparency. The total change in SEE yield across this transparency range is $>20\%$.

III. By separating the foam ligament image region from the backplate image region (see Fig. 6), the reduction of SEE yield of the backplate, as well as the foam ligament SEE yield are calculated and are shown in Fig. 10. The backplate contribution to the total SEE yield in a foam with 34% is at most 16.6%, and quickly becomes negligible as the foam reaches <1% transparency.

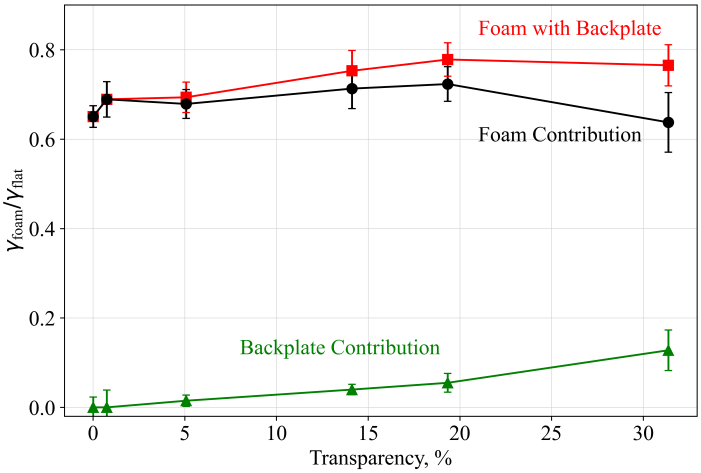

Figure 4.9: The SEE yield from the foam ligaments only and the backplate placed behind the foam are discerned and shown as a function of transparency. The 80 PPI and 100 PPI foams are <1% transparent to the backplate, thus their backplate contribution to the total SEE yield are negligible, and the SEE yield is solely comprised of ligament emitted secondary electrons.

4.2.4 Angular dependence of SEE yield for carbon foams

For flat and smooth surfaces, SEE has an increasing dependence on the angle of incidence of the primary electrons [58, 3]. Some featured surfaces, such as fuzzes, have shown a loss of angular dependence of SEE yield, while others such as velvets and grooved surfaces have shown a modification of the theoretical angular SEE yield function of a smooth surface. The angle of incidence is defined here as the angle between the primary electron beam and the normal to the target surface plane. Angular dependence studies were performed using the SEM sample stage tilt and two foams with 45 PPI and 100 PPI. The SEM stage was tilted by 0^o, 10^o, 20^o and 30^o, and SEE yield results were compared to two theoretical models: the simple secant law [3] and the fiber-foam analytical

approximation model by Swanson and Kaganovich [4]. The results from this analysis are shown in Fig. 11. In the secant law, the flat graphite SEE yield is increased by the secant of the primary electron angle of incidence. For each model, the initial value for 0^o incidence was given as the experimental SEM derived value.

It is found that the inverse cosine and the Swanson and Kaganovich models are within a 3% of each other for 0^o – 30^o angles of incidence of the primary electron beams, while the experimental SEM SEE yield values of carbon foam deviate by up to 10.5% for 45 PPI foam and 5.1% for 100 PPI foam. The results suggest that for foams with greater transparency to a flat backplate, the SEE yield angular dependence for a foam follows a flat graphite model more closely, while the non-transparent 100 PPI foam deviates from these models. The reduction of SEE yield for the 100 PPI carbon foam with $<$1% transparency is $>$26% for all angles measured. The suppression of secondary electrons from a foam surface at 0 - 30^o is thus more effective than theoretically predicted and is also greater than from velvet-type surfaces. For carbon velvets, the SEE from side surface of fibers becomes significant when tilting the surface, and SEE yield is predicted to increase by $>$25% for high aspect ratios over a 40^o tilt ([78]).

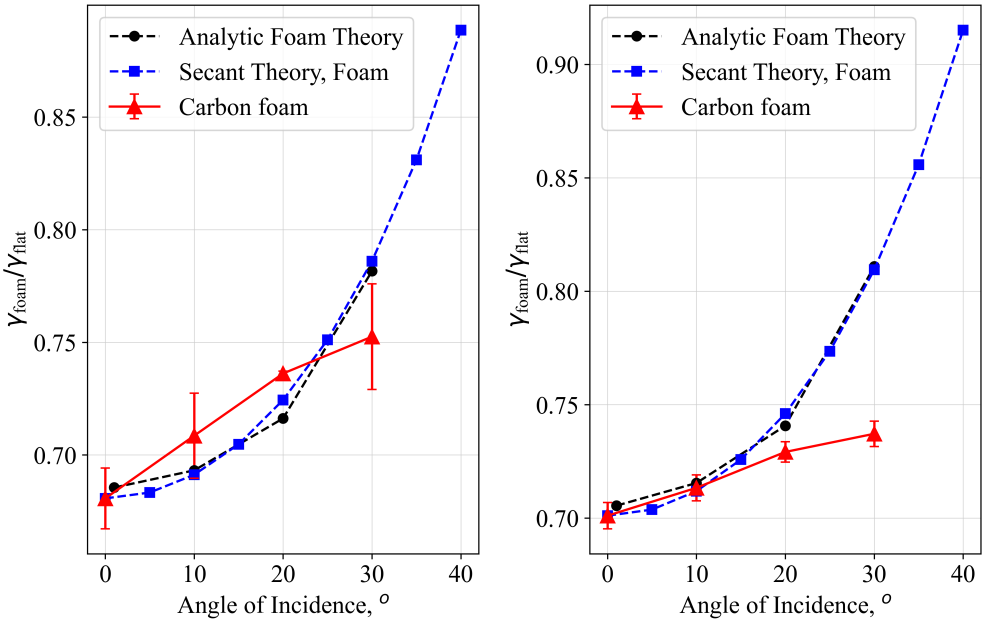

Figure 4.10: The SEE yield as a function of primary electron angle of incidence is measured for a (left) 45 PPI foam with 5% transparency and for a (right) 0 PPI foam with <1% transparency. The foam SEE yield is compared to two theoretical models: one is by Swanson and Kaganovich for carbon foams, and one is for a flat surface. The normalized SEE yield $\gamma_{foam}/\gamma_{flat}$ for 45 PPI carbon foam increases from 0.68 to 0.89 (by 31%) over 40^o while the 100 PPI foam increases from 0.70 to 0.92 (by 31%).

4.3 Direct SEE Measurement Chamber

Direct measurements of total SEE yield of the reticulated carbon foams were taken by using a dedicated experimental setup at the Princeton Plasma Physics Laboratory Nanolab and which has been described in Refs [60, 41]. The setup consists of a high vacuum chamber which has a base pressure of $1-5\times10^{-7}$ Torr and an ELG-2 Kimball Physics electron gun which produces electrons with a range of energy between 5 – 1000 eV. The maximum beam current to the target is kept $<$ 1 mA, while the filament emission current is 1.0 μA. An electrically isolated aluminum collector plate is attached to the electron gun and installed over the target sample to shield out stray electric fields. Figure 4.11 shows the chamber and electron gun power supply at PPPL. Figure 4.14 shows the setup inside of the direct SEE measurement chamber when using a reticulated carbon foam target sample with a graphite backplate on a x-linear stage. Two electrical configurations are shown for primary beam current measurements and sample current measurements used to infer the SEE yield.

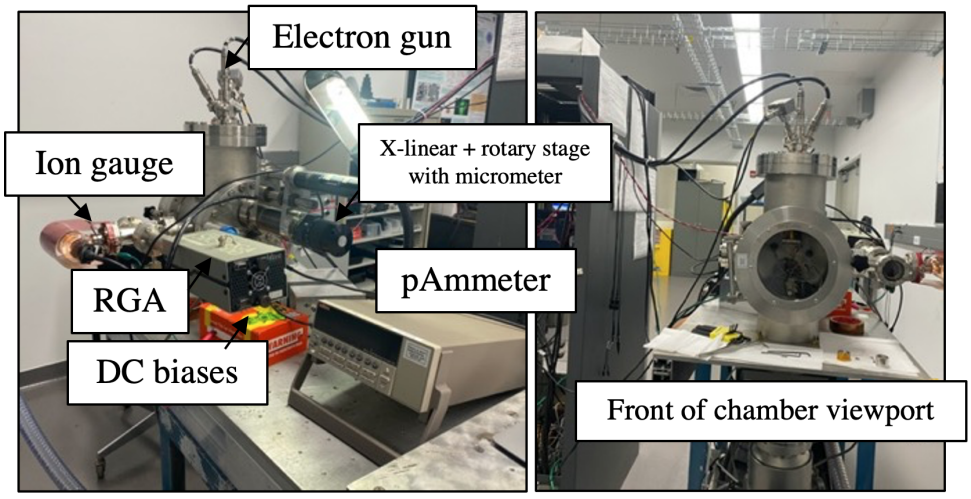

Figure 4.11: Direct SEE chamber and electron gun with x-linear stage setup.

4.3.1 Beam characterization with Faraday Cup

When measuring reticulated foams, the pore dimensions may range from a few μm – mm's, thus it was important to ascertain that the electron beam is large enough to cover more than one pore in a single measurement. The requirement for the electron beam diameter was thus determined to be:

$$\oslash_e >> D$$

where $\oslash_e$ is the electron beam diameter at the sample surface. A graphite Faraday cup with an entrance opening diameter of 0.5 mm was first used to characterize and center the electron beam before measuring the reticulated carbon samples. The Faraday cup was mounted onto a ceramic base which is attached to an aluminum arm with linear stage. The stage can be manipulated to move the Faraday cup manually from outside the vacuum chamber perpendicular to the electron beam. The electron beam profile was measured by positively biasing the inner pillar of the Faraday cup and recording currents with a picoammeter. Electron beam profile and shape depends on the primary energy and can be modified with the focus voltage settings. Guidance from data reported in the Kimball ELG-2 manual [ref Kimball] was used to select two focus voltage settings to characterize the electron beam for low (80 eV), middle-range (300 eV) and high (1000 eV) beam energies. These two focus voltages are F = 700 V and 200 V. Figure 3 shows the profiles with a Gaussian fit for each setting used. Based on these measurements, it was determined that the F = 700 V setting was suitable for all primary beam energies with a beam diameter which ranges from ϕ_e = 2-6 mm, which satisfies the electron beam diameter requirement. The beam center was also determined for each setting by finding the center of the Gaussian profile fits. Figure 4.12 shows Gaussian beam profiles acquired with a Faraday cup for different focus voltage and primary electron gun voltages.

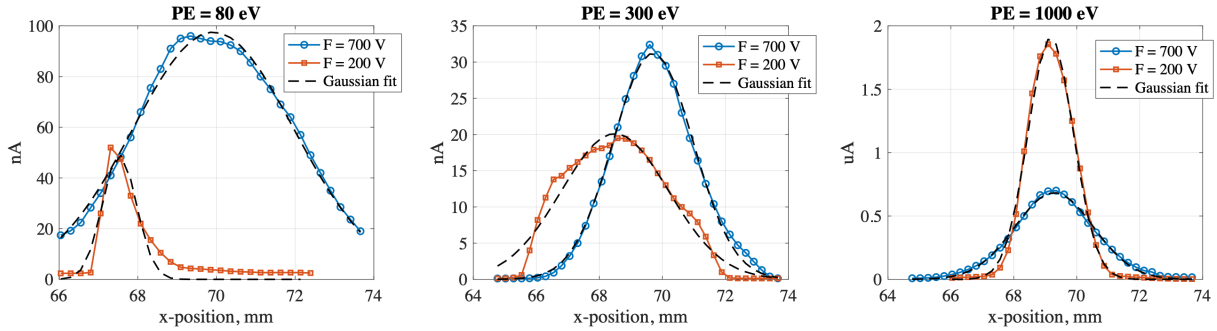

Figure 4.12: Primary electron current measured to an electrically grounded Faraday cup with a 0.5 mm diameter aperture versus position for three different electron gun incident energies of (a) 80 eV, (b) 300 eV and (c) 1000 eV and two focus voltage settings for each of F = 700 V (blue curves) and F = 200 V (red curves). The black dotted lines are Gaussian fits for each beam profile used to determine the beam diameters using $1/e^2$, and beam center location at each setting.

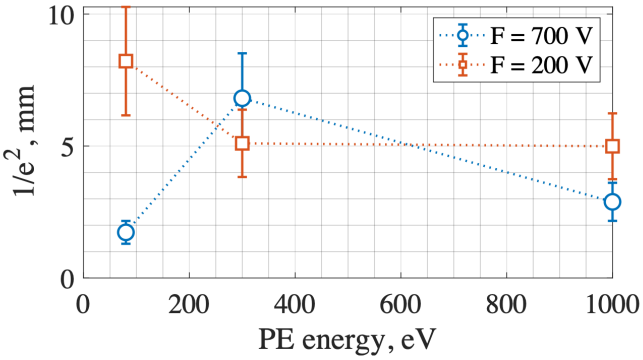

Figure 4.13: Beam diameters for different electron gun set-points.

4.3.2 Setup and SEE yield determination

For SEE yield measurements, a HOPG graphite plate was placed behind the carbon foams, as shown in Figure 3. This was done so that in the case of low PPI foams with nonzero transparency to the primary electron beam, SEs are generated from only carbon surfaces. The foams are each 6 cm x 3 cm x 6.35 mm while graphite disk has a 2.54 cm diameter and 0.1 cm thickness. The foams were bound to the graphite disk with a 22 AWG copper wire and were then placed onto a cylindrical aluminum sample holder. The aluminum holder was in turn mounted to a ceramic base so that the

sample could be electrically isolated and biased with respect to the electron gun. For the primary current measurement, I_{PE}, the sample was biased to + 72 V with respect to ground to suppress and collect SEs as well as measure the current coming from the electron gun. The collector was connected to ground. For the sample current measurement IS, the sample was connected to ground while the collector was biased to + 19.5 V. With this configuration, the sample current is $I_s = I_{PE} - I_{tot}$, where I_{tot} is the total SEE current comprised of SEs and BSEs which is directed to the collector. In addition, tertiary electrons from the chamber walls are prevented from being collected by the sample. The total SEE yield is then deduced:

$$\gamma_{tot} = \frac{I_{tot}}{I_{PE}} = \frac{I_{PE} - I_S}{I_{PE}} = 1 - \frac{I_S}{I_{PE}}. \tag{4.10}$$

It is important to recall that γ_{tot} includes both true secondary electrons and backscattered electrons, as described in Chapter 2.

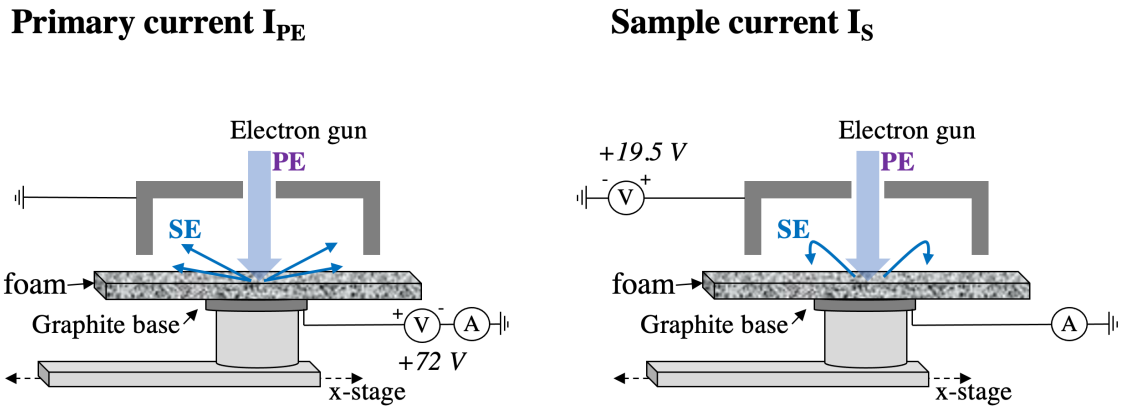

Figure 4.14: Diagram and electrical configuration for beam and sample current measurements using a reticulated carbon target with a graphite backplate.

Each reticulated carbon was measured at 5 adjacent locations on the surface so that an average spread in the SEE yield could be calculated. For measuring the incidence electron beam angle dependence of SEE yield, the sample stage was tilted around its central axis by -20^o to +35^o. In the case of a nonzero transparency foam, the SEE yield was measured with and without the graphite

backplate by moving the linear stage so that the electron beam can penetrate the foam in a region where there is no backplate. In Figure 2, this is where the foam hangs off the edge of the graphite plate past the reach of the aluminum arm mount. During a foam with no backplate measurement, a fraction of the electron beam proportional to the transparency of the foam is dumped to the chamber ground and not collected by the pico-ammeter.

4.4 Cylindrical Mirror Analyzer (CMA) for Electron Spectroscopy

For a complete analysis of SEE, a dedicated ultra-high vacuum chamber for surface science studies at the Surface Science and Technology Laboratory at PPPL was used for electron spectroscopy. The chamber has a base pressure of 1×10^{-8} Torr. A double pass Cylindrical Mirror Analyzer (CMA) from the Perkin Elmer Phi series model 15-255 normally used for Auger Electron Spectroscopy (AES) and X-ray Photoelectron Spectroscopy (XPS) was used to analyze secondary electrons from flat graphite and a reticulated carbon structure. The CMA consists of two concentric cylindrical electrodes which sit at different voltages. A coaxial electron gun is installed at the center of the CMA to produce a primary electron beam. Secondary electrons, both true and backscattered, are filtered through two different mechanisms: a first pass is achieved via discerning particles of a certain kinetic energy as a narrow band filter, and a second pass discerns particles with a trajectory of a determined radius.

The CMA used for these experiments has a constant pass energy and fixed resolution of 0.6% of the electron kinetic energies. The acceptance angle of emitted electrons for the target material is 10^o around a $42.5^o \pm 6^o$ angle. The CMA is used in conjuction with a Phi 20-805 electron analyzer control unit, a Phi 20-075 electron multiplier supply and a RBD instruments unit 147 for computer interfacing. The Software which communicates with the system is AugerScan. The electron multiplier increases the electron signal as a function of the analyzed K.E. Figure 4.15 shows a schematic diagram of a double pass CMA, taken from [80], and figure 4.16 shows raw signal from the CMA system and processed AES spectrum for a nickel Ni(110) crystal. The

increasing background signal as a function of SE K.E. is apparent in the raw signal in figure 4.16.

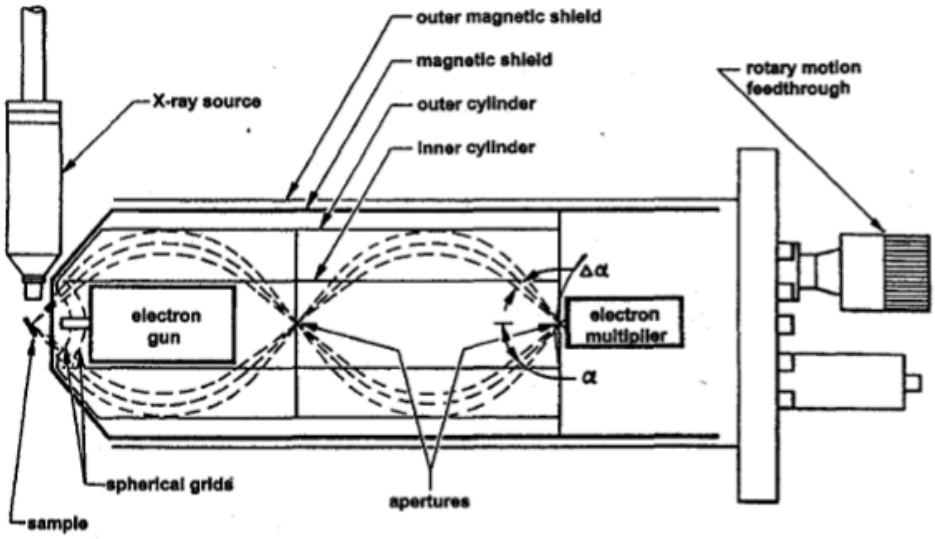

Figure 4.15: Diagram of a double-pass CMA with a coaxial electron gun and an X-ray source used for XPS. An outer spherical grid collects SEs generated from the interaction between the electron gun and the target sample, after which SEs are discerned by the outer and inner electrode potentials and then again by the geometrical path as they enter the second inner aperture. An electron multiplier then increases the electron count.

A nickel crystal Ni(110) was used to acquire AES spectra with the CMA system and for target sample alignment and calibration before introducing non-planar carbon structures. AES was performed on Ni surface before and after Ar sputtering. Figure 4.16 shows the raw AES data as well as the dN(E)/d(E) first order differential of the raw signal, which is typically used to remove the large background signal and more conveniently determine the spectral peak locations. It is important to note that the peak locations in the differentiated spectrum are at the crossover with the x = 0 axis. These Ni(110) spectra show the presence of carbon, nitrogen and oxygen with the Ni peaks before sputter cleaning, and a reduction of those peaks after Ar sputtering at with a fluence of 1.85 ions/cm^2. The peak in the low energy region (0 - 50 eV) is the characteristic true SE peak. The primary electron gun energy used to acquire these spectra was 3.0 keV. The electron multiplier voltage was determined by recording maximum counts as a function of multiplier voltage with sample current measured to ground of 10 nA. The multiplier voltage plateaus at 1,200,000

counts for a multiplier voltage of 1600 V. Thus, 1650 V was used as the multiplier setting for all measurements.

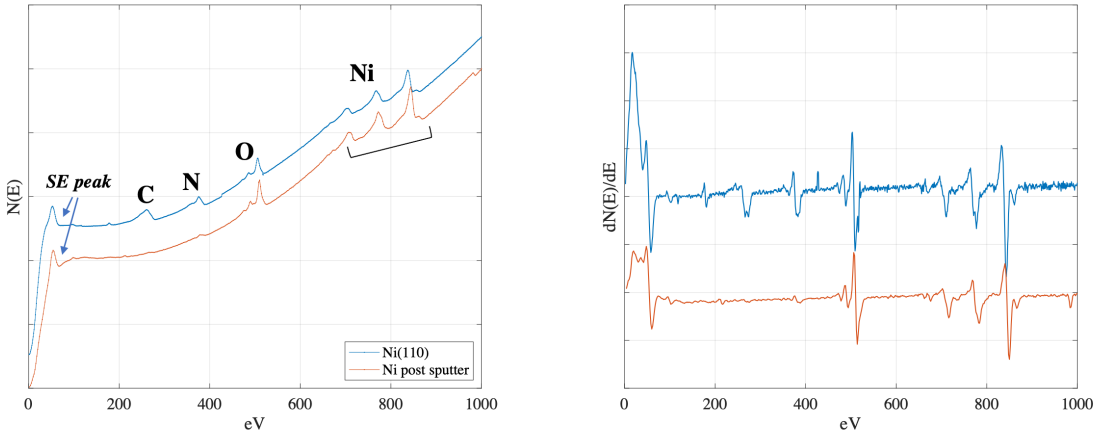

Figure 4.16: AES of a nickel crystal Ni(110) before and after argon ion sputter cleaning. (Left) raw signal shows an increasing background signal as a function of electron energy, and (right) differentiated signal typically used for AES peak determination. The primary electron gun energy for these spectra is 3 keV.

This setup will be used for examining the total secondary electron energy distribution function (SEEDF) from planar and non planar carbon surfaces described in chapter 4.

4.5 Direct SEE Measurement Results

Four reticulated carbon foams manufactured by ERG Aerospace Duocel [81, 82] were analyzed in these experiments. Similar foams were used in recent work [6] where SEE yield was estimated using Scanning Electron Microscopy. Figure 4.17 shows optical images of the foams measured in these experiments. Reticulated foams are geometrically characterized by their average pore diameter, D and ligament diameter, d. A common linear metric for foam materials is Pores Per Inch (PPI), which, as previously stated in 3, is defined as

$$PPI = \frac{1\,\text{inch}}{D+d}$$

as well and their aspect ratio $A_R = D/d$.

The transparency, τ, was calculated for each of the foams used in the direct SEE yield experiments and was found to vary from ≈ 0 transparency for a 100 PPI foam to 20% transparency for a 5 PPI foam. Because of this range in transparencies, it is important to carefully consider any backplate contribution to SEE yield. To this end, a planar HOPG graphite disk was mounted in combination with carbon foams.

Figure 4.18 summarizes the foam sample geometric properties. It is important to note that often the indicated manufacturing PPI of a foam is not the actual measured PPI of the foam received. This is critical when comparing SEE model results to SEE experimental measurements where the input parameters are geometric variables such as A_R, d, and D. Several images of each foam used in the SEE yield direct measurement experiments were taken by an optical microscope and scaled using Motic Imaging Software. The foam properties reported in Figure 4.18 were generated from averaging 25 ligament and pore diameters of each foam sample.

4.5.1 SEE yield with energy

Four carbon foams and flat graphite were measured for their SEE yield as a function of incident electron energy, and results are shown in 4.19. The flat graphite has a maximum yield of $\gamma = 0.89$ for a primary energy of 300 eV, which is within 5% agreement with previous measurements taken in the same setup [65], and the carbon foams follow a similar increasing for 0 - 300 eV and decreasing for $>$ 300 eV primary energy trends. The reduction of SEE yield compared to a flat is also shown in 4.19. It is interesting to note that at low primary energies $<$ 100 eV, the SEE yield reduction between a foam and a flat converges for 30, 100 an 40 PPI foams. This could be due to SEs which approach the primary energies in this regime, thus resulting in additional SE trapping during the sample current measurement, and increasing the effective yield. The maximum reduction is achieved for the 40 PPI foam at all energies, with 44% yield reduction compared to flat graphite.

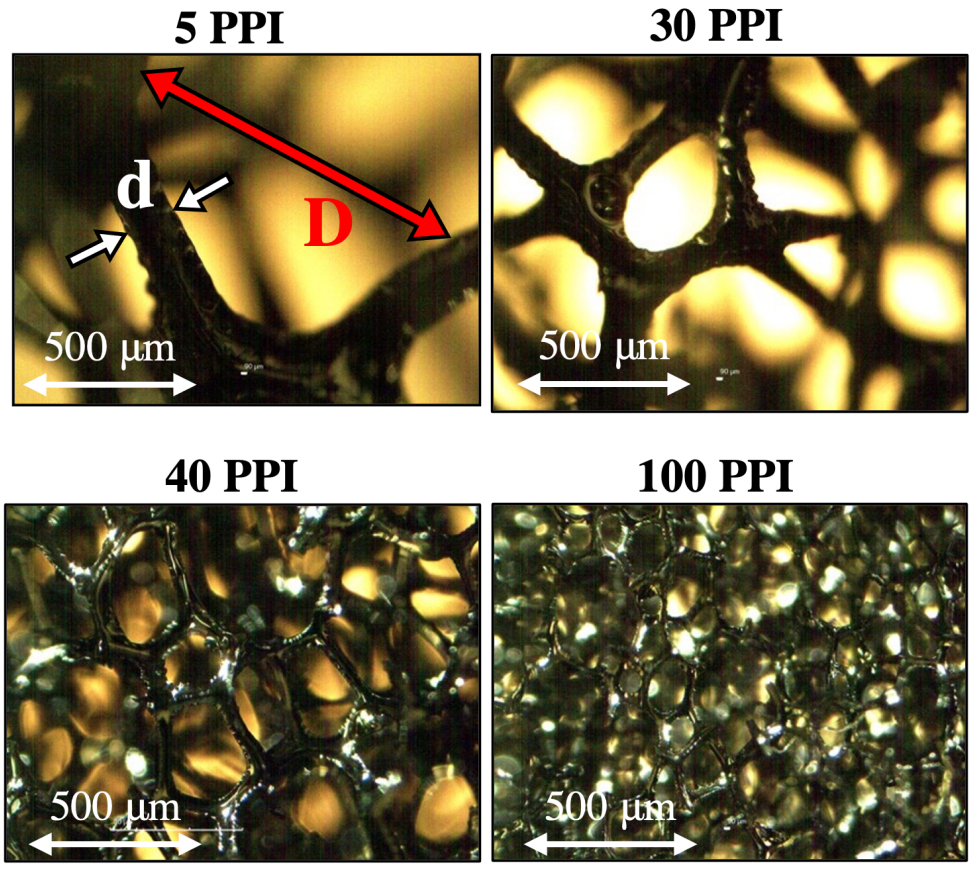

Figure 4.17: Select optical microscope images of foams used for SEE yield. The PPI was calculated by averaging 25 measurements of pore and ligament diameters from each carbon foam.

Indicated PPI	Measured PPI	D [µm]	d [µm]	A_R= D/d	T [%]
10	5	1370 ± 150	320 ± 58	4.3	20
30	30	1060 ± 122	200 ± 44	5.3	10
60	40	590 ± 80	70 ± 20	8.4	5
100	100	210 ± 32	45 ± 12	4.7	0.1

Figure 4.18: Geometric properties of the reticulated carbon foams used in direct SEE yield measurements. Each foam has same thickness of 6.35 mm. The indicated PPI is given by the manufacturer while the measured PPI is calculated from measuring scaled microscope images of the foams.

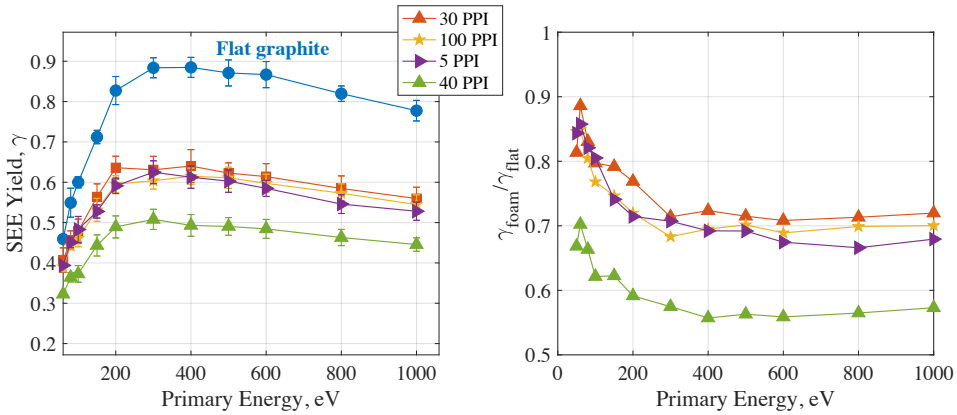

Figure 4.19: (Left) Total SEE yield of flat graphite and four foams with different PPIs as a function of incident primary electron energy. Each data point is an average of five adjacent locations across the sample surface (right) reduction of yield compared to flat graphite for foam as a function of primary energy.

4.5.2 SEE yield with angle of incidence

Foams with 5 and 100 PPI were tilted on the sample stage to analyze their SEE yield as a function of electron angle of incidence. Planar graphite is expected to increase in yield roughly as a function of sec θ_i where θ_i is the angle of incidence, as described in Chapter 2. By moving the x-linear stage, it was also possible to measure the 5 PPI foam with and without the graphite base, as shown in 4.14. The 5 PPI foam has a transparency of 20% and therefore it is important to measure the backplate contribution to the total SEE yield. Figure 4.20 shows results for 5 PPI with and without a backplate, for 100 PPI foam and for flat graphite.

The SEE yield for 5 PPI without a backplate is monotonically decreasing for angles between -15 and 15 degrees, and then flattens as a function of θ_i. The increased yield could be where the ligament side area is primarily exposed to the beam. As the foam is tilted, the yield may decreases as the beam becomes more aligned to the average ligament direction. This suggests that a low PPI foam is directional in it's geometry. The same foam with a backplate however appears to be symmetric around 10-15 degrees. The 5 PPI foam might have ligaments which are, on average, tilted by 10-15 degrees. When the foam is "upright" at this angle, the backplate becomes most visible to the primary electron beam, which decreases the yield on average compared to when there

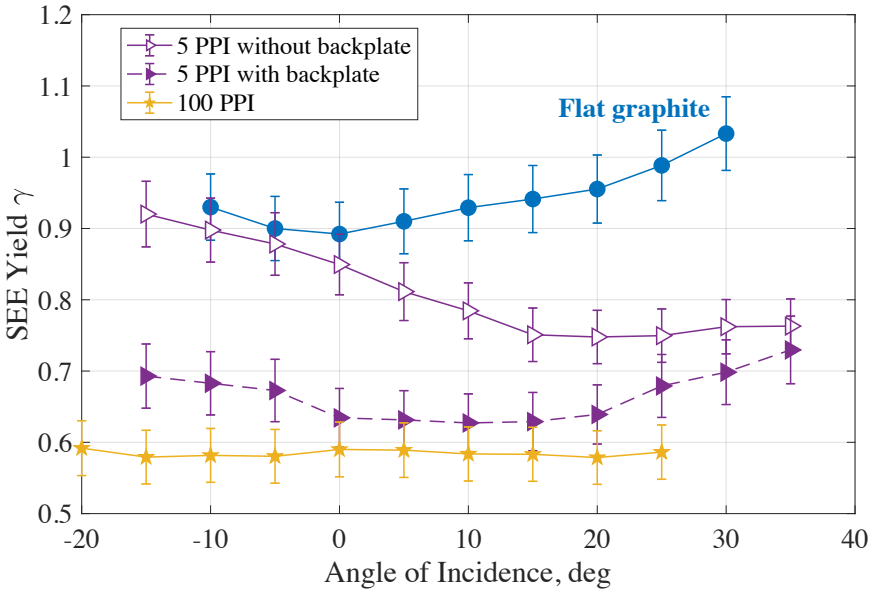

Figure 4.20: Total SEE yield as a function of primary angle of incidence. Measurements are shown for planar flat graphite, reticulated carbon foam with largest pores (5 PPI) and 20% transparency with and without a backplate, and foam with smallest pores (100 PPI) with 0% transparency.

is no backplate. While tilting the foam further, the transparency of the backplate to the primary beam decreases once more, and the yield increases. Further testing of this hypothesis could be carried out by tilting a low PPI foam under a microscope and measuring the transparency for each angle.

Notably, the 100 PPI foam shows a loss of angular dependence with the primary electron beam. This result is similar to measurements taken of plasma-generated tungsten fuzz [77]. 100 PPI foam has ligament and pore dimensions between 10 - 80 μm which is up to 100 times smaller than the electron beam diameter. It is possible that for such small features, the isotropic nature of the foams results in an average reduced SEE yield for each primary beam angle.

4.5.3 SEE yield with PPI

Each carbon foam was also analyzed for its SEE yield behavior as a function of PPI for a fixed primary energy of 300 eV. The results are shown in 4.21 in comparison with two analytical models which were described in chapters 3 and 4, respectively AMPS-E (or Li Wirz Ottaviano), and the Swanson and Kaganovich model. In addition, the direct SEE yield measurements were compared to SEM measurements also reported in Chapter 4 and in [6]. Agreement within 6% between AMPS-E and the PPPL direct measurements is shown, and within 18% between the Swanson and Kaganovich model and direct PPPL measurements. An optimal regime for SEE suppression is revealed for 40 PPI foam, which is confirmed by both models. The optimum foam configuration could be explained by noting that the 40 PPI foam has an aspect ratio $A_R = 8.4$, while the other foams, including those measured in the SEM experiments, have aspect ratios between 4.3 and 5.3.

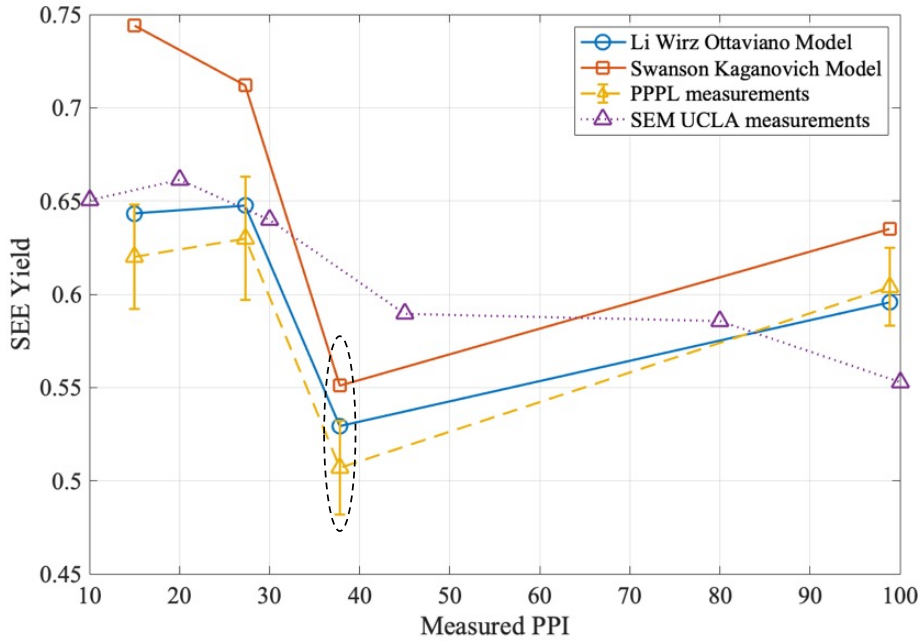

Figure 4.21: Direct measurements taken at PPPL for four carbon foams are compared to two models [5, 4] and to previous SEM measurements [6]. An optimal SEE suppressing configuration is shown and confirmed with these models for 40 PPI carbon foam and circled by the black dotted outline. This foam and the computed model inputs have aspect ratio of $A_R = 8.4$, while the SEM data points are of foams with $4.3 < A_R < 5.3$.

4.6 SEE Energy Distributions with a CMA

The following results were taken at the Surface Science and Technology Laboratory at the Princeton Plasma Physics Laboratory using a Cylindrical Mirror Analyzer with a coaxial electron gun, an electron analyzer, an electron multiplier, and a PC interface unit provided by RBD istruments. Details of this setup are described in Chapter **??**. The chamber setup is shown in Figure 4.22. A 5 mm $\times$ 5 mm $\times$ 3 mm 100 PPI carbon foam was places above an equivalently sized flat graphite sample. The graphite and carbon foams are vertically mounted with tantalum wires which are spot-welded onto a tantalum shaft. The vertical shaft is controlled by a motorized stage, so that either the graphite or the foam can be aligned to the electron gun and CMA system for measurement.

Electrically, the sample is connected to a picoammeter and in series to ground so that the collected current from the electron gun can be monitored. The current measured to the sample is:

$$I_{measured} = I_{PE} - I_{SEE,tot} \tag{4.11}$$

where I_{PE} is the primary electron gun current and $I_{SEE,tot}$ is the total secondary electron current which is comprised of both true secondary electron current, I_{SE} and backscattered electron current, I_{BSE}. Each measurement was taken for three graphite and foam locations and averaged. Example spectra from the flat graphite at primary energies of 100, 200, 300, 400 and 500 eV are shown in Figure 4.23. The resolution of the spectrum is 0.5 eV, and the dwell time for each data point is 80 ms. The increasing background signal due to the electron multiplier was removed by dividing each spectrum by the kinetic energies [83].

An individual set of spectra for the flat graphite sample and the foam sample are shown in Figure 4.24, for a primary energy of 300 eV. The measured currents to the sample are typically between 100 - 500 nA for primary energies between 100 and 1000 eV. This type of energy spectrum analysis allows for the comparison of true secondary and backscattered secondary electron behavior between a flat graphite and a foam structure.

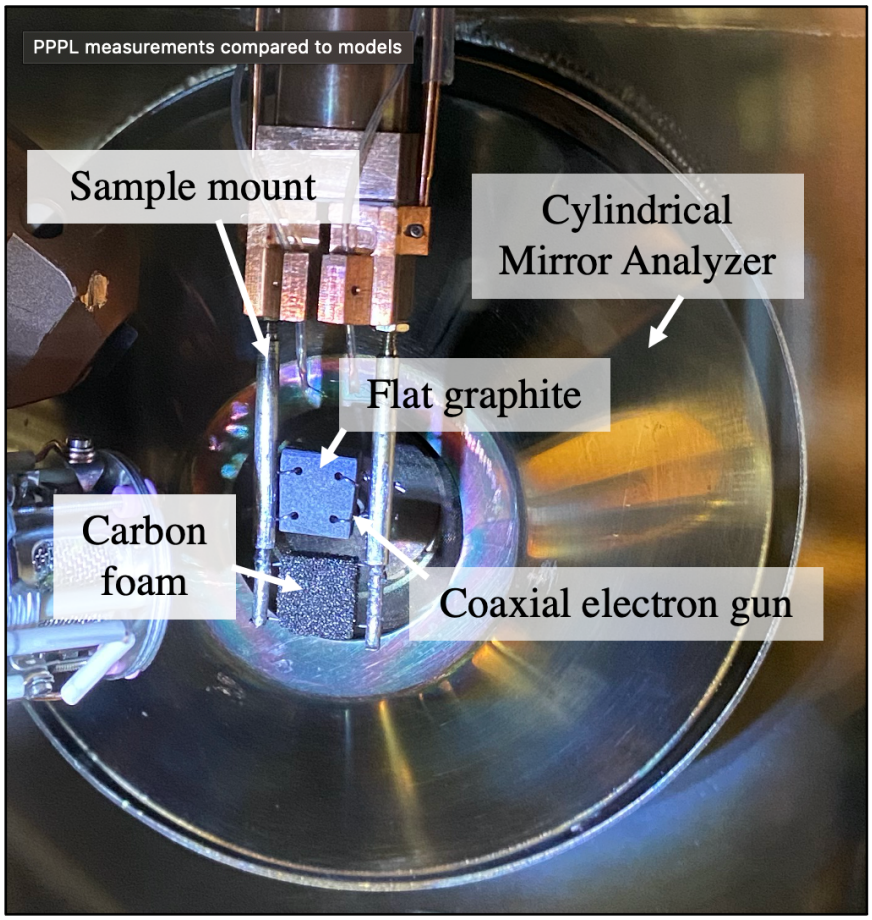

Figure 4.22: CMA with samples and coaxial electron gun. The sample post can move vertically with a motorized stage so that the graphite and foam can be positioned at the CMA and electron gun focus for consecutive measurements.

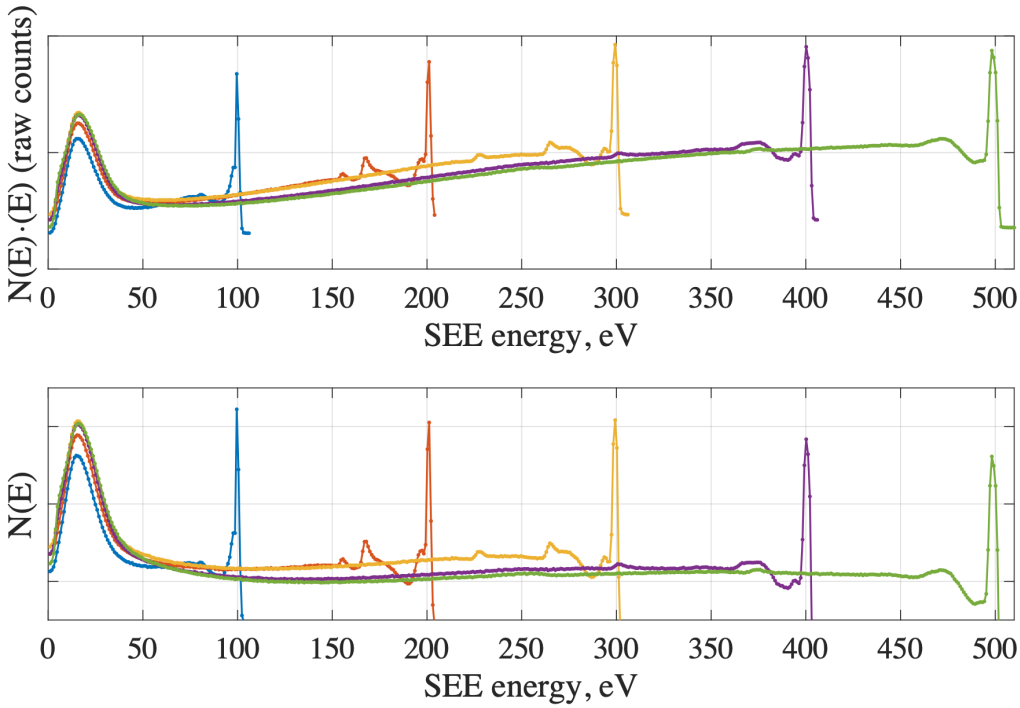

Figure 4.23: Semilog plot of raw energy spectra from flat graphite (top) and divided by electron multiplier signal which increases counts proportionally to SEE energy (bottom). Curves for primary beam energies of 100, 200, 300, 400, and 500 eV are shown.

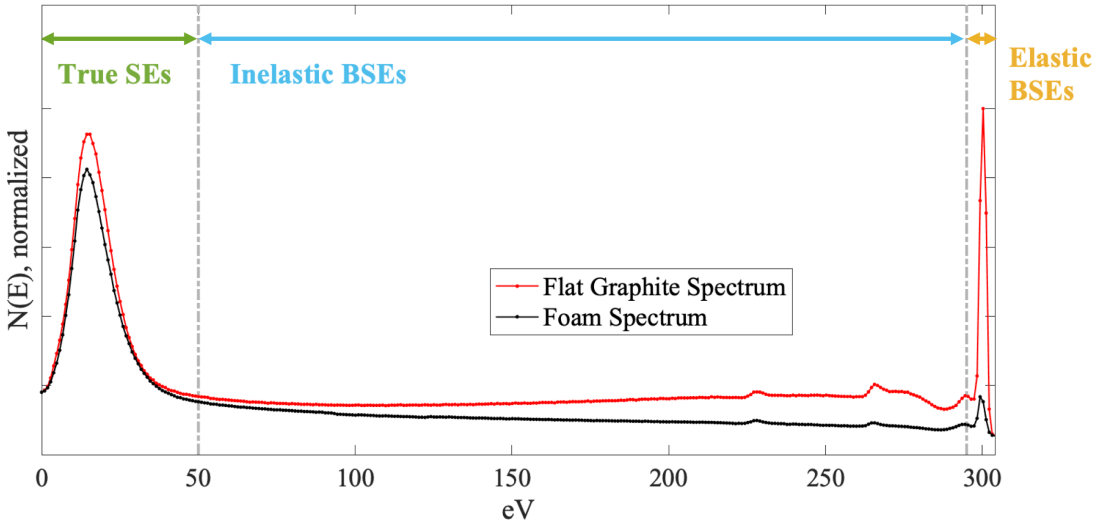

Figure 4.24: EEDF of flat graphite compared to 100 PPI foam for a primary electron beam energy of 300 eV. True SEs are between 0 – 50 eV, iBSEs between 50 eV and the primary energy (PE) minus 5 eV, and eBSEs are between the PE ±5 eV. The SE peak is reduced by 15% while the eBSE peak is reduced by 85% for this EEDF.

Calculation of reduction of SE counts between a flat and a foam sample for true SEs, for iBSEs and for eBSEs are also performed directly from these spectra by integrating sections of the curves:

$$N_{SE,true} = \int_{0}^{50eV} n(E)dE \tag{4.12}$$

$$N_{iBSE} = \int_{50eV}^{PE-5eV} n(E)dE \tag{4.13}$$

$$N_{eBSE} = \int_{PE-5eV}^{PE+5eV} n(E)dE \tag{4.14}$$

and the total SEE signal (in arb. counts) is

$$N_{SEE,tot} = \int_{0}^{PE+5eV} n(E)dE. \tag{4.15}$$

The SEE yield can also be calculated with this data by using $I_{measured}$ to find I_{PE} from Equation 4.15, and by multiplying by a factor F found from the direct SEE measurements to convert electron counts to SEE current:

$$\gamma_{tot} = F\frac{I_{SEE,tot}}{I_{PE}} = \frac{I_{SEE,tot}}{I_{measured} + I_{SEE,tot}} \tag{4.16}$$

and then relative contributions of SEE populations (true SEs, iBSEs, eBSEs) to the total SEE yield can then be found using the CMA electron enregy spectra:

$$true\ SE[\%] = \frac{\gamma_{SE\,true}}{\gamma_{tot}} \tag{4.17}$$

$$iBSE[\%] = \frac{\gamma_{iBSE}}{\gamma_{tot}} \tag{4.18}$$

$$eBSE[\%] = \frac{\gamma_{eBSE}}{\gamma_{tot}}. \tag{4.19}$$

Performing these calculations allows for insight on the generations and suppression of secondary electrons in flat compared to foam surfaces, and are used in the following results.

4.6.1 Reduction of low-energy (true) SEs and BSEs

The SEE currents were found by integrating the indicated sections of curves shown in Figure 4.24, and the total current was found by integrating the entire CMA curve. These results are shown in Figure 4.25. The true SE peak is reduced by $\approx$ 20 % while the elastic backscattered peak is reduced by up to 70% when comparing a flat surface to a foam surface.

The relative contribution to the total SEE yield was also calculated from the CMA data and compared with previous findings from Patino et al. [79]. The range of % contributions are from a primary energy of 100 eV to a primary energy of 1000 eV. Note: in Patino et al. work, the term

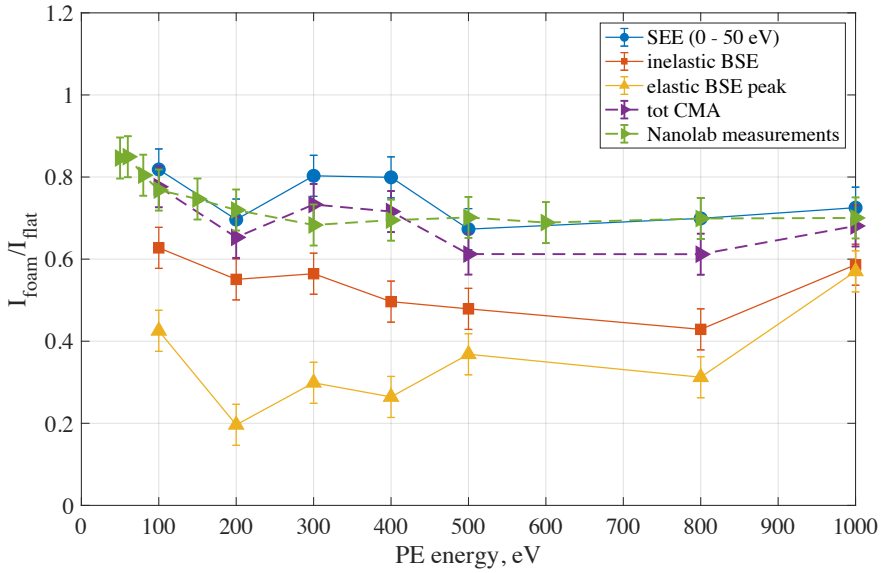

Figure 4.25: Total SEE yield reduction within 8% agreement with direct measurement results. The true SE peak reduced by ≈20% but BSE is reduced by ≈60 to 70% compared to the flat graphite.

"rediffused electrons (RE)" are indicated as "iBSE" in this work. The results are shown in Figure 4.27, and show that the contribution of true SEs to the total SEE is larger for a foam than for a flat graphite sample. This implies that while the reticulated carbon foams are effective at trapping scattered, or specular electrons, the generation of low energy, true SEs may be enhanced. This results is important for applications of electron emissive surfaces.

% of γ_{tot}	**Flat graphite** (PE = 100 eV - 1.0 keV)	**Patino et al.** (PE = 100 eV - 1.0 keV)	**Foam 100 PPI** (PE = 100 eV - 1.0 keV)
True SE	83 – 63	80	87- 70
iBSE	12 - 35	19	10 - 29
eBSE	5 – 2	< 2	3 – 0.5

Figure 4.26: Relative % contribution of true SEs, iBSE and eBSE to total SEE yield calculated for flat graphite, foam, and compared with previous work by Patino et al. for flat graphite.

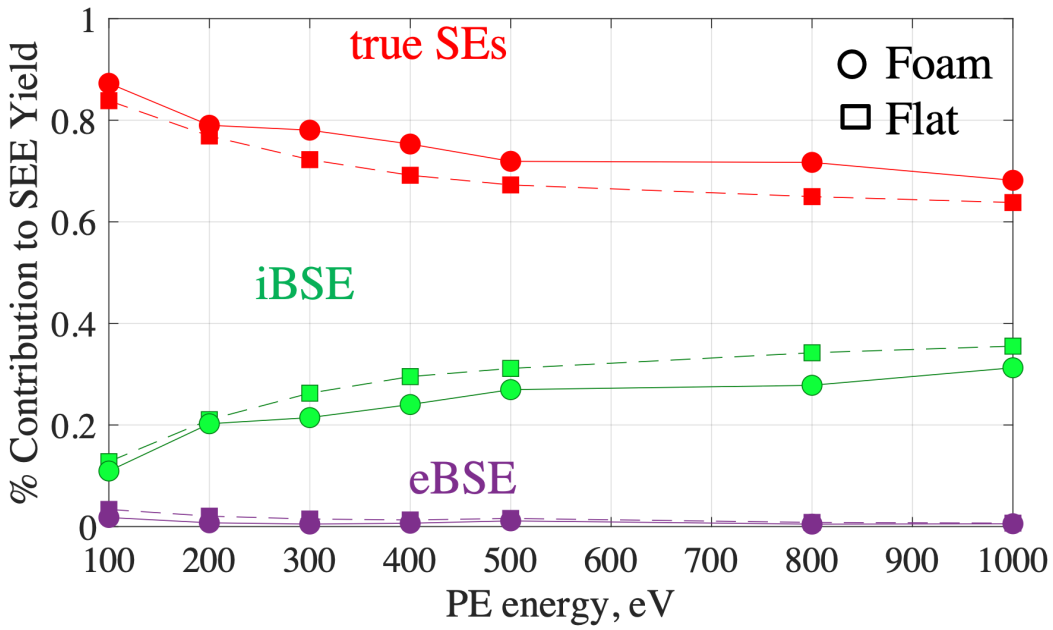

Figure 4.27: Relative % contribution of true SEs, iBSE and eBSE to total SEE yield calculated for different primary energies are shown. These results suggest SE is enhanced by 2-5% from foam surfaces, while BSEs are suppressed. However, the contribution of iBSE and eBSE to the total yield is $< 40\%$ at every energy.

4.7 SEE Modeling Results

4.7.1 Varying primary energies for ion and electron-induced SEE

AMPS-E was used to compute the SEE yield and IIEE yield for energies of primary electrons and ions varying from 0 to 1000 eV and for 10, 45, and 100 PPI foam and compared with SEM-derived experimental measurements. IIEE is shown for both singly charged xenon ions impacting a carbon and tungsten surfaces. The reduction of SEE and IIEE yields are in agreement of up to 38% compared with a backplate. SEE measurements show that the lowest SEE yield is found for a 45 PPI foam which, for a 6 mm foam thickness, has a transparency of $\approx 5\%$. The modeled results however show the most reduced SEE yield for a 100 PPI foam which has nearly 0% transparency to a backplate. The discrepancy between modeled and measured values could be due to several factors: real foams often have many sharp edges due to broken ligaments on their top layers, causing sharp SEE yield emission peaks. These edges and ridges are not accounted for in AMPS-E. In addition, the errorbars from the measured values are too large to be able to definitevely conclude which of the 45 or 100 PPI foam has the largest reduction of yield for all measured energies. The IIEE yield results from AMPS-E show that IIEE yield is $< 11\%$ of that from SEE yield, but is still non-negligible in applications where energetic ions impact materials surfaces such as in electric propulsion facilities and gridded ion thrusters. The IIEE yield is linearly increasing as a function of primary ion energy due to ion-induced electron generation occurring closer to the material surface compared with electrons which penetrate a material by up to 10s of nanometers. The SEE curve increases initially due to increased SEE generation until the escape depth of the electrons overcomes the increased SEE generation after $E_{PE,max}$. This occurs for much higher ion energies in IIEE, beyond the limits of these simulation energies. IIEE yield for carbon and tungsten foams range from 0 to 0.071 for 10 PPI foams with 36% transparencies.

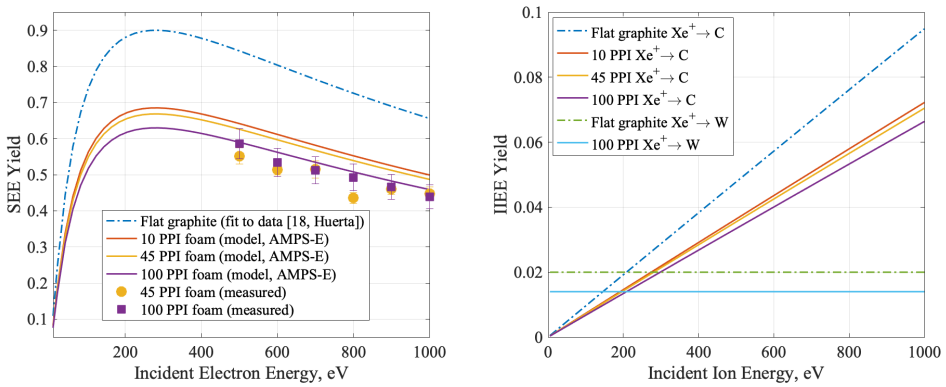

Figure 4.28: (Left) SEE yield computed from AMPS-E for 10, 45 and 100 PPI foams compared with SEM-derived SEE measurements and compared with a flat surface. (Right) IIEE yield computed using AMPS-E for single charged xenon ions impacting carbon and tungsten foams and flat surfaces. In both cases, the electron emission yield reduction is of up to 38% compared with a flat surface with no geometric trapping.

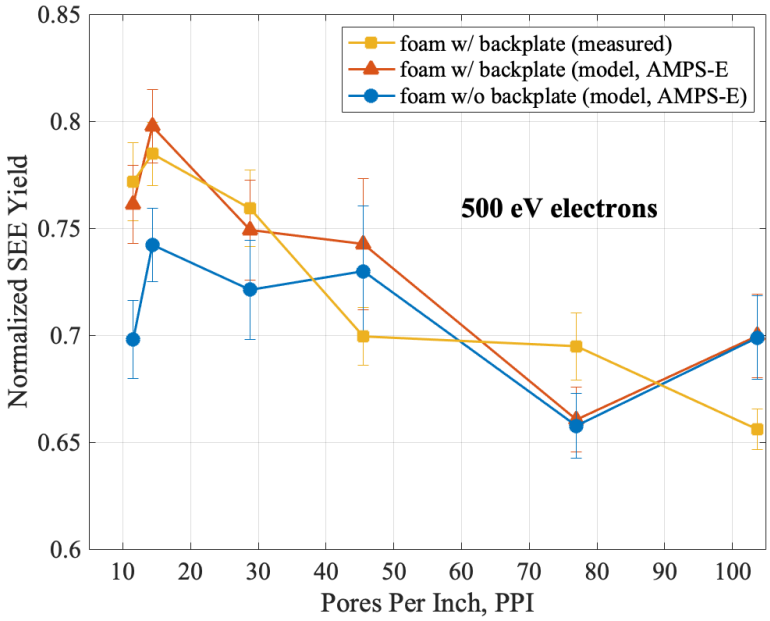

Figure 4.29: SEE yield as a function of Pores Per Inch for primary electron energies of 500 eV. Curves are shown for SEM-derived SEE yield measurements as well as foam SEE yield with and without backplates calculated using AMPS-E.

4.7.2 SEE yield vs Pores Per Inch (AMPS-E)

SEE and IIEE yields were also computed using AMPS-E for a variety of PPI foams with a 6 mm thickness so that they could be compared with experimental results. The primary energies of electrons and ion are both 500 eV. The errorbars are calculated from spreads measured in the foam ligaments and diameters propagated into SEE yield values. Both foams with and without backplates are shown in order to demonstrate the contribution of yield from a backplate is exponentially decreasing with increasing PPI (and therefore reduced transparency). 100 PPI foams have almost no transparency to their backplates at 6 mm thickness, which is why 100 PPI SEE and IIEE yields are nearly the same with and without backplates. The AMPS-E model predicts the trends of SEE yield compared with experimental measurements within a few percent for 10, 20 and 30 PPI foams, but deviate for higher PPIs. It is important to note that the effective PPIs of the measured and computes foams deviate slightly from the manufacturing indications of 10, 20, 30, 45, 80 and 100 and have been measured and reported in Table I.

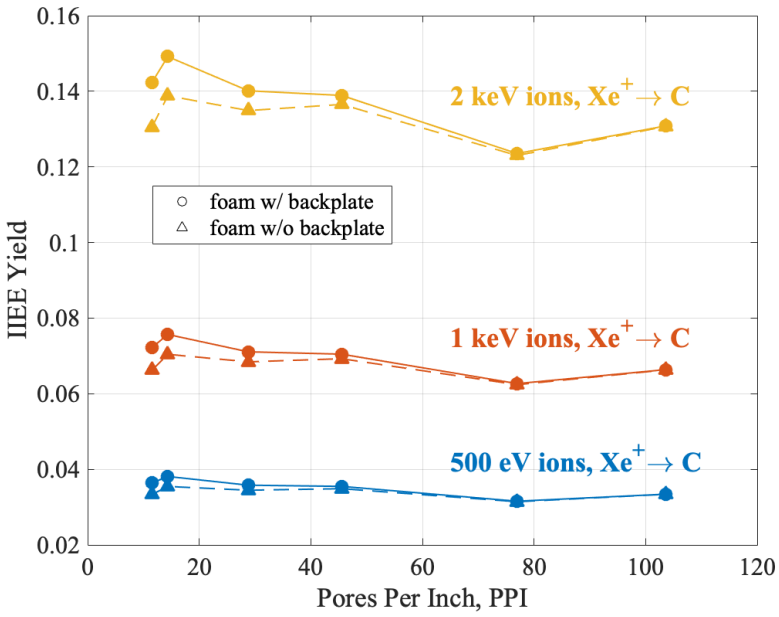

Figure 4.30: IIEE yield as a function of PPI for primary ion energies of 500 eV. Curves are shown for IIEE yield with and without backplates calculated using AMPS-E.

IIEE yields for foams varying from 10 to 100 PPI are $< 10\%$ of their SEE yield counterparts, with an increasing linear energy dependence. The variation of electron yield across different PPI foams is also weaker for IIEE than SEE yield, which suggests that IIEE yield is roughly constant for foams with a fixed thickness and aspect ratio A_R.

Carbon foams with 3% volume density and a fixed aspect ratio of $1/A_R = \frac{d}{D} = 0.2$ have been characterized for their SEE and IIEE properties using SEM and using an analytical model which approximates a foam to a cage geometry. Compared with carbon fibers or velvet surfaces, carbon foams are rigid structures, which reduce geometric variation across a foam. This also implies that the backplate contribution per foam, characterized by sample transparency, is more consistent than in a carbon fiber sample due to less bending and tilting of fibers and pillars. The volumetric nature of foams also allows the structure to be more scalable in manufacturing, rather than a pillared surface which scales with fiber height, but the volumetric structure does not remain isotropic. It was found that transparency is a useful metric for characterizing sample geometry and SEE yield, and with SEM it is possible to distinguish backplate SEE contribution. The isotropic nature of reticulated carbon foams allows sustained suppression with angular primary electron beam energies. A model, AMPS-E, which is a variation of a recently developed model for ion-induced sputtering, AMPS, has been successfully implemented for both SEE and IIEE of carbon foams using primary electrons and primary xenon ions on carbon and tungsten targets. Results are consistent with measured values with a maximum reduction of electron yield of 38% for 3% volume fill density carbon foams of 6 mm thickness.

The modeled results of SEE yield from foams using AMPS-E will be used in 4 to compare with experimental findings from scanning electron microscope measurements, also reported in [6] and from direct SEE measurements taken at the Princeton Plasma Physics Laboratory. In addition, AMPS-E generated results are also compared to other computational and analytical models such as developed by Swanson and Kaganovich [4].

CHAPTER 5

Plasma Sputtering, Erosion and Material Transport

This chapter describes two experiments for the demonstration of plasma infusion and of plasma-material transport across the layers of foam materials. The results are a qualitative description of the phenomena of plasma-infusion into a VCM and are part of ongoing work on plasma-material transport and inter-deposition due to ion sputtering.

5.1 Plasma-interactions facility (Pi)

The Plasma-interactions (Pi) facility at UCLA consists of a 250 A lanthanum hexaboride (LaB6) hollow cathode that feeds an axial magnetically confined plasma column that is focused to a downstream target sample [26, 84, 85]. The chamber has a base pressure of 10^{-6} Torr and operates at a pressure of 10^{-4} Torr during plasma operation. The sample can be biased negatively with respect to the plasma potential to enable energetic ion bombardment for sputtering and erosion studies. A schematic of the Pi facility is shown in 5.2. The magnetic field near the target was designed to enable diagnostic access to the near-target region where plasma-induced sputtering, deposition, and re-deposition processes are concentrated. The operating conditions of the Pi experiment have been well characterized [43, 42] and are listed in Table **??**.

For evaluation of the bulk plasma and near-surface plasma properties, a range of diagnostic capabilities are used in concert with the Pi facility. As shown in **??** and Figure 5.2, these include semi-intrusive and non-intrusive in-situ diagnostics, as well as ex-situ surface analysis techniques are used for pre- and post-plasma sample evaluations.

Table 5.1: Experimental parameters of the Pi facility.

Parameter	Typical Values
Plasma density	$10^{18} m^{-3}$
Electron temperature	7 eV
Ion energy to target	40 to 300 eV
Ion flux to target	$10^{17} cm^{-2} s^{-1}$
Exposure diameter/area	$1.5cm / 1.8cm^2$

Plasma and material diagnostics include a Langmuir probe, a Faraday probe, a quartz crystal microbalance (QCM) for measuring sputtering yield, optical emission spectroscopy (OES) to monitor the chemical composition of the near-target region plasma, and a long-distance microscope (LDM). The LDM is a Questar 100 unit based on a Maksutov-Cassegrain design with a working distance of up to 35.6 cm with a resolution of $3\ \mu m$. The specifications of the numerical aperture (NA) of the LDM in relation to working distance (WD), depth of field, and resolution are listed in Table 5.2.

Table 5.2: Specifications of the Questar 100 LDM.

WD [cm]	NA	Depth of Field (μm)	Resolution (μm)
15.2	0.141	27.4	1.95
25.4	0.110	45.4	2.51
35.6	0.076	95.9	3.64

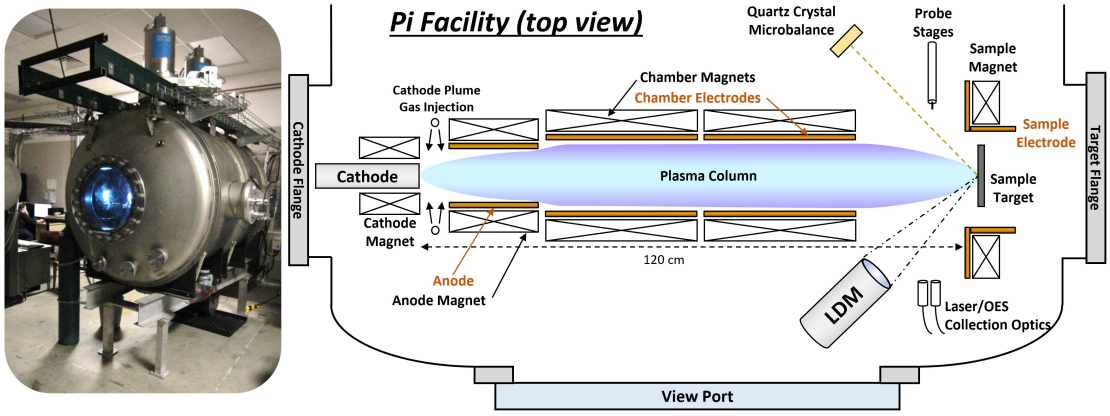

Figure 5.1: Top view schematic of Plasma Interactions (Pi) facility at UCLA. The hollow cathode-generated plasma is magnetically confined and focused downstream onto a material target with a final area of 1.8 cm^2. A suite of plasma and material diagnostics are included in the chamber to investigate the plasma and plasma-material interactions at the target.

Type	**Diagnostic**	**Measured Parameters**
Non-intrusive	Quartz Crystal Microbalance (QCM)	Differential sputtering rate, sputtering yield
	Long Distance Microscope (LDM)	Surface visualization, morphology, height mapping
	Optical Emission Spectroscopy (OES)	n_e, T_e and n_n of plasma and sputterant species
	Laser Induced Fluorescence (LIF)	Ion/neutral velocities
	Laser Absorption Spectroscopy (LAS)	n, T of plasma and sputterant species
	Witness Plates	Combined with ex-situ capabilities reveals deposited sputterant composition
Semi-intrusive	Langmuir Probe	n_e, T_e
	Faraday Probe	Ion flux
	Emissive Probe	Plasma potential
	Retarding Potential Analyzer	Ion energies
Ex-situ	SEM/EDS/TEM/XPS/Laser Profilometry	Material and surface analysis

Figure 5.2: Diagnostic capabilities of the Pi facility.

5.2 The Large Plasma Device (LAPD)

The Large Plasma Device (LAPD) is a user facility located at the Basic Plasma Science Facility at UCLA and is supported by the US Department of Energy. With a high vacuum chamber that measures 20 meters in length and 1 meter in diameter, LAPD produces a pulsed plasma column that is approximately 60 centimeters in diameter and 18 meters long. This device is primarily used for studying plasma waves, turbulent transport physics, RF heating, and other fusion and astrophysical applications.

Recently, the LAPD was utilized to study the plasma-materials interactions (PMI) and arcing behavior of positively biased tungsten-based VCMs in a pulsed helium (He) plasma. This PMI experiment was part of an ARPA-E funded project called Advanced Materials for Plasma-Exposed Robust Electrodes, which aims to design and investigate high current density electrode materials for fusion-relevant applications. The goal of the LAPD PMI experiment was to expose custom tungsten VCMs and planar tungsten to a pulsed He plasma to observe ion sputtering, ablative erosion, and arcing behavior, using optical diagnostics and pre- and post-ex-situ materials analysis techniques such as electron microscopy and X-ray electron composition spectroscopy. To induce ion sputtering effects, the VCM and target samples were biased to several hundred volts (negative with respect to chamber ground).

The He plasma is primarily generated from a 38 cm diameter LaB6 cathode with molybdenum mesh anodes located 50 cm away, producing pulse lengths of 10-70 milliseconds, and a discharge of approximately 7.5 kA with an axial magnetic field of 0.1 Tesla [86] [7]. The main goal of the LAPD PMI experiment was to qualitatively observe the general erosion, sputtering, possible cathode spot formation and bipolar arcing behavior of a VCM in a high-fluence pulsed plasma environment. Arcing behavior is especially informative for a wide variety of applications including general vacuum discharges and cathode design. Electric field enhancement for non-planar surfaces can have a significant impact when studying secondary electron emission, field emission, thermionic emission, and the practical consideration of placing a VCM with a high voltage in a

plasma device [87] [88] [89].

The LAPD is equipped with a Data Acquisition System which is capable of storing digitized metadata and probe signals in HDF5 format for every shot. For the basic characterization of the LAPD plasma used for tungsten VCM PMI experiments, a triple probe was employed. This probe was used to measure the plasma in a straight line across the plasma column, located approximately 1 meter upstream from the target sample location. The entire 60 cm diameter plasma column was covered with 35 points spaced at 2 cm intervals, with 10 shots taken per point. Notably, no bias was applied to the target sample for these measurements.

To obtain T_e, n_e, and ϕ data, the triple probe was equipped with three channels. The first channel measured the ion-saturation current, I_{sat}, using a 60 V bias across a 106 Ω resistor. The second channel measured the difference between the applied positive bias and the floating probe voltage $V_+ - V_f$, which is proportional to the electron temperature, T_e. A third channel recorded the floating potential V_f with respect to the wall, using a 1/10 gain, while the fourth channel recorded the anode voltage, V_a, with respect to the wall using a 1/200 gain. The following expressions were used to calculate plasma parameters from the triple probe data channels:

$$T_e = \frac{k_B}{e} \frac{(V_+ - V_f)}{ln(2)} \tag{5.1}$$

$$n_e = \frac{I_{sat}}{eA_{probe}exp(-1/2)} \sqrt{\frac{m_i}{k_B T_e}}, \tag{5.2}$$

where k_B is Boltzmann's constant, M is the ion mass (helium) and A_{probe} is the probe tip which was $1.0mm^2$. The measurements show that the LAPD plasma at nominal operation for the VCM experiments described in the Results secrtion (4) has a slightly hollow density profile with maximum density of $n_e = 1.8 \times 10^{13} 1/cm^3$ at 20 cm radially from the column center. The electron temperature profile peaks between - 10 to + 10 cm from the column center at 7.5 eV, and the probe floats to ≈ -10 V with respect to chamber ground, which is a few volts above the plasma potential at the center of the column.

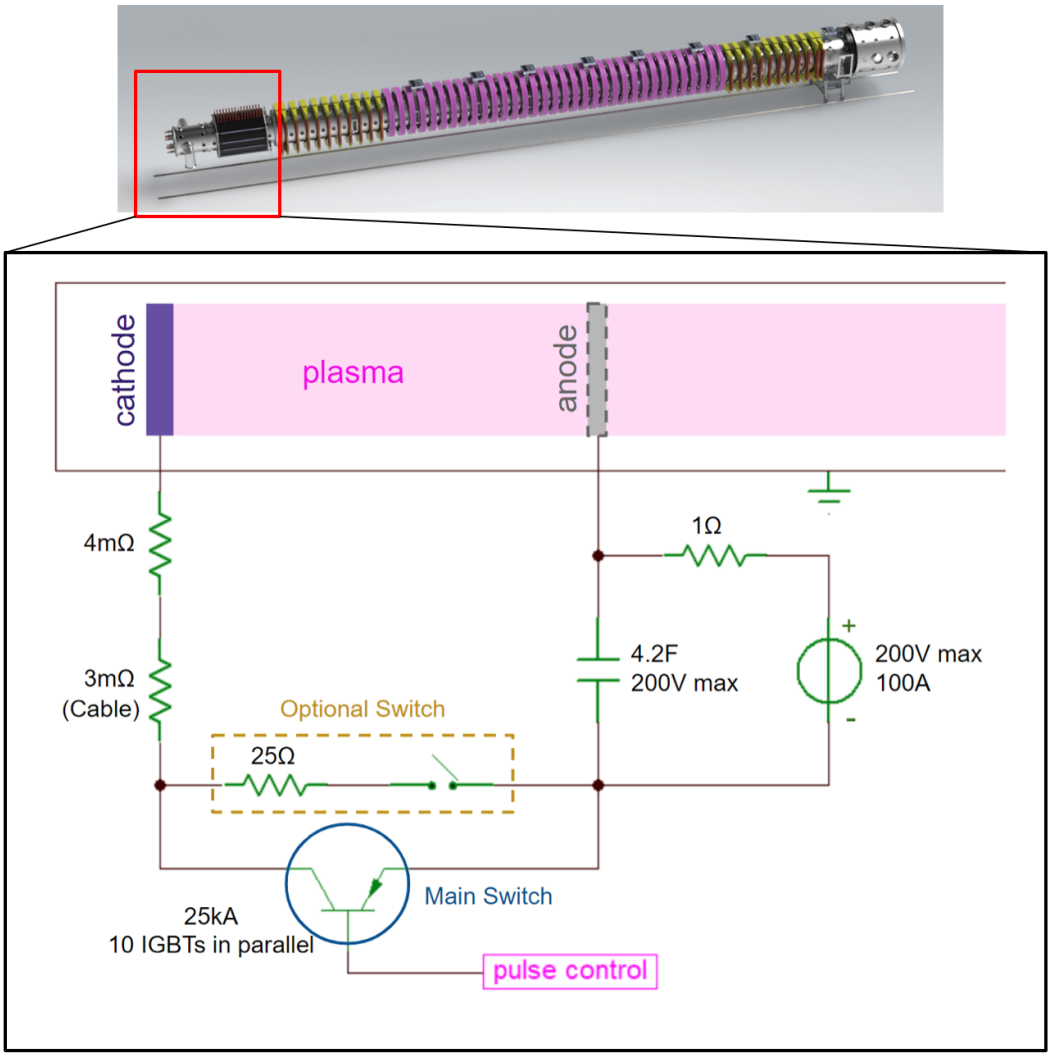

Figure 5.3: Photo and electrical schematic of the Large Plasma Device with a LaB6 cathode for plasma generation. The LaB6 cathode and Mo anode are located on the left side of the chamber in this diagram, with a distance of $\approx$ 50 cm between them. A capacitor bank of 4.2 F with 200 V maximum voltage is connected cathode to anode with a set of Insulated Gate Bipolar Transistor (IGBT) switches. [7]

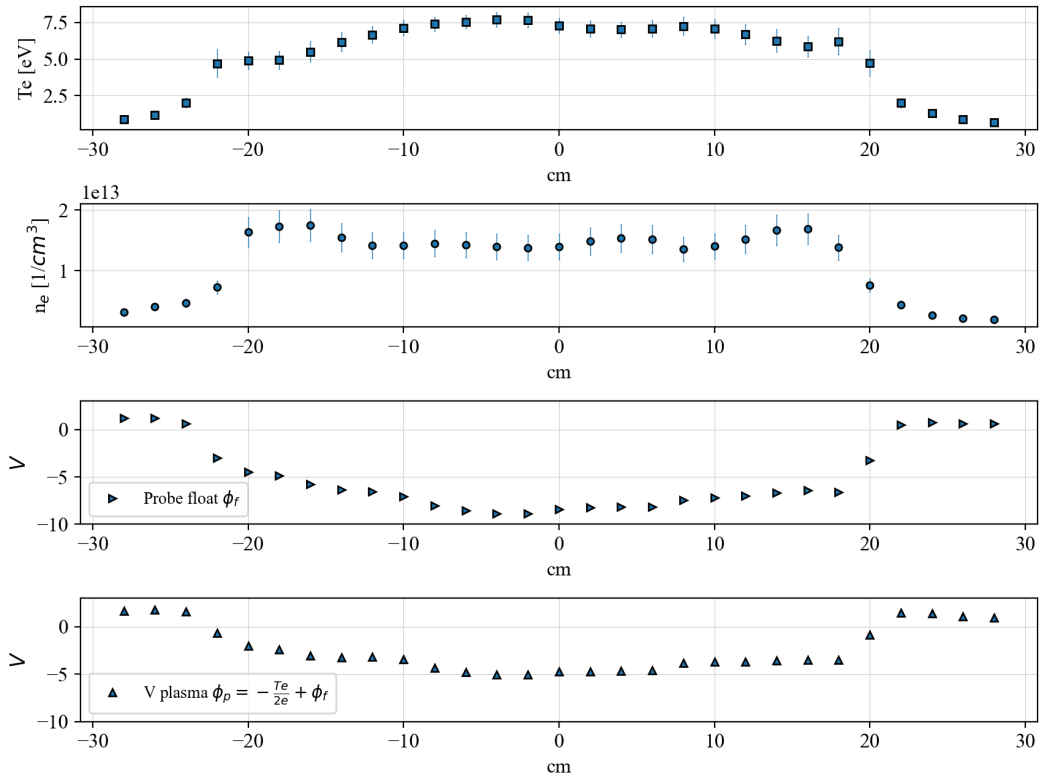

Figure 5.4: Triple probe profiles of LAPD plasma used for PMI experiments. The average electron density is $n_e = 1.7 \times 10^{13} 1/cm^3$ across the majority of the plasma column, and the electron temperature is ≈ 7.2 eV.

Processing of all LAPD data was achieved by first uploading data with the custom built open source *bapsflib* package in Python and the *bapsflib.lapd* module [90].

5.3 Materials Observation and Characterization Apparatus (MOChA)

The Materials Observation and Characterization Apparatus (MOChA) is a recently commissioned experimental device for testing plasma-material interactions rapidly and iteratively. The vacuum chamber is cylindrical with an 18 inch diameter and is 12 inches in height, with a lid which compresses into seal when under vacuum. A roughing pump backed by a turbo-molecular pump achieve vacuum levels down to $\approx 1e{-}6$ Torr in a 20 minute time frame. The plasma source is a custom designed and built tungsten filament hollow cathode encased by a cylindrical stainless steel body which is separately biased from the filament, and functions as a keeper for the initial cathode discharge. A cylindrical anode in either copper or graphite is used to complete a plasma discharge. MOChA is also configured with a sample bias up to 600 V which can be used as the anode for high current density target exposure experiments. The total plasma column is $\approx 15\,cm$ in length, and an external magnetic field is used to focus the plasma electrons to the sample target region. The magnetic field is established by a Helmholtz coil with a radius of 8 inches, and N = 150 turns for each coil. The field at the center of the plasma column has been characterized with a Gaussmeter and can achieve magnetic fields of up $> 150\,G$ for a current of 15 A, as shown in figure 5.7. At this magnetic field strength, the ion are not magnetized. Argon or xenon neutral gas can be flowed into the system interchangeably.

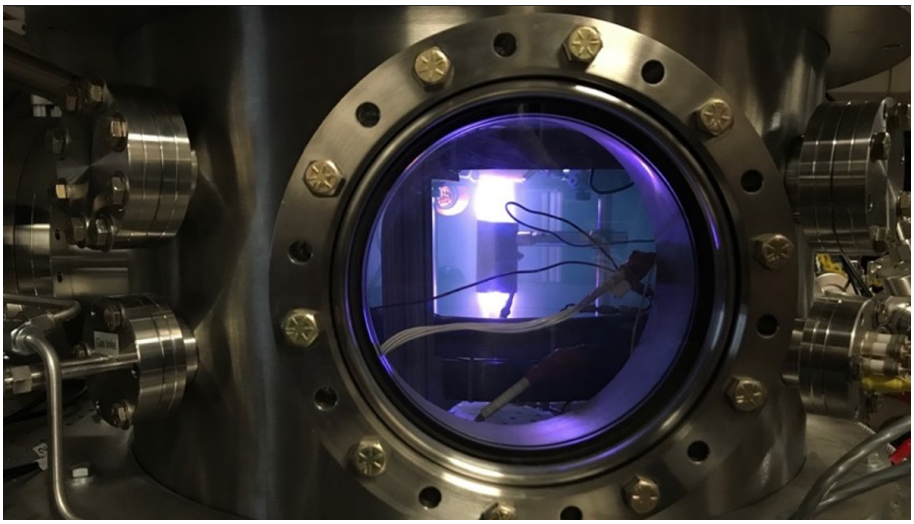

Figure 5.5: MOChA operating an argon plasma with a cylindrical copper anode and a filament hollow cathode.

TYPE	DIAGNOSTIC	MEASURED PARAMETERS
Non-intrusive	Quartz Crystal Microbalance (QCM)	Angularly-resolved differential sputtering rate, sputtering yield
	Optical Emission Spectroscopy (OES)	$n_e, T_e, n_n, n_{sputterants}$ Material side view capability
	Witness Plates	Deposited sputterant composition
	External CCD camera	Qualitative surface image monitoring
Intrusive	2-axis Langmuir Probe	n_e, T_e, ϕ_p
	2-axis Emissive Probe	Plasma potential (ϕ_p)
Ex-situ	SEM/EDS/TEM/XPS/Laser Profilometry, SEE Yield	Comprehensive surface/subsurface analyses and mapping

Figure 5.6: Diagnostic capabilities of the MOChA facility.

The intrusive and non-intrusive diagnostic capabilities of MOChA are listed in Figure 5.6. These include 2D staged Langmuir and emissive probes, optical emission spectroscopy with a focus of < 1 mm and a quartz crystal microbalance for measuring in-situ sputter yield. The target sample is placed in a custom built boron nitride sample holder and can be biased with respect to

ground and electrically isolated from the plasma system. In addition to the plasma and material diagnostics in MOChA, a CCD camera sits outside the main view-port to monitor the operation of PMI experiments and the near surface material region. Thermocouples are also installed to measure and record the temperatures of various system components, including the target samples. The magnetic field strength as a function of Helmoltz coil current and chamber location were measured with a Gaussmeter and are shown in figure 5.7.

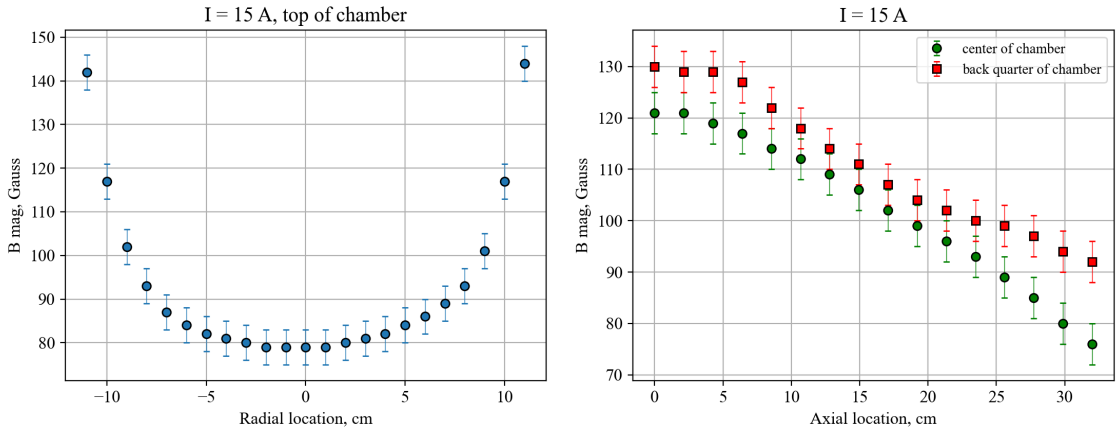

Figure 5.7: Magnetic field characterization of MOChA at different locations in the chamber with a current through the Helmholtz coils of 15 A. The coils can also be run individually with different currents to achieve magnetic cusping and focusing.

Images of MOChA, complete with a diagnostic setup is sown in figure 5.8.

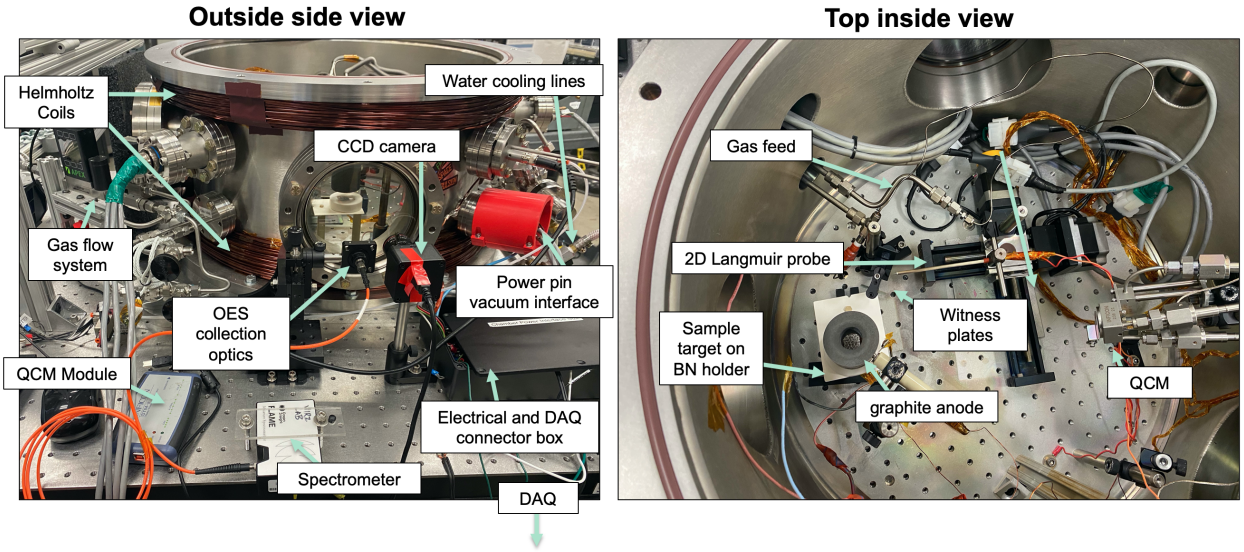

Figure 5.8: (Left) External side view of the MOChA chamber and (right) interior view of the chamber from above. The filament hollow cathode is not shown in these images.

5.3.1 Filament hollow cathode and cylindrical anode

A custom designed and manufactured filament hollow cathode is used as a plasma source for MOChA. Similar concepts can be found in previous literature and experimental setups such as in [91]. A stainless steel cylindrical enclosure houses a W filament which is mounted through a ceramic bore post. A graphite cap with a < 1 mm diameter chamfered orifice is then attached to the front of the cathode body to allow for controlled electron, gas and plasma flow out the center of the cathode. Swagelok® fittings are used at the back of the cathode body to flow gas into the cathode. This cathode was tested with both argon and xenon flow rates of 1-4 sccm. The stainless body of the cathode can be positively biased with respect to the tungsten filament to function as a keeper [14] and to ensure a plasma can be ignited in the cathode. Once a plasma is established, the keeper power supply is generally turned off and the discharge remains sustained.

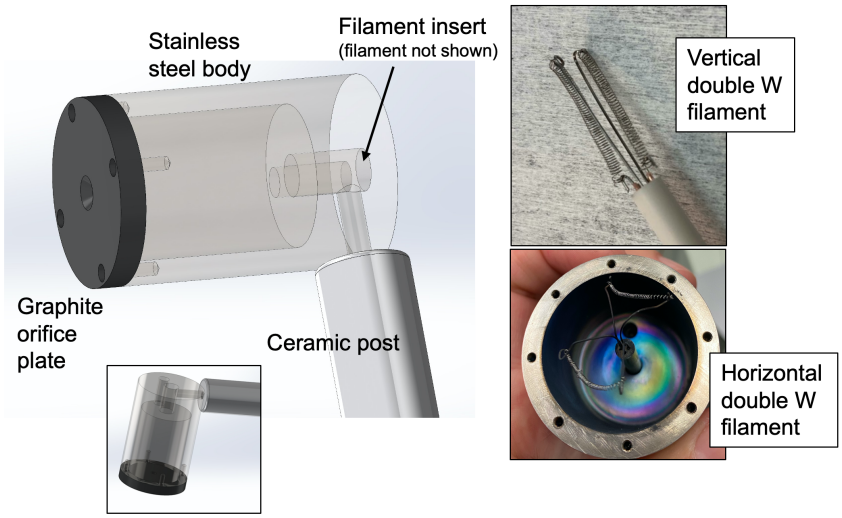

Figure 5.9: (Left) CADs of the stainless steel body with graphite orifice plate of the filament hollow cathode. The diameter of the orifice plate and body are 2.54 cm, and the length of the body is 4.45 cm. (Right) A double W filament in both a vertical (length wise) configuration and horizontal (parallel to the orifice plate plane) inserted in a ceramic bore post are the electron source for MOChA. This design was completed by Richard Wirz, Stephen Samples, and Angelica Ottaviano (UCLA).

Two separate filaments are used in the cathode so that if one fails, the backup filament can be powered without breaking vacuum during an experiment. The filaments are typically run at 60 W power with a current of 2.5 A. Using a blackbody radiation approximation, the filament temperature can be calculated and is shown in Figure 5.10. The Stefan-Boltzmann Law instead is used to calculate the emitted current from the W filament for material different work functions, including that of W which is 4.45 eV. The typical operating parameters for the filament are 2.0 - 2.5 A at 30 V. The filament has a radius of 0.064 mm and a length of 4-5 cm

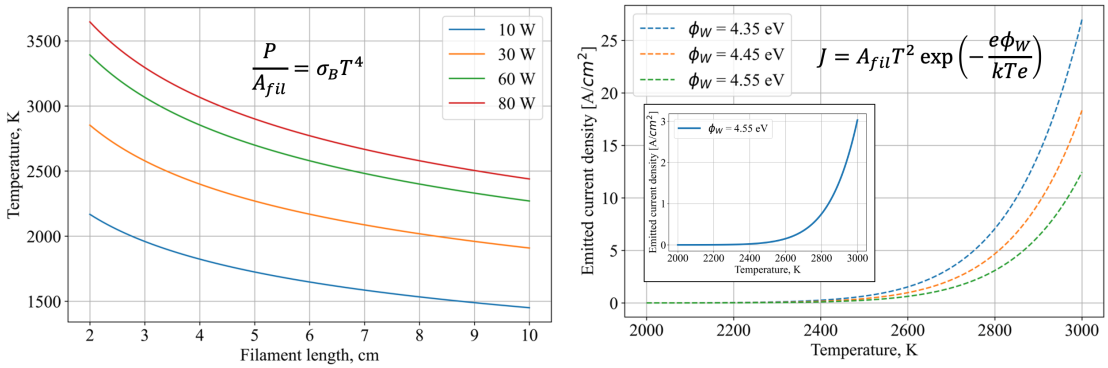

Figure 5.10: (Left) Schematic of argon neutral gas flow through the filament hollow cathode, and (right) the orifice exit pressure for different orifice diameters for varying neutral flow rates, and assuming a temperature of 400 K.

The neutral pressures upstream (P_1 and downstream P_1 of the stainless cathode body cylinder can be found using modified Poiseuille flow for compressible flow. The flow rate (Q) is defined as:

$$Q = \frac{\pi a^4}{16 \nu l} \frac{\left(P_1^2 - P_2^2\right)}{T_r} \tag{5.3}$$

$$P_1 = \left(P_2^2 + \frac{0.78 Q \nu T_r l}{d}\right)^{1/2} \tag{5.4}$$

where ν is the viscoty of Ar, and a, l are respectively the cylinder radiu and lengths, d is the orifice diameter and $T_r = T/290K$ [92, 93]). In combination with a free-molecular flow approach for neutral density between the orifice exit and the ambient chamber pressure, it is found that there is a 2-3 order of magnitude drop in neutral density at the orifice exist with when using flow rates of 1-4 sccm of argon.

The filament hollow cathode is operated with a cylindrical anode. A copper anode and graphite anode were tested for device performance. The choice of Cu or graphite anode is made based on the nature of the PMI experiment: if graphite or Cu materials are being examined, a dissimilar anode is used to avoid witness plate and material contamination from anode evaporation, heating or sputtering.

5.3.2 Langmuir probe data of MOChA plasma and example experiment

The plasma generated in MOChA was characterized using a Langmuir probe for different operational set-points. These include varying current drawn to the anode, magnetic field strength, and neutral gas flow rate through the filament hollow cathode. Figure 5.14 shows an example of a single point Langmuir probe analysis used to retrieve T_e and n_e. 50 Hz measurements per set point are taken with 20,000 points per acquisition using a Kepco power in combination with a Agilent signal generator, and a 110 Ω resistor across the probe. MOChA is equipped with two Langmuir probes to analyze the behavior of plasma near structured materials before and after plasma infusion, however for the purpose of these measurements (nominal plasma characterization), only one probe was used near the target surface. The target in these experiments was a planar, grounded stainless steel plate. The data was acquired using an oscilloscope and then analyzed in Python. Each voltage ramp and probe response I-V trace was averaged and smoothed using a spline function. To find the plasma potential, the intersection of line fits to the log of the I-V ion saturation and electron saturation regions was used.

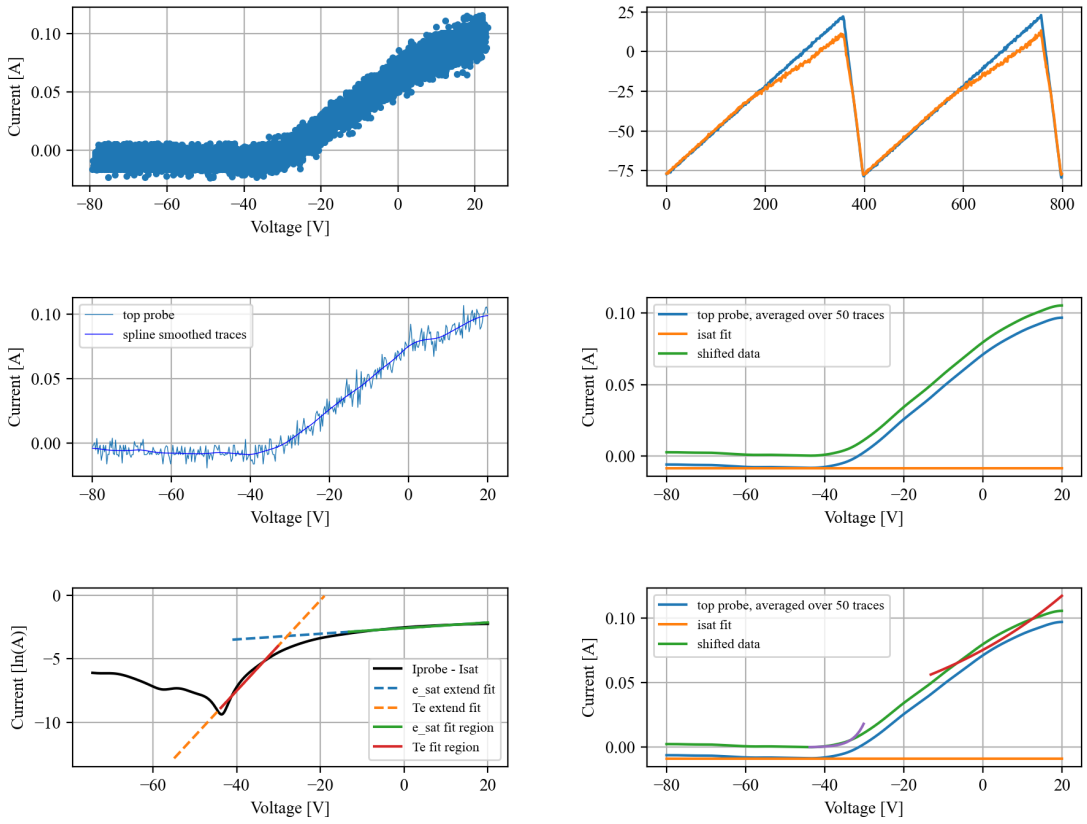

Figure 5.11: Step by step Langmuir analysis procedure starting from raw oscilloscope data.

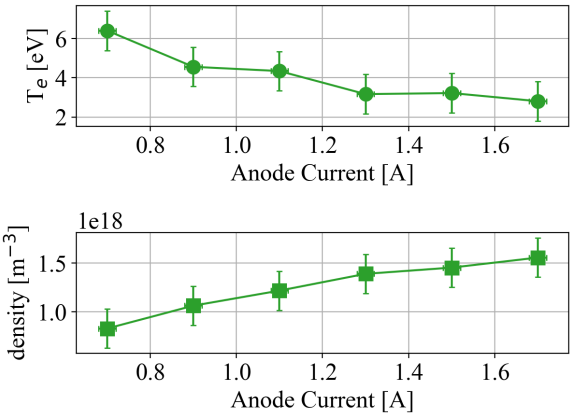

Figure 5.12: Electron temperature and density as a function of anode current.

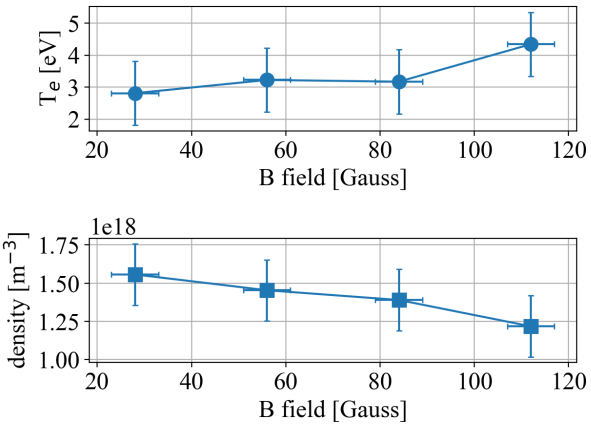

Figure 5.13: Electron temperature and density as a function varying magnetic field strength for symmetric Helmholtz coil configuration.

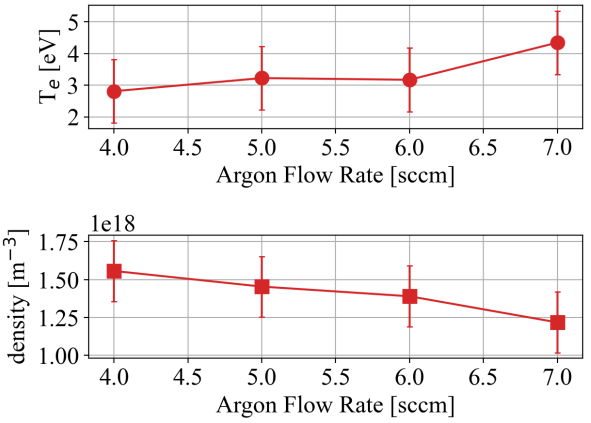

Figure 5.14: Electron temperature and density as a function of neutral argon flow rate.

The plasma column at the sample interface is equal to the anode inner diameter. For these experiments, the anode has an inner diameter of 2 cm. With this setup, a demonstration of ion sheath visualization on the stainless steel target plate was recorded. The stainless steel target was biased up to - 300 V from floating. An external CCD camera was used to acquired a video of the sample during biasing, and stills are shown in figure 5.15. The Debye length, λ_D of the MOChA plasma is $\approx 60\mu m$. The sequence of images show (right) a floating surface-plasma interface, where the Debye sheath is on the order of $3\lambda_D$ and isn't visible in the image. As a bias is applied and

negatively increased on the sample surface, the sheath grows to $\approx 1500\mu m$, as approximated by Child-Langmuir, and a dark region above the target plate becomes visible. As the sheath further is increased with a - 300 V bias, a blue glow is detected, most likely reflecting on the stainless plate. The blue glow could be due to excited argon ions which are present in the ion sheath in the absence of electrons, which glow in the blue part of the visible spectrum. The measured current to the sample is 60 - 100 mA, which will be used for future ion fluence calculations in PMI experiments.

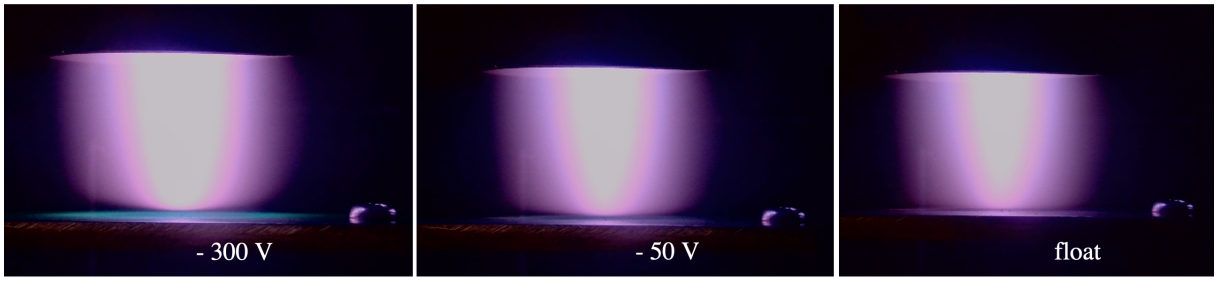

Figure 5.15: A stainless steel plate biased down to - 300 V was used a sample target for MOChA experimental characterization. Visualization of the Child-Langmuir sheath is shown for the -50 V and - 300 V cases, with a characteristic blue glow reflecting on the stainless steel plate. This glow is likely due to the excited argon ions in the sheath.

5.4 In-situ microscopy of plasma erosion using Long Distance Microscopy (LDM)

A novel method for the in-situ visualization and profilometry of a plasma-facing surface is demonstrated using a long-distance microscope. The technique provides valuable in-situ monitoring of the microscopic temporal and morphological evolution of a material surface subject to plasma-surface interactions, such as ion-induced sputter erosion. Focus variation of image stacks enables height surface profilometry, which allows a depth of field beyond the limits associated with high magnification. As a demonstration of this capability, the erosion of a volumetrically-featured aluminum foam is quantified during ion-bombardment in a low-temperature argon plasma where electron temperature is 7 eV and the plasma is biased relative to the target surface such that ions impinge at approximately 300 eV. Three-dimensional height maps are reconstructed from the im-

ages captured with a long-distance microscope with an x-y resolution of 3 x 3 microns, and a focus variation resolution based on the motor step-size of 20 microns. The time-resolved height maps show a total surface recession of 730 microns and significant ligament thinning over the course of 330 minutes of plasma exposure. This technique can be used for developing plasma-facing components for a wide range of plasma devices for applications including propulsion, manufacturing, hypersonics, and fusion.

Visualizing and quantifying the morphological evolution of a surface undergoing plasma erosion is critical for understanding and developing plasma-robust materials that can withstand sputter erosion and reduce plasma contamination. In addition, the surface morphology of a plasma-facing material dictates the structure of the electrostatic sheath potential at the plasma-material interface, which can influence the trajectories and energies with which ions impact the material surface [94, 95, 96]. Steady-state and pulsed plasma discharges can also cause blistering, bubbling, and cracking of material surfaces [97]. Conventionally, material surface diagnostics for PMI effects are performed ex-situ using devices such as optical microscopes, Scanning Electron Microscopes (SEMs), and Transmission Electron Microscopes (TEMs) for imaging the surface; weight-loss measurements to surface recession; and X-Ray Photoelectron Spectroscopy (XPS) and Energy-dispersive X-ray Spectroscopy (EDS) for chemical composition analysis before and after plasma exposure. Although these ex-situ diagnostics provide some understanding of how plasmas affect material surfaces, it is also important to capture real-time surface changes during plasma exposure for a more comprehensive and temporal understanding of PMI processes.

Previous examples of real-time and in-situ monitoring of material surface changes during plasma exposure include in-situ laser holography for International Thermonuclear Experimental Reactor (ITER) plasma facing components [22] , and imaging of tungsten plate surface modification under ITER-like heat loads [98, 99, 100]. Although the method described in [22] is in-situ and real-time, it is applied to a pulsed electron beam and simulates high ITER-like heat loads. The technique is not suitable for visualizing the evolution of a surface undergoing continuous ion-bombardment in lower temperature and lower instantaneous power environments, such as those

found in magnetic confinement fusion divertors, or in surfaces and electrodes of electric propulsion thrusters.

For the experiment described in this work, the LDM was placed on a linear motorized stage which was aligned with the target sample at an initial distance of 35 cm. The large WD was chosen as to minimize thermal damage to the LDM. By moving the LDM closer to the sample with the motorized stage, the focused object plane moves through the depth of the sample surface, and an image is acquired for each position. In this way, the depth of field of the LDM is extended to image the structure of the target sample parallel to the plasma column axis. One sequence of images taken through 2 - 4 mm of the sample depth is referred to as an image stack. Each image in a stack are separated by a step size of $20\ \mu m$ relative to the preceding and following images in the stack. In image post-processing, custom algorithms detect in-focus pixels for each image in an image stack. These stacks are then recompiled into a composite image, which is a reconstruction consisting of all of the most in-focus pixels of the same scene. The LDM, in combination with a camera and a linear motorized stage, is therefore capable of producing focused micrographs with a large depth of field. In addition, because the focal length and motor step size are known for each image, a height map can be generated to correspond with each composite image. During plasma exposure, this process is repeated several times at constant time intervals, such that an erosion video and time-resolved set of height maps showing surface recession can be computed. The focus-variation method and the algorithms used to generate these data are explained in the next section.

The LDM system is positioned in the Pi chamber off-axis with respect to the plasma column and consists of a Complementary Metal–Oxide–Semiconductor (CMOS) camera, the microscope, an optical shutter, a motor-driven stepper stage, and several Light Emitting Diode (LED) sources. The sample could be rotated to capture other views of the surface. These components are electrically powered via a vacuum feedthrough of the vacuum chamber and are connected to a computer station and power supplies for manual and automated control. Controls for the LDM are implemented using a LabVIEW virtual instrument (VI). Figure 5.16 (a) shows the LDM placed on a motorized stage with its optical axis aligned to the center of the sample surface. The camera is

mounted to the back of the LDM. 5.16 (b) shows the LDM placement in the Pi chamber. The sample is rotated so that it is normal to the optical axis of the LDM and is at 35o with respect to the axis of the plasma, indicated by the location of the focusing magnet coils. Motorized optical shutters are placed in front of the LDM and in front of each LED, which are remotely operated to prevent coating during potential material sputtering from plasma exposure of the target. Coating of the LDM lens or the LED would cause gradual darkening of the acquired sample surface images over time, deteriorating the quality of the data.

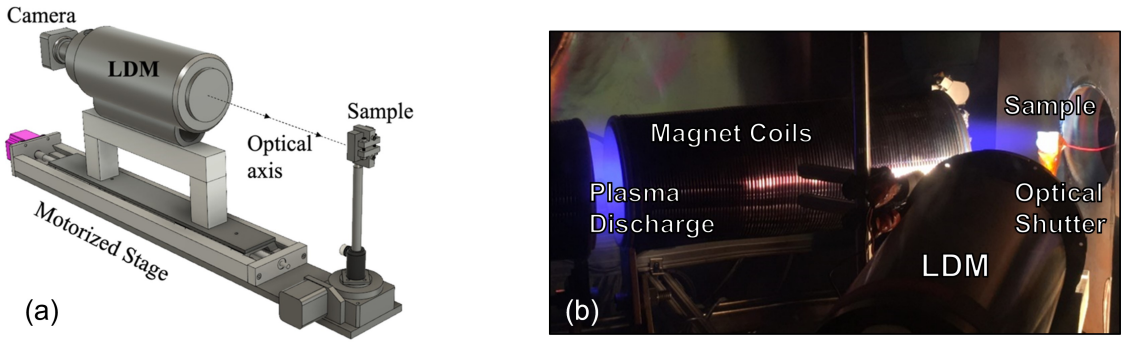

Figure 5.16: (a) The Long Distance Microscopy (LDM) system including the camera, motorized stage and sample target. (b) The LDM system placement in the Pi chamber, aligned to the center of the sample surface and with an optical shutter in front of the final lens of the LDM. An argon plasma discharge (purple) is focused onto the sample by a series of magnet coils.

The sample chosen for this experiment was an aluminum foam provided and manufactured by Duocel [23]. Aluminum was chosen because of its higher sputter yield of 1.1 atoms/ion at 300 eV [101] with respect to conventional plasma-facing materials such as tungsten or carbon. Surface recession and erosion of aluminum should be more pronounced than tungsten or carbon for a lower ion fluence, making the target suitable for benchmarking a diagnostic for visualizing and measuring erosion. The foam geometry was chosen because recent studies have shown this to be a promising candidate material for plasma-facing surfaces due to its inter-cavity trapping property, low secondary electron emission and large surface area for heat dissipation [102]. The aluminum foam has a pores per inch parameter (PPI) of 40 with an average pore size of *approx*

250 μm.

The argon plasma is generated by dividing the argon mass flow between the cathode and the anode gas injectors to create a stable plasma across a wide range of operating conditions. The discharge current was set at 45 A and the cathode potential was biased to –40 V relative to ground. The target was subsequently negatively biased to -300 V so that ions that are accelerated through the electrostatic sheath. The temperature of the sample was continuously monitored with a thermocouple to not exceed 300o C to limit excessive thermal drifting of the sample, which would cause the surface area of interest to move out of the camera frame. The sample was exposed for a total of 5.5 hours, and at 15-minute intervals the bias on the sample was turned off so that LDM image stacks could be acquired. When the sample is unbiased, the LED and LDM shutters can be opened since there are no sputterants to be deposited on the surface of the optical components. The LDM takes approximately 5 minutes to acquire a stack of 150 images, each at a 20 μm step size. In total, the LDM should therefore acquire images at 3 mm depth into the sample surface during each scan. A total of 75 image stacks were acquired.

5.4.1 Shape-from-focus method and focus-variation algorithm

Shape-from-focus is a general shape extraction method introduced by Nayar et al. [103, 104, 105, 106] [28]. Corresponding algorithms are known as focus measure operators and are used to detect the most in-focus pixels for a series of images of the same object with varying object plane. Assuming the distance is known between each focus level or individual image, an in-focus pixel is assigned the distance between its focus level and the first or last focus level. If the pixel size of the camera is known, then a scaled height map can be generated from a series of images. A sequence of algorithms has been compiled by UCLA Plasma and Space Propulsion Laboratory (PSPL) to process a series of images acquired by the LDM of a foam surface during plasma exposure to generate composite images and height maps of the evolving surface.

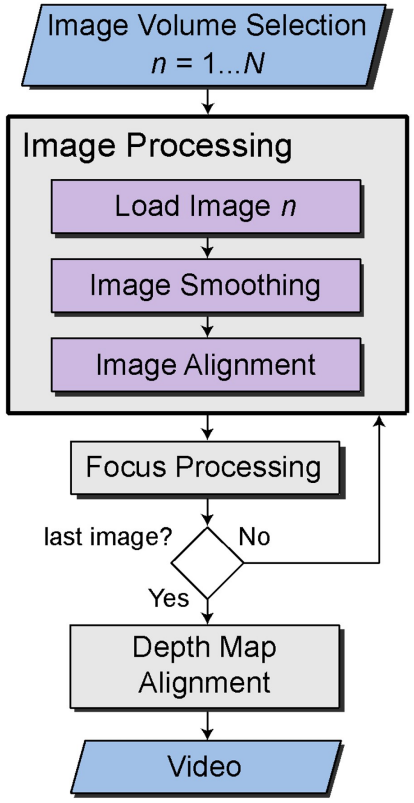

Figure 5.17: Schematic of the algorithm sequence developed by UCLA for generating composite images and height maps of LDM acquired image series.

Figure 5.17 shows a schematic of the entire algorithm sequence applied to the LDM-acquired images. Once a series of images has been captured by the LabVIEW VI, each image stack undergoes a processing sequence that removes noise and aligns each image in the stack to the first image. The noise is removed by applying two filters: a 2-D Gaussian filter and a median kernel filter. The Gaussian filter is used to smooth saturation regions where the intensity is either too high or too low, while the median kernel filter removes any speckle noise by taking the median of 3×3 neighboring pixel regions. An example of speckle noise and its removal of an image of a pore of the aluminum foam is shown in Figure 5.18.

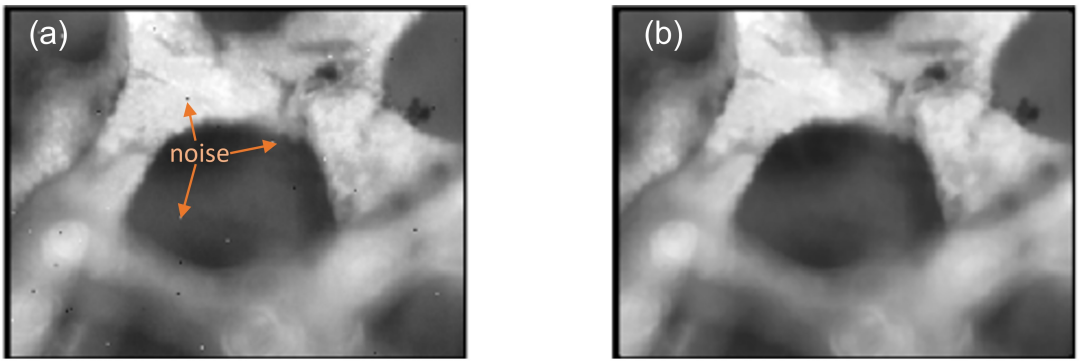

Figure 5.18: Example of noise removal by median kernel of a foam image by showing image (a) with speckle noise present due to camera sensor failures and (b) with the speckle noise removed.

After removing noise from the original series of images, it is important to make sure the images are all aligned to their optical center. The optical center is determined by the central pixel of the first image in the stack. Because the sample reaches temperatures up to 350^{o}C, significant thermal drift occurs during image acquisition. In addition, because the working distance is so large when using an LDM, micron-precision alignment with the sample is challenging. As the LDM moves closer or further from the sample, there might be slight translation of the images from the optical center. The alignment is performed by applying a phase correlation method algorithm. Phase correlation estimates the translation between two images by computing a Phase-Only Correlation (POC) function, which is the normalized cross-spectrum of two images in Fourier space [107]. Figure 5.19 shows the sequence for aligning two images. The phase correlation is based on the Fourier Shift Theorem, which can be used to find rotation and translation in the polar domain. The rotation of a two-dimensional signal in Cartesian space corresponds to the translation of angles in polar coordinates, therefore Log-Polar mapping results in radial steps which are taken logarithmically [108, 30]. The log polar transform is rotation and scale invariant. The Log-Polar Transformation is used to register images which are transformed by rotation and translation.

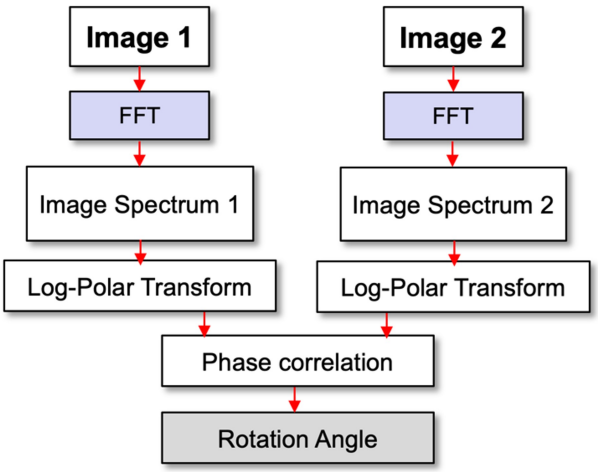

Figure 5.19: Sequence of the phase correlation method used to align two images that have been translated or rotated

After the images have been aligned, the focus-variation algorithms are applied to the image stacks to produce a single composite image with every pixel in-focus and to measure the relative depth of each pixel in reference to a fixed axial position. The focus-variation algorithm was taken from Ref [109] where further details are documented. In-focus pixels for each image are compiled into a single composite image for each stack. When a series of composite images has been produced, they are then combined into a video where each frame is a composite image. Another alignment is performed on each frame of the video. The result of the set of algorithms is a video of composite images representing the surface erosion over time due to plasma exposure, and the corresponding topological evolution of each composite image [23]. Various stages of these algorithms are shown in Figure 5.20 for an ex-situ benchtop experiment with a copper foam with a motor step size of 60 μm.

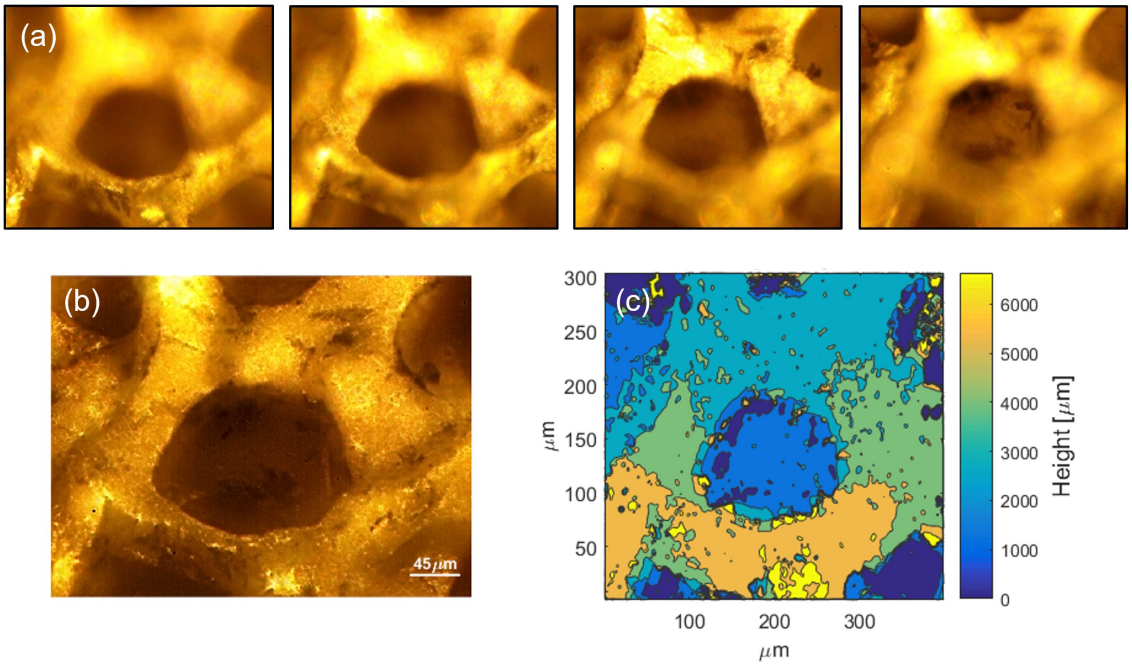

Figure 5.20: (a) Examples of images at different focus levels for a copper foam sample in a bench-top experiment. For this characterization of the focus variation technique, the LDM was moved using 60 μm steps between each image; however, height resolution can be improved with smaller step sizes. (b) The composite image generated from 150 images in a single stack and (c) the height map generated from the composite image.

5.4.2 LDM generated foam erosion images

An aluminum foam erosion sequence with corresponding height maps produced by composite image stacks was generated to demonstrate the capability of using an LDM with a camera and a motorized stage as an in-situ plasma-surface interaction diagnostic system. Select images from the sequence are shown in Figure 5.21 at different stages of the surface erosion and ion fluence: at the start of the ion-bombardment, midway through the ion-bombardment, and at the end of the 330-minute experiment. The three frames show aluminum foam ligaments thinning as the ion-sputtering erodes the surface features.

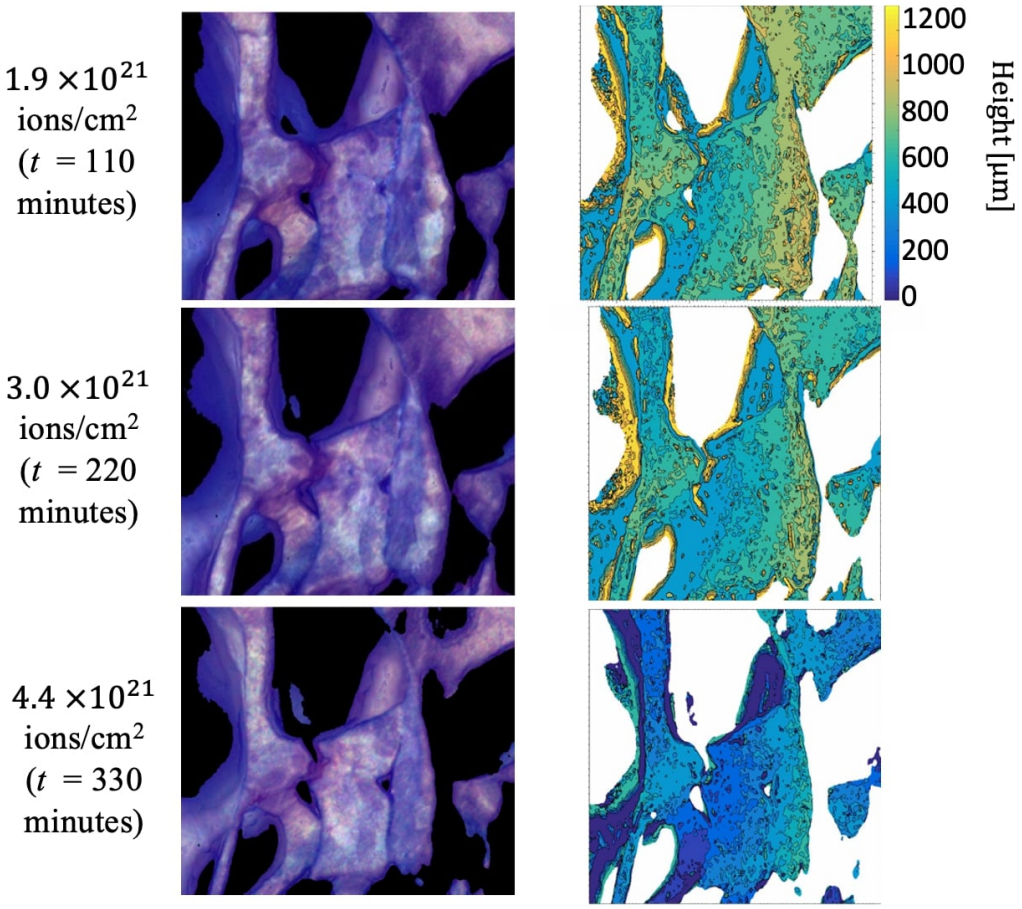

Figure 5.21: Three images of the aluminum foam erosion sequence generated during the experiment outlined in Sec. IV represent three stages of foam erosion. Each frame is $600 \times 600\ \mu m$ in size. A side-by-side view of each composite image in the sequence is compared to a corresponding height map to quantitatively assess the surface erosion over time.

The sequence generated by the composite images reveals the morphological evolution of the aluminum foam surface with a time interval of 15 minutes. The background region, which remains out of focus for the entire range of the LDM, was removed and set to black or white space, as shown in Figure 5.21. By removing the unfocused background, it is easier to distinguish the surface of the foam under observation and the LDM system is able to perform 3-D surface reconstructions. Aluminum ligament thinning and pore expansion is visualized throughout the experiment. The

height maps reveal an average total of $\approx 730 \pm 20\ \mu m$ of aluminum eroded from the observed foam surface at the experimental conditions of - 300 V bias and 330 minutes (5.5 hours) of plasma runtime. The fluence, *Gamma*, is defined as the total number of ions which are incident on the target per unit area and can be found via the time-integration of the ion flux $F_i(t)$.

$$\Gamma = \int_{t_0}^{t_1} F_i(t)dt \tag{5.5}$$

The ion flux was measured using a Faraday probe is reported in Table I. It can therefore be calculated that a total fluence of $\approx 4.4\times10^{21}$ ions/cm^2 was delivered to the sample surface by the end of the experiment. Another important result revealed via LDM imaging and profilometry is that the surface morphology of the aluminum foam over the course of the experiment remained structurally intact and could still be considered a foam during and after erosion. Foams are volumetrically structured materials and a particularly interesting property of such surfaces is that they maintain their structure throughout erosion rather than evolve into a planar surface [110]. The LDM system provides insight into how the structure evolves. It is important to have time-resolved erosion images to determine transient surface breakage events such as flaking of large fragments detaching from the target sample.

The LDM diagnostic coupled with focus-variation algorithms is a novel application of profilometry for producing in-situ and time-resolved imaging of plasma-facing surfaces. In this work, a demonstrative experiment successfully produced composite erosion and height map sequences of a biased aluminum foam subjected to a low-temperature argon plasma. Because of the relatively high sputter yield of aluminum with respect to conventional plasma-facing materials, a morphological evolution of the surface was observed in an exposure time of 330 minutes. Time-resolved height maps also quantify surface recession throughout the plasma exposure. The depth resolution of the height maps is based on the minimum motor step size (20 μm herein). However, with smaller step size the true depth resolution can be as high as the diffraction limit of the lensing system.

The LDM system as a plasma-surface diagnostic is critical for plasma-material interaction re-

search. Current methods commonly focus on pre- and post- surface composition and imaging analysis but lack the ability to reveal time-resolved behavior of the surface during plasma exposure. It is especially advantageous to capture crucial transient erosion events such as flaking of mm sized material pieces that may occur in featured surfaces, such as foams, velvets or fuzzes. Topological height maps can help determine the erosion rate of different features within a single surface in each dimension; the 2D edges of the features and the axial dimension (recession) aligned to the LDM stage. In-situ visualization and LDM enabled surface reconstruction is particularly applicable to improving the performance and lifetime of limiters and divertors of magnetic confinement fusion devices as well as electric propulsion devices. The low-temperature plasma conditions of these devices and components are suitable for operating the required setup for the LDM diagnostic system.

Future considerations and improvements to the LDM plasma-surface diagnostic include establishing techniques for accurately calibrating the height maps. Current results produce relative recession rates and total surface erosion. Ex-situ calibrations techniques are being developed to enable calculation of absolute surface recession from LDM data. In addition, the current resolution of the LDM (3 μm) could be improved by implementing super-resolution microscopy methods to the LDM optics, such as structured illumination microscopy [33]. Lastly, a future effort of the LDM diagnostic system is to modify the image processing algorithms to render the technique suitable for reconstructing surfaces which are not at a normal angle to the optical axis of the LDM. This added capability would provide a significant improvement to the proposed diagnostic by reducing restrictions on experimental setup requirements, as well as providing insight into in-situ surface modifications occurring at multiple regions on the target surface

5.5 Demo experiment of plasma infusion through an aluminum foam surface as a function of sample bias

A demo experiment was performed in the Pi facility for observing plasma-infusion through an aluminum foam surface. The foam used as a sample target was Duocel aluminum foam with 20 PPI with a 1cm thickness and surface area of 10 cm $\times$ 10 cm. The pore diameter for this foam is $720 \pm 120\,\mu m$ The xenon plasma column center-line density in this experiment is $n_e = 8 \times 10^{17}\,m^{-3}$ and the electron temperature is $T_e = 5\,eV$. The expected Debye length is $\lambda_D = 18.5\,\mu m$. The Al foam was placed at the magnetic cusp of the Pi plasma column with no backplate. Langmuir probes were used to monitor the bulk plasma properties, and optical emission spectroscopy was used to measure the Xe signature and relative density infront, in between and behind the foam, with an edge-on view of the plasma column. The specific locations for optical emission collection are specified in Figure 5.23. A camera outside of the vacuum chamber captured images of the plasma-foam target region. The foam target was initially floated (-35 V) and was biased down to -150 V over the course of 5 minutes. Based on the Child-Langmuir law for a negative electrode, the sheath thickness at -100 V is expected to be $\approx 280\,\mu m$.

With no sample bias, a plasma is observed behind the foam (downstream of the hollow cathode), and as the bias in increased negatively, the foam is expected to become plasma-facing as the sheath thickness increases from much smaller than the pore size to on the order of pore size. Other factors such as exponential drop in plasma density as a function of pore depth and neutral pressure buildup are expected to contribute to a rapid transition from a plasma infused to a plasma facing regime with sample bias. Optical emission spectroscopy measurements at several locations infront, behind, and in the middle of the sample confirm that the Xe plasma drops off in density after the first couple of pore layers of the foam [111].

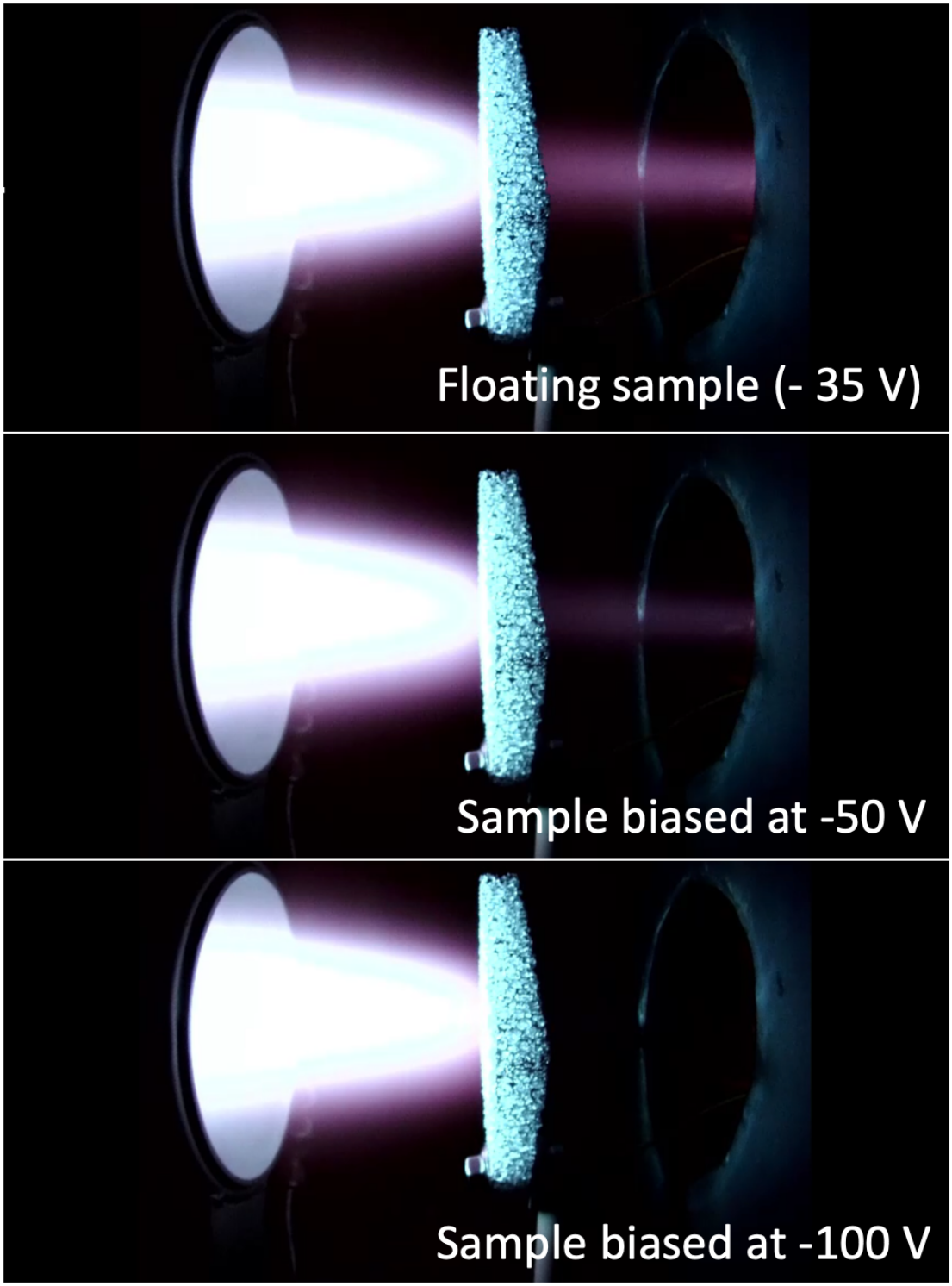

Figure 5.22: Xe plasma magnetically focused onto a 20 PPI foam with no backplate for a floating foam condition, a -50 V foam bias, and -100 V bias.

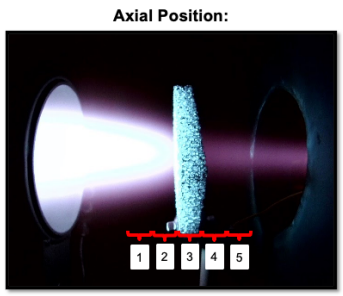

Setpoint	Discharge	Chamber and Anode Magnets	Sample Bias
A	ON	OFF	FLOAT
B	ON	ON	FLOAT
C	ON	ON	-50 V
D	ON	ON	-100 V

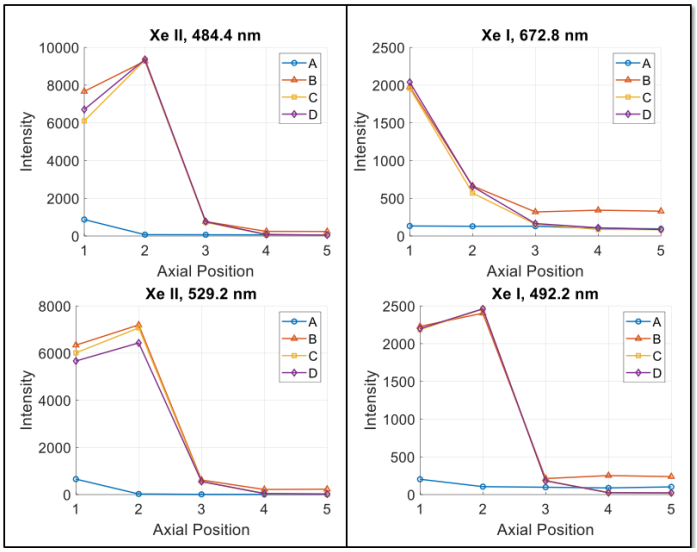

Figure 5.23: Optical emission spectroscopic measurements of Xe intensities for 5 different locations across the foam sample region at 4 different plasma and sample bias setpoints. By the location 3 into the sample, Xe is at $>$ 10% of its out-of-sample intensity. The OES setup is similar to that described in [8].

This experiment was an important validation of plasma infusion in a floating foam sample with low PPI and high transparency with no backplate. The observed results set up the groundwork for future quantitative experiments and simulations to understand how plasma and materials properties affect the behavior of plasma, excited neutrals and neutral gas buildup in a complex material structure.

5.6 Sputtering of Layered Dissimilar Foams

An experiment was conducted to investigate plasma-foam and inter-foam transport between different pore layers.

This experiment was carried out first in the Pi facility at UCLA using a partially ionized argon plasma column, and later repeated with MOChA. The plasma has magnetized electrons and unmagnetized ions, and is magnetically cusped approximately to the center of the sample target. The plasma density along the center-line is measured with a Langmuir probe to be on the order

of $n_e = 5 \times 10^{17}\, m^{-3}$, with an electron temperature $T_e = 3\,\text{eV}$. In this experiment, a target sample was biased to - 300 V below ground to accelerate argon ions to the surface and through a Child-Langmuir ion sheath, causing ion induced sputtering at ≈280 eV energies. The target sample was a double layer foam with a solid plate back. One foam was a 20 PPI aluminum foam with 3% volume fill density and 1 cm thick, and was provided by ERG Aerospace Duocel. The second foam was a 40 PPI copper foam with 5% volume fill density and 1 cm thick, also provided by Duocel. The backplate was a 1 mm thick nickel plate. Each of the components of the stacked foam with backplate sample were 5 cm×5 cm in surface area. Figure 5.24 (a) shows the Al and Cu samples with the Ni plate after plasma exposure, while Figure 5.24 (b) shows the stacked sample during plasma exposure. The Al foam is directly facing the plasma, while Cu is placed between the Al foam and the Ni plate, and the Ni plate is at the back of the sample system. The two foams were held together with the Ni backplate by compression custom made sample holder which had minimal plasma facing parts made of alumina ceramic. Mica ceramic sheets were used around the edges of the foam samples to avoid plasma coming into contact with the sides of the target.

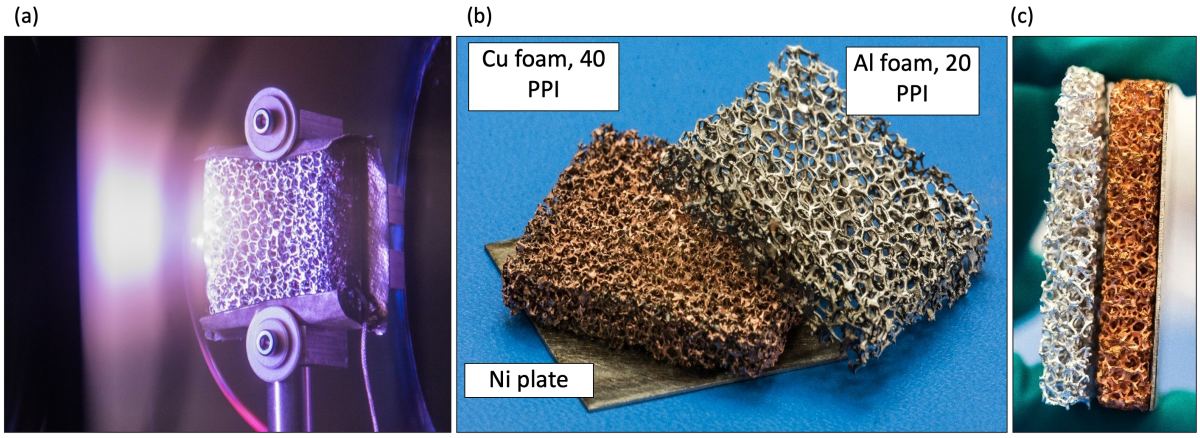

Figure 5.24: (a) Ar plasma column focused on stacked foam materials: A, Cu and a solid nickel backplate, (b) the Al and Cu foam and Ni plate post plasma exposure and ion sputtering and (c) original Al and Cu foams and Ni plate stacked as in the plasma experiment.

The background neutral pressure for this experiment was $P_0 = 2 \times 10^{-2}$ Pa which gives a mean free path of $>$ 1 m at room temperature. Thus, the plasma sheaths are assumed to be collisionless.

The total fluence delivered to the sample is calculated to be $\approx 4\ times10^{21}$ ions/cm^2 over a period of 6 hours. During plasma exposure, LDM imaging and profilometry was used in-situ, as well as a quartz crystal balance to monitor the total time-dependent sputter yield. Witness plates were also installed at various radial positions from the sample for pre- and post- plasma exposure deposition analysis. Images from the erosion video generated during the experiment are shown in Sec 1. Thermal modeling were run using COMSOL of stacked foam geometries and combined with thermocouple measurements of the sample during plasma exposure and show that the Ni backplate surface which was facing the plasma column did not exceed 300^oC.

The Debye length for the plasma in this experiment is:

$$\lambda_D = \sqrt{\frac{\varepsilon_0 k_B T_e}{e\,5\times10^{17}}} = 18\,\mu m. \tag{5.6}$$

From the Child-Langmuir law, the biased sheath thickness L_s is approximately:

$$L_s = \lambda_D \frac{\sqrt{2}}{3}\left(\frac{2e\Delta\phi_s}{T_e}\right)^{3/4} = 350\,\mu m \tag{5.7}$$

where $\Delta\phi_s$ is the potential difference between the plasma and the wall, which in this case is 280 V. The 20 PPI Duocel Al foam has pores which are $D_{Al} \approx 1470 \pm 286\,\mu m$ in diameter. Compared with these foam dimensions, the floating sheath thickness, λ_D is much smaller than the pore diameter, while the biased sheath thickness, L_s is only just smaller than the pore diameter. This suggests that the aluminum foam is at least partially infused with plasma, while the 40 PPI Cu foam, which has pore dimensions closer to the order of the biased sheath thickness ($D_{Cu} = 650\,\mu m$), must be facing. To summarize, for this experiment:

$$\lambda_D << D_{Al}$$

$$L_s < D_{Al}$$

$$L_s \approx D_{Cu}$$

.

In addition to the first order comparison of predicted sheath thicknesses to foam pore dimensions, it is important to note that an infused plasma density is expected to decrease significantly through infusion depth into a sample. Preliminary analysis has shown the plasma density should decrease by a factor of $1/e$. Therefore, even if a foam is infused in its first layers, partial and then no infusion is quickly achieved with increasing sample depth.

Thus, in the dissimilar layered foam experiment, it is expected that the first layers of Al foam are infused and partially with plasma and/or plasma ions, while the Cu is plasma facing.

Post plasma exposure, the stacked foam samples and backplate were separated and analyzed individually on each surface for their chemical composition. Identifying and quantifying the sputter deposition of each dissimilar material allows for an initial understanding of inter-foam transport and can be used for comparing to expected plasma infusion theory and models. SEM imaging was performed at the Materials Science and Engineering Department at UCLA was a FEI NOVA 230 High Resolution SEM on SE (low energy secondary electron mode) and an Everhart-Thornley detector. The same areas which were imaged were also analyzed for their elemental composition using an integrated EDS detector. The results generated from the EDS analysis are shown in Figure 5.24.

Preliminary results show that each surface of the foams and the Ni surface of the backplate which was facing the plasma each experienced some sputter deposition. The relative deposition quantities and patterns can be partially explained using recently developed infusion theory, specifically in combination with theoretical models which show back and forward bias in the direction of sputterants from a curved surface. Five surfaces are analyzed and will be referred to as subsets of the three materials: $S_1 - S_3$ with 1 being Al, 2 being Cu, and 3 being Ni. $S_{1,p}$ is the Al foam surface facing the plasma, $S_{1,2}$ is the Al foam surface facing the Cu foam, $S_{2,1}$ is the Cu foam surface facing the Al foam, $S_{2,3}$ is the Cu foam surface facing the Ni, and $S_{3,2}$ is the solid Ni surface facing the Cu foam.

For each surface, the following is found: $S_{1,p}$ is elementally composed of Al with surface elemental traces of Cu. $S_{1,2}$ is similar to $S_{1,p}$ which is made of Al with Cu traces. $S_{2,1}$ is made of Cu, with surface traces of Al. $S_{2,3}$ is Cu with traces of Al and Ni. Lastly, $S_{3,2}$ is the Ni plate and reveals only Al deposition with $< 2\%$ Cu in its elemental mapping. The results are not immediately intuitive and in order to understand which material sputtered onto which surface, the sputtering physics and foam material opacity must be taken into consideration, as well as an estimate of how many foam layers may have been infused by the plasma during the experiment.

The backsputter factor f_β is defined as the fraction of sputtered material which is ejected back into the plasma, adding to the total measured sputtering yield. The sputtered material which is instead ejected into the forward direction (into the sample itself) is considered to be trapped and remain in the foam surface. The backsputter factor can be calculated using angular sputtering profiles which are incident on foam ligaments at different angles of incidence for different energies. The angular sputtering profile used for calculating the backsputter factor, f_β, is:

$$S(E,\theta,\sigma) = \frac{0.042\sigma'(M_2/M_1,\theta)S_n(E)}{\pi U_s}\cos\sigma\times \left[1-\frac{1}{4}\left(\frac{E_{th}}{E}\right)\left\{\cos\theta\gamma_s(\sigma)+\frac{3}{2}\pi\sin\theta\sin\sigma\cos\Phi\right\}\right] \quad (5.8)$$

where E is the incident ion energy, θ is the ion incidence angle, σ is the sputtered particle ejection angle, Φ is the azimuthal ejection angle, and E_{th} is the sputtering threshold energy [101]. In [110], the backsputter factor was calculated by iterating through ions which form a uniform flux density at equal distance increments in he vertical direction. This backsputter factor was calculated for both a plasma facing and a plasma infused scenario. In the plasma infused case however, the plasma ions are iterated in equal angular intervals around a (circular) ligament. The backsputter factor for the plasma infused case is found to approximate to 0.5 due to the symmetry of the ligament. Figure 5.26 shows the backsputter factor, f_β as a function ion energy for different threshold energies. In the experiment described above, the threshold energy is in the range of

50-80 eV, and the ion energies are 250 - 300 eV. In this range, and accounting for oblique yield, the backsputter factor is almost always > 1. Thus, it can be expected that the plasma-facing layers of the foams in the dissimilar metal foam with backplate experiment almost exclusively backsputter (back towards the plasma), while the plasma-infused layers backsputter and forward-sputter symmetrically. A graphical representation of these scenarios for a circular ligament are also shown in Figure 5.26.

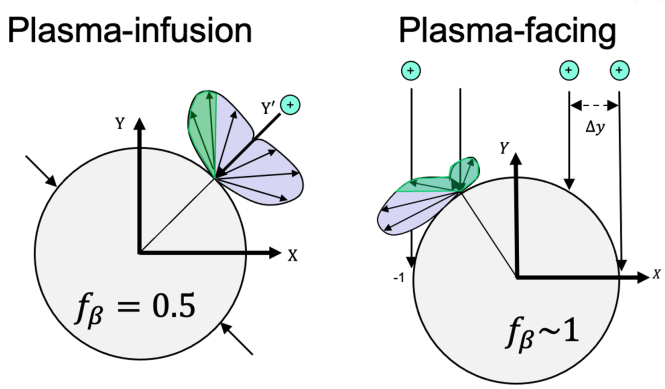

Figure 5.25: Circular ligaments with plasma-infusing and plasma-sputtering backsputter diagrams.

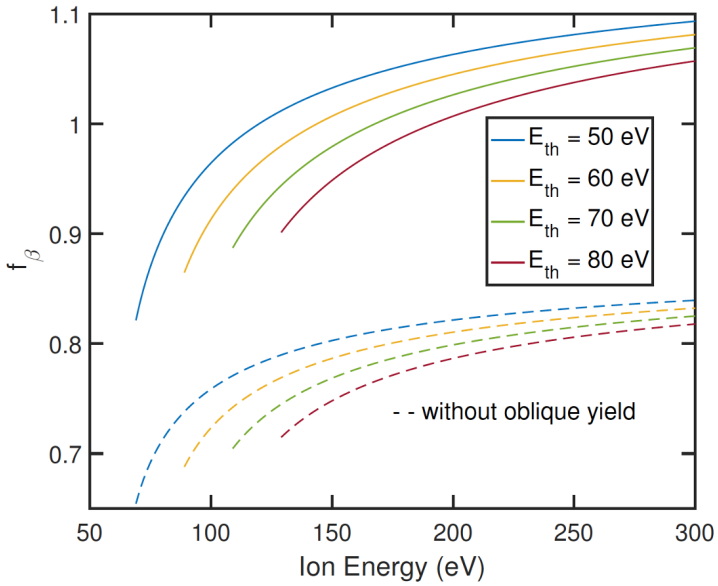

Figure 5.26: Backsputter factor as a function of primary ion energy and threshold energy for surfaces with and without oblique ion incidence. In these experiments, f_β is near or greater than 1 when including oblique incidence in the plasma-facing case [9].

The EDS results shown in the dissimilar foam experiments qualitatively agree with the backsputter theory and plasma infusion. The diagram in Figure 5.27 shows EDS-generated elemental mapping of the surfaces outlined above. Each surface reveals aluminum presence, which suggests that the most plasma facing foam was sputtered in every direction (forward-sputtered and backsputtered).

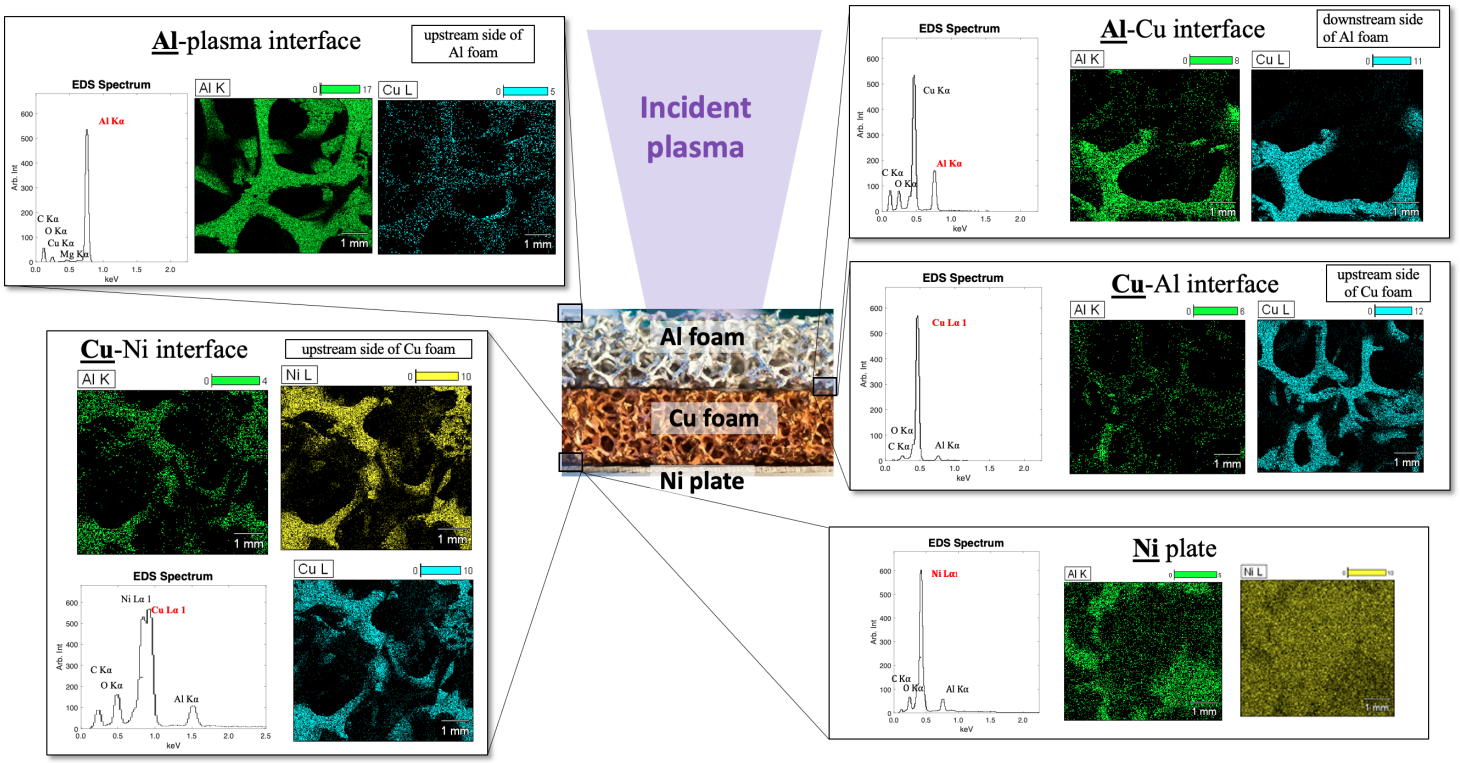

Figure 5.27: EDS-generated elemental mapping projected onto SEM images of each surface analyzed to show which material was deposited onto and through each layer of the stacked plasma-exposed foams with Ni backplate. Aluminum is present on each surface, suggesting forward and backsputtering, while Cu and Ni are only shown to have backsputtered towards the surfaces which are placed behind them.

Figure 5.28 is a graphical representation of the theorized material transport in the stacked plasma-foam with backplate experiment. Aluminum foam which experiences plasma infusion, produces sputterants in every direction back towards the plasma and witness plates, as well as through the foam layers, Cu foam and eventually depositing by some amount onto the Ni plate. The Cu foam ligaments are receiving some primary ions at incidence normal to the sample plane (plasma-facing), and thus expected primarily to backsputter towards the plasma and deposit into the Al foam and onto the witness plates. Lastly, Ni may experience some primary ions which have traveled through the Al and Cu foams, assuming a non-zero transparency, but can only backsputter due to its solid geometry.

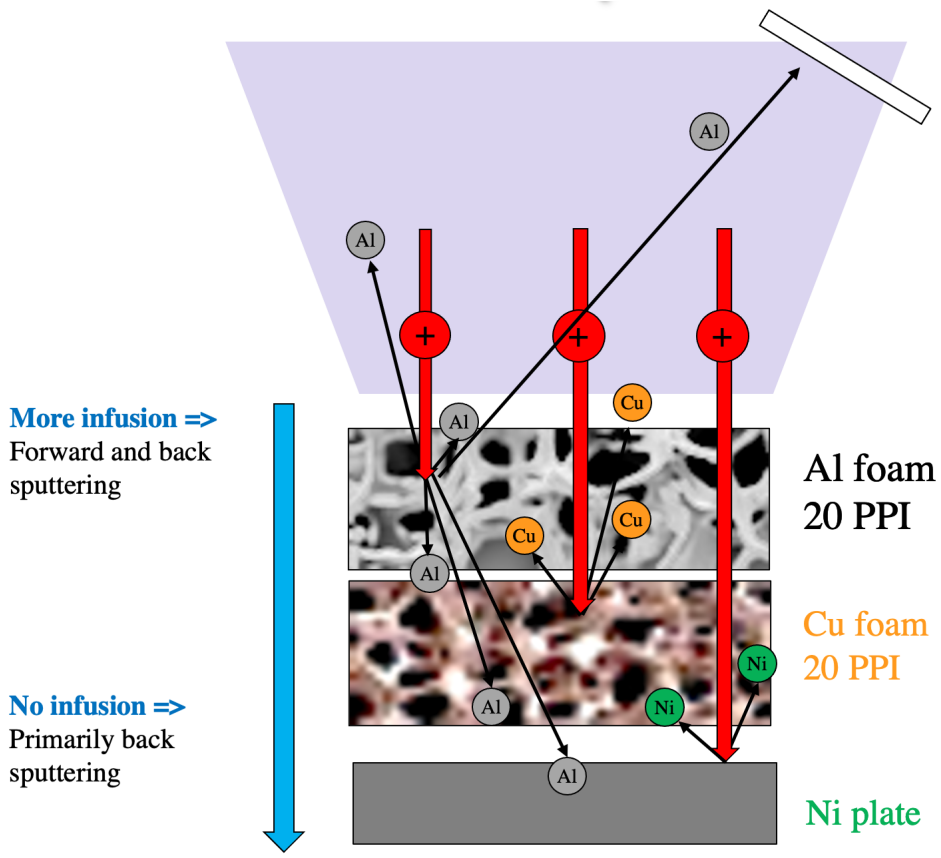

Figure 5.28: Diagram showing predicted foam and backplate material transport mechanisms based on plasma infusion and backsputter theory.

This experiment was repeated using MOChA, with Al and Cu foams of 20 PPI and a Ni backplate. In this experiment, the samples were placed in a custom made boron nitride holder so that the side edges were shielded from the plasma. The anode was made of a graphite cylinder to avoid Cu contamination of the foams. A bias of up to - 500 V was used on the target foam stack, and the plasma Debye length when the sample is floating is 60μ m. The Al and Cu foams both have pore diameters $D = 1120\mu m$ and ligament diameters $d = 150\mu$m, and thicknesses of 0.35 cm. The number of pore layers for each foam is ≈ 2.8, with transparency of 42%. For a plasma density of $n_e = 1 \times 10^{17} m^{-3}$ and an electron temperature $T_e = 6$ eV as described in Chapter 4, the Debye length is expected to vary between 60 μ m to 445 μm for a -500 V target bias. Thus, the first two

layers of the Al foam are expected to be plasma infused and partially infused, and the subsequent layers to be facing.

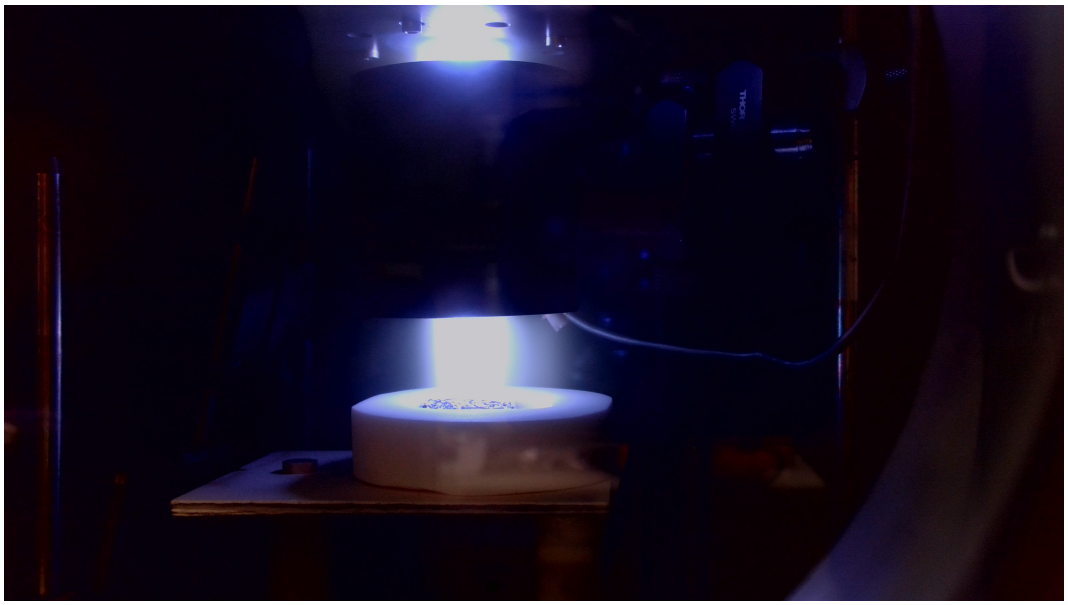

Figure 5.29: Operation of MOChA argon plasma with stacked Al and Cu foams with a Ni backplate in a BN holder. The anode is graphite, and the plasma diameter is 1 cm.

Each surface was examined with EDS elemental mapping as in the previous iteration of the experiment, and quantitatively analyzed using software from Thermo Fischer Scientific. The results are shown in Figure 5.30. The overall foam and Ni backplate transport direction is in agreement with the previous results and with theory, showing Al deposited in both the forward and backward direction, while Cu was found to deposit backwards towards the top Al foam layer, with only trace amount depositing onto the Ni plate. The quantitative results were found by average 5 locations per foam at the center of each sample. Quartz-crystal microbalance (QCM) sputtering data and OES spectra of the near sample region before and during target bias were also acquired. Further analysis includes comparison with more recently developed models which include data generated from atomic simulations in TRIDYN and more accurate geometric foam descriptions such as those found in [112, 27, 113].

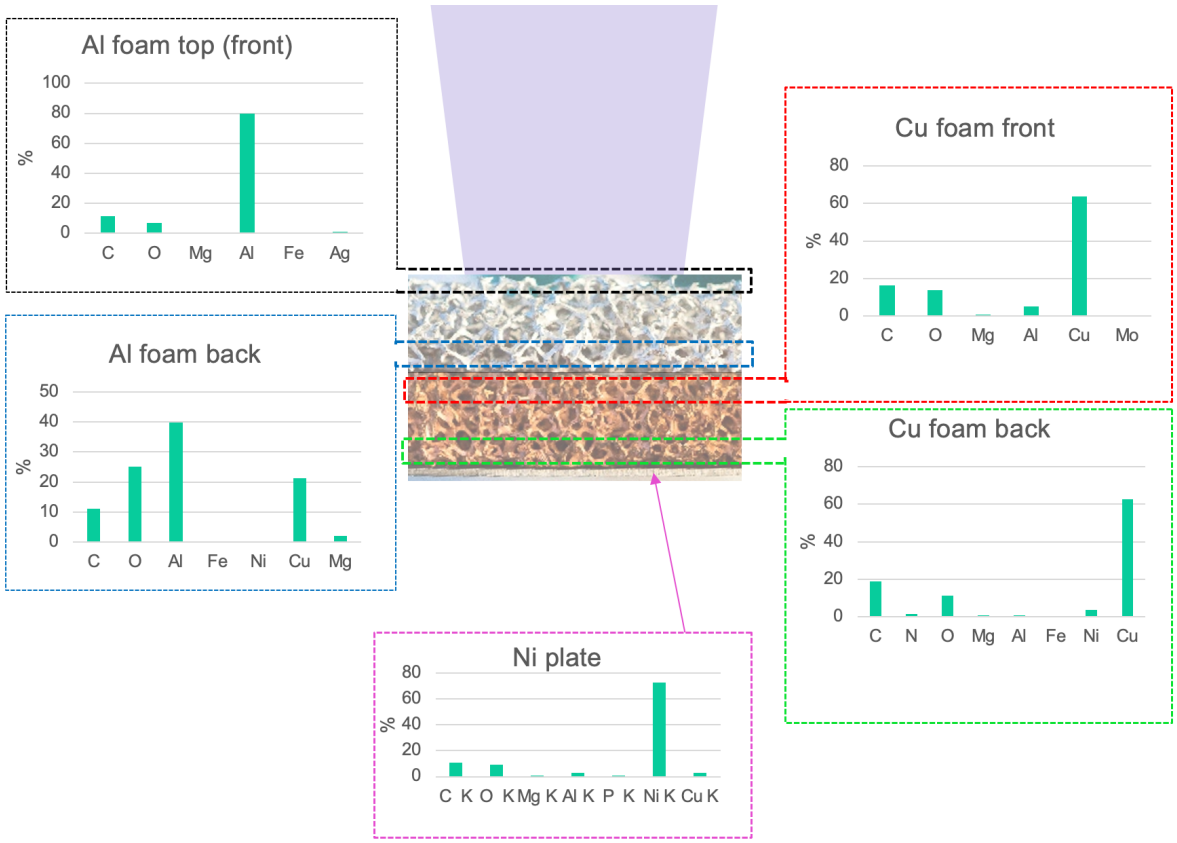

Figure 5.30: EDS quantitative elemental mapping of each surface in the stacked dissimilar foam experiment carried out with MOChA. The relative concentrations of each element was calculated using Thermo Fischer Scientific EDX software.

5.7 Plasma ablation and arcing of a tungsten VCM

5.7.1 Target tungsten samples and setup

The experiment carried out for Plasma-Material Interactions at LAPD is a collaboration between the Mechanical and Aerospace Engineering department and Physics & Astronomy funded by an ARPA-E grant aimed at studying VCMs for use as high power electrode surfaces. A custom sample holder was designed and built out of boron nitride to house a total of 4 target samples: 2 planar W foils and 2 W VCMs. The W VCMs were manufactured by Ultramet, Inc. with varying pore, ligament and volume fill density parameters. Each sample had a diameter of 1 cm and a few mm

thick. Each sample could be biased independently, and thermocouples were wired to each sample to monitor the surface temperatures during the experiments. As shown in Figure 5.31, the sample holder can be lowered and raised into the plasma and rotated during experiment so that each face can be exposed to plasma int he same experiment. A set of removable Cu witness plates were also positioned at 45 degrees from the sample surface for a post-analysis of sputtered and erosion products from the surface of the targets [114].

The biasing schematic is also shown in Figure 5.31. A capacitor bank with a 600 V bias capability was connected between the anode and the W samples, referenced to ground. The samples were inserted into the LAPD device at port n. 30, which is $\approx$ 14 m downstream of the anode grids.

Figure 5.32 shows I-V traces of the plasma discharge measured between anode and cathode, and the samples measured between cathode and target sample. The voltage between sample and cathode was divided by a high-voltage isolator For a nominal shot, the plasma pulse length is 25 ms with the sample bias turned on at t = 5 ms and off at t = 20 ms. The ion saturation current to the sample is $\approx$ 0.9 A for negative biases greater than 50 V.

During these experiments, several shot sequences were taken for flat W and for VCM W for a total of 6 runs. Each run captured up to 1000 plasma shots onto either a flat or VCM W surface, and with biases increasing from floating to - 600 V in steps of 50 V. The main diagnostics which were active for this experiments were Fast-Frame Imaging with a Phantom Fast Cam v.7.3, a long distance microscope with CCD camera, and optical emission spectroscopy at the near-surface region to monitor the erosion products from the samples. In this work, a summary of the I-V trace findings for biased VCM vs flat W and the Fast-Frame-Imagining results will be described.

5.7.2 Results: I-V traces

Experimental runs for flat and VCM biases are illustrated in Figures 5.32 - 5.33. A noteworthy observation in this experiment was the occurrence of bipolar arcing from the W sample surfaces in both the flat and VCM cases to the plasma. The I-V curves suggests that arcing occurs between

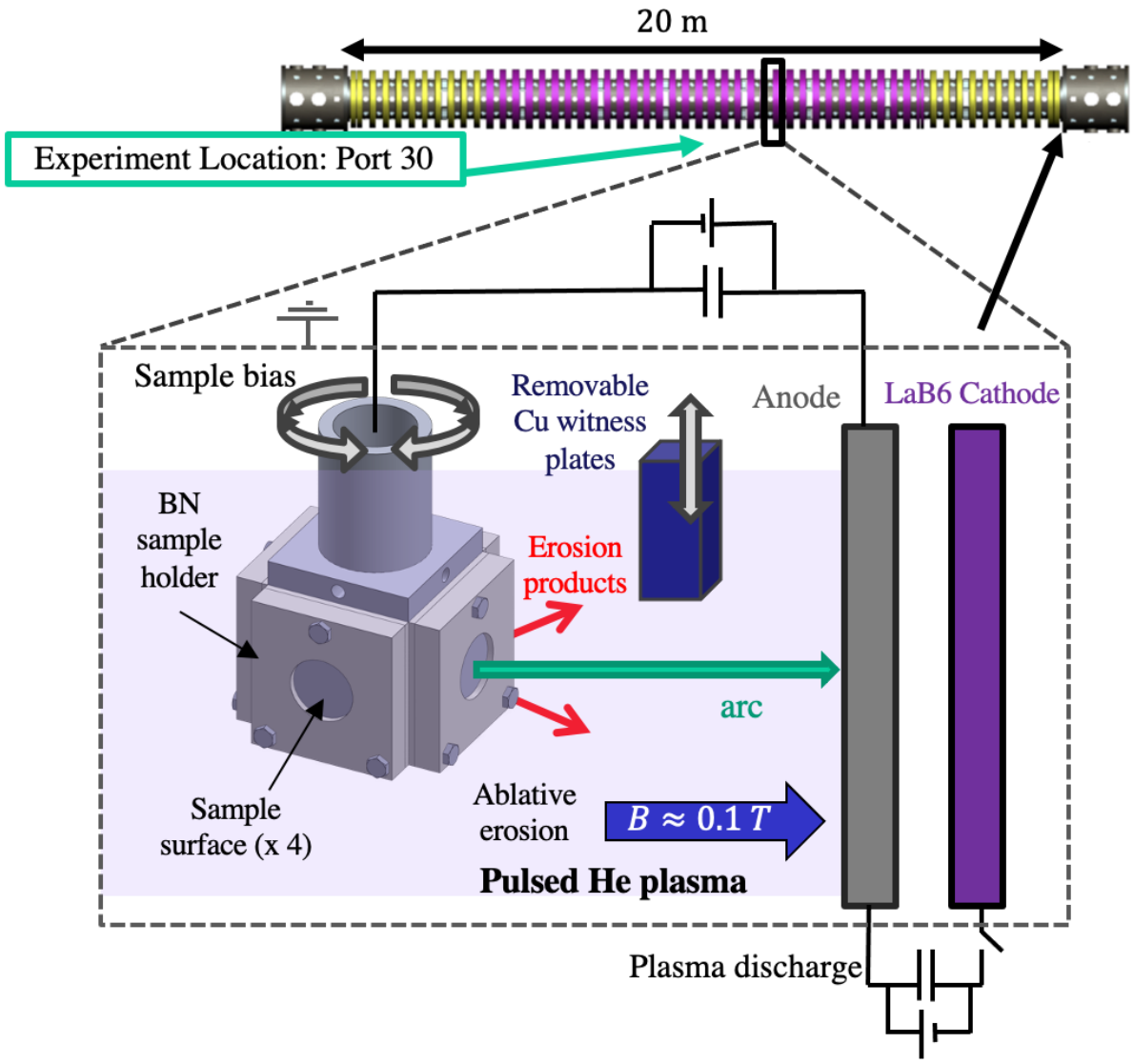

Figure 5.31: BN custom made sample holder with 4 sample surfaces which can rotate into the plasma column. Retractable Cu witness plates were used to monitor deposited erosion products in post-analysis. The anode was connected to the target W samples to achieve negative biases up to - 600 V using a capacitor bank.

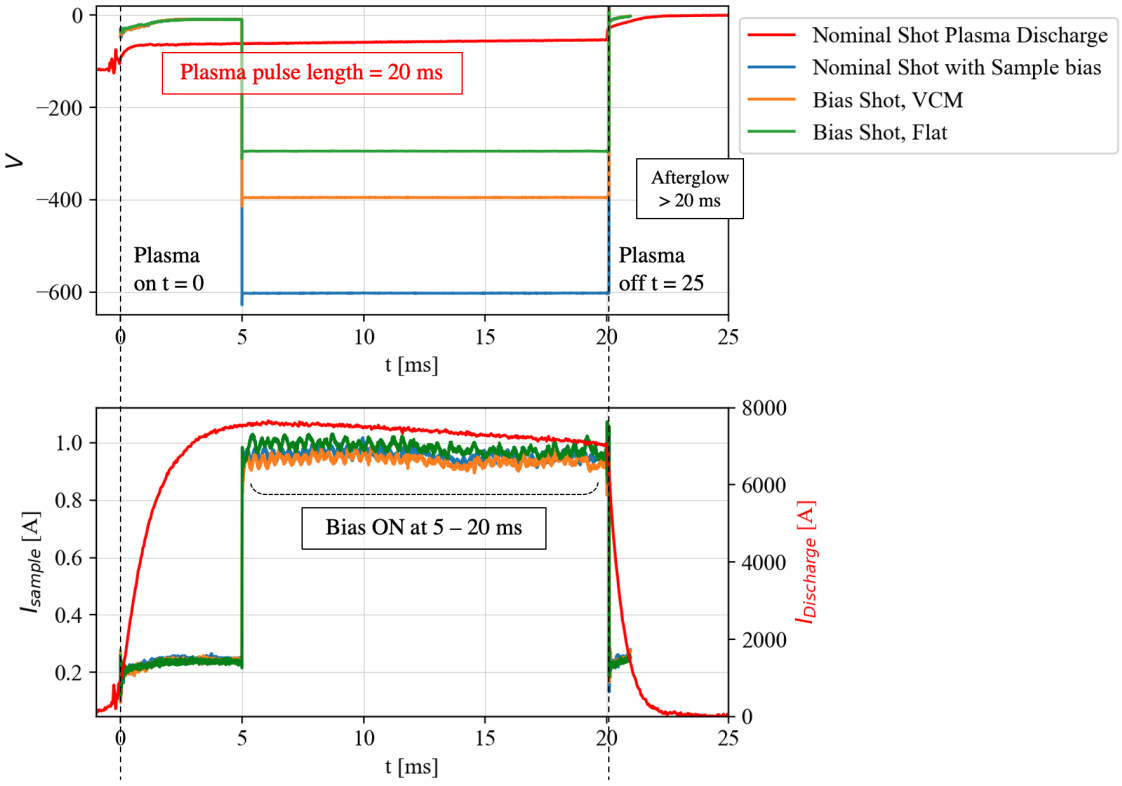

Figure 5.32: I-V traces of the LAPD plasma discharge and the of plasma shots with bias on a VCM at -400 V and on a flat at - 600 V. These traces demonstrate show nominal behavior, with the plasma on at t = 0 ms, bias on at t = 5 ms, and plasma pulse ends and bias off turned at t = 20 ms. The ion saturation current of both the VCM and the flat W is 0.9 A for biases larger than -50 V. The discharge current measured between anode and cathode is 7.5 kA.

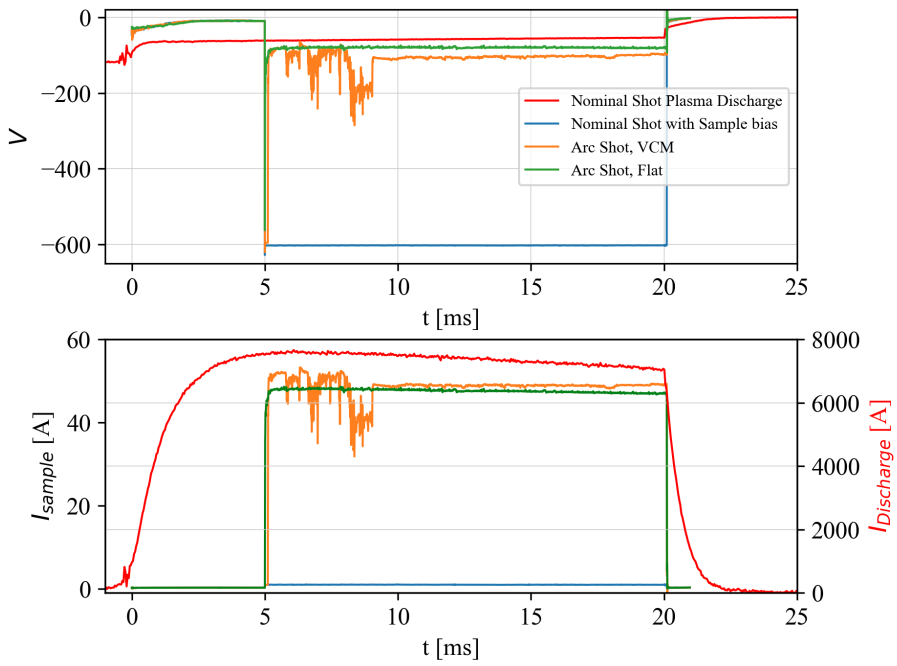

Figure 5.33: I-V traces of the LAPD plasma discharge and the of plasma shots where biased VCM and flat samples displayed an arcing event. In this example, both arcs had average arc currents of 45 A. During an arc, the power supply driving the capacitor bank turns off, and no active bias is measured on the samples.

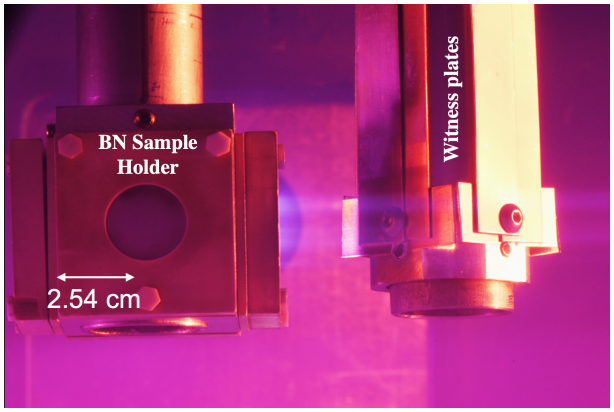

Figure 5.34: A long distance microscope with a camera was pointed through a lateral viewport in LAPD to monitor the sample surface region. The BN holder has four openings for the W flat foils and VCM which were inserted into the plasma column at $\approx 14m$ from the source. Cu witness plates were placed at a 45^o angle from the sample to not block the direct line of the plasma.

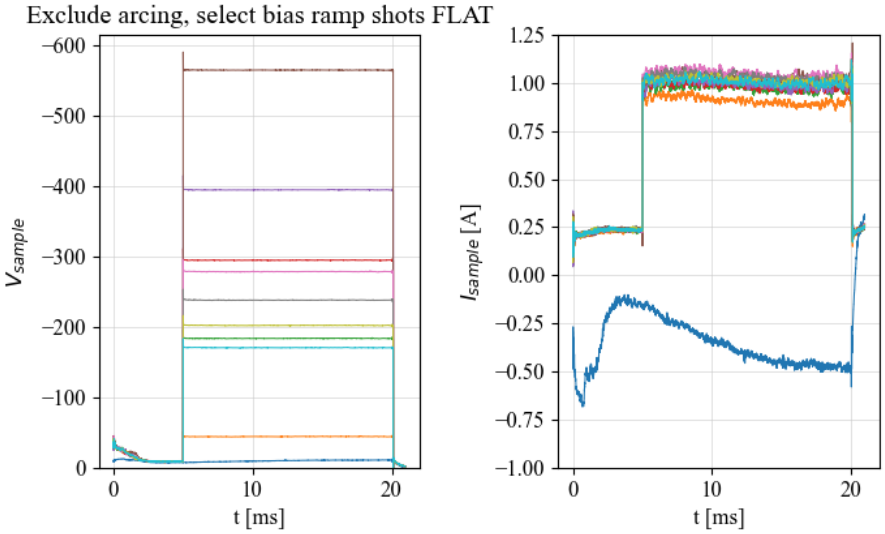

Figure 5.35: 10 select shots with no arcing at different sample biases from a flat W experiment where a total of 392 shots were taken. The maximum current is 1.0 A for nominal, non-arcing conditions.

the biased sample and the LAPD gridded anode. Figure 5.32 displays selected I-V traces for a flat sample, with biases ranging from zero to -580 V, and currents reaching a maximum of 1.0 A to the sample. 5.36 shows plasma shots where arcing occurred at several voltages starting at -75 V. Each shot was analyzed for an arcing criteria, defined as an average current between 5-20 ms exceeding 1.0 A. This enabled us to determine the percentage of arcing events per data run and sample type, as well as the magnitude of each arc. For instance, the experimental run of Figures 5.36 on the flat W surface had a total of 392 shots, 35 of which were arcs. The maximum temperature recorded on the sample was 118^{o}C. Figure 5.38 shows the same traces but for an experimental shot sequence of 498 shots on a W VCM. The maximum temperature recorded for the VCM was 109^{o}C. It is important to note that all the plasma conditions for each experimental run and plasma shot are kept the same in the LAPD, with the only changes being the target surface and bias of the target.

Each data run was analyzed for number of arc shots, arc bias occurrence and average current to sample during an arcing event. The following table summarizes the statistics from this analysis:

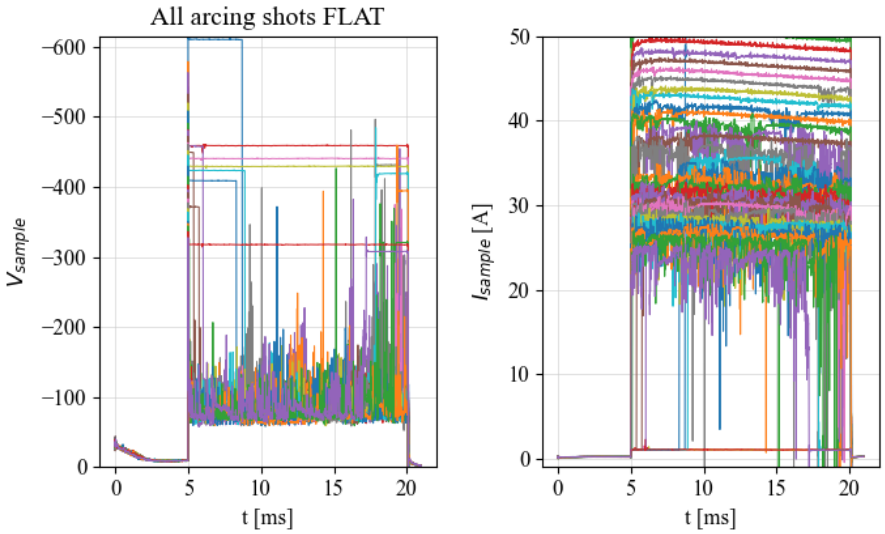

Figure 5.36: All shots with arcs shown for different sample biases from a flat W experiment where a total of 392 shots were taken, and 35 had arcing events. The maximum current for an arc in this experimental run is 50 A.

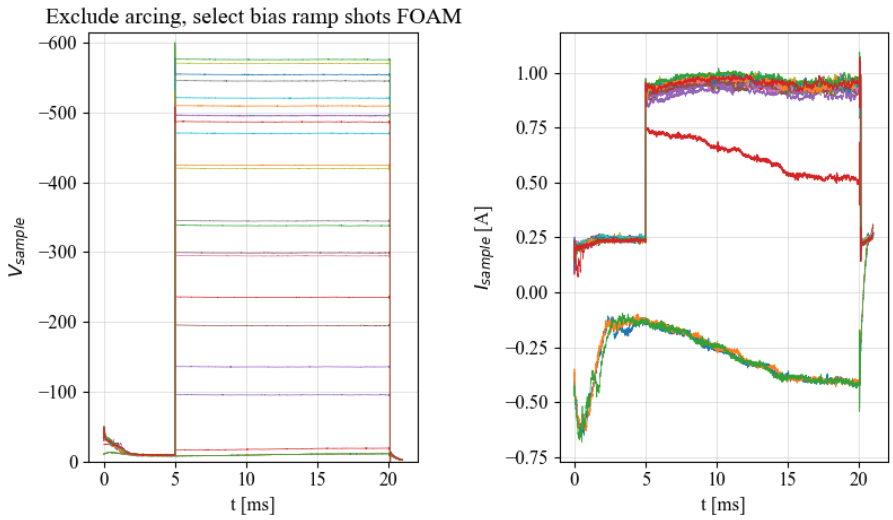

Figure 5.37: 20 select shots of a VCM with several biases, with a maximum current of 1.0 A to the sample. In this experimental run, 498 shots were taken at biases varying from 0 to -600 V.

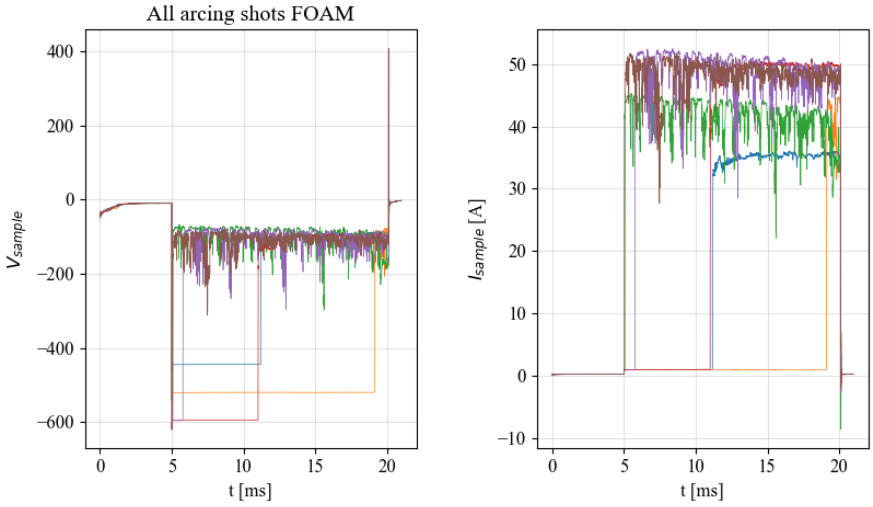

Figure 5.38: All arcing shots for the experimental VCM run shown in Figure 5.38. In this sequence of 498 shots, 4 showed arcing with a maximum (electron) arc current of 52 A.

Run	n total shots	n arcs	ave arc current [A]	max bias	% arcing
total flat	1500	131	- 400 V	22.35	8.73
total VCM	8457	22	29.4	-610 V	0.26

Table 5.3: 6 total experimental runs each with several hundreds of plasma shots with varying sample biases from 0 V to - 600 V were analyzed for arcing behavior. An arc was defined to be when sample current exceeded its saturation current by 10%.

These results reveal that the occurrence of an arc was higher for a flat W target than a VCM W target, and that the maximum achievable bias without arcing was higher for a VCM than a flat W target. However, the magnitude of arc current was high from a VCM than from a flat. This could be due to increased surface area of the VCM which could contribute to higher electron emission current in an arcing event. A visual representation of the statistical findings is shown in Figure 5.39.

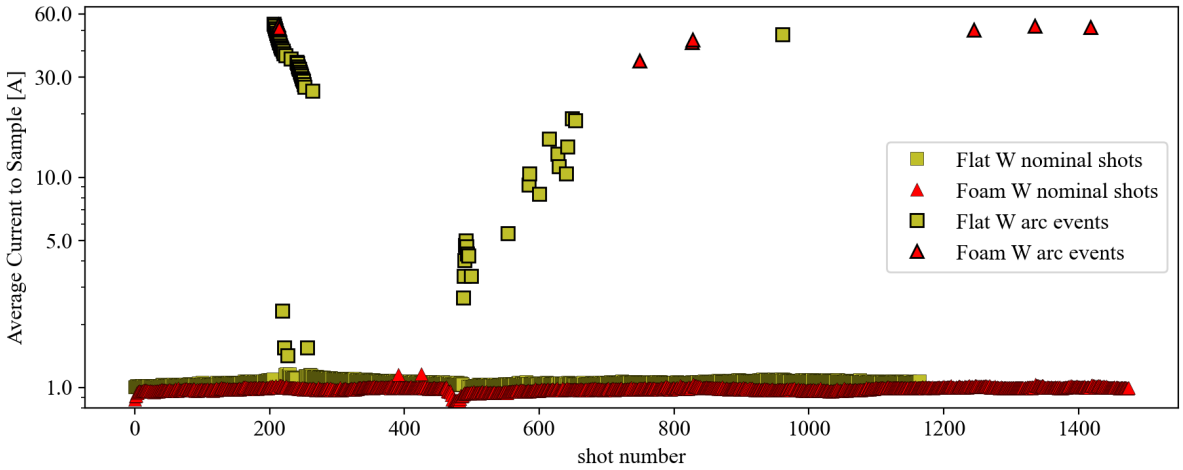

Figure 5.39: 1500 VCM and 1200 flat shots with arcing events and average arc currents. Nominal shot current with no arc is 1.0 A for both flat and VCM W.

5.7.3 Fast-Frame Imaging

To take a closer look at the bipolar arcing behavior, a fast-camera revealed snap shots of the arcs on the VCM surface compared to the flat W surface. A Phantom 7.3 camera was set to point at a viewport which was perpendicular to the sample. To capture detailed images of arcing on the sample surfaces, the targets were turned by 45^o to face the camera. The camera frame rate was 21052 frames per second, and the length of the plasma shot was captured for multiple shots with and without arcing events. Figure 5.40 shows still frames of an flat and W arcing event. This fast-frame imaging diagnostic releaved two important properties of arcing on the VCM versus flat surface: (1) the erosion products from what is hypothesized to be ablative erosion are reduced for the VCM, and (2) the arc hot spot origin location appears to remain localized for a flat W target while moving across ligaments for the W VCM. The decreased sputter and erosion products could partially be explain from geometric trapping properties of a VCM, while the non-localized arc origin could be a results of larger heat and current spread across a VCM surface. However, a larger current from the VCM arcing might be due to increased surface area compared to a flat W surface. This result may support SEE behavior studies from reticulated VCM foams which showed larger secondary electron generation from a curved, large surface surface compared, but with total

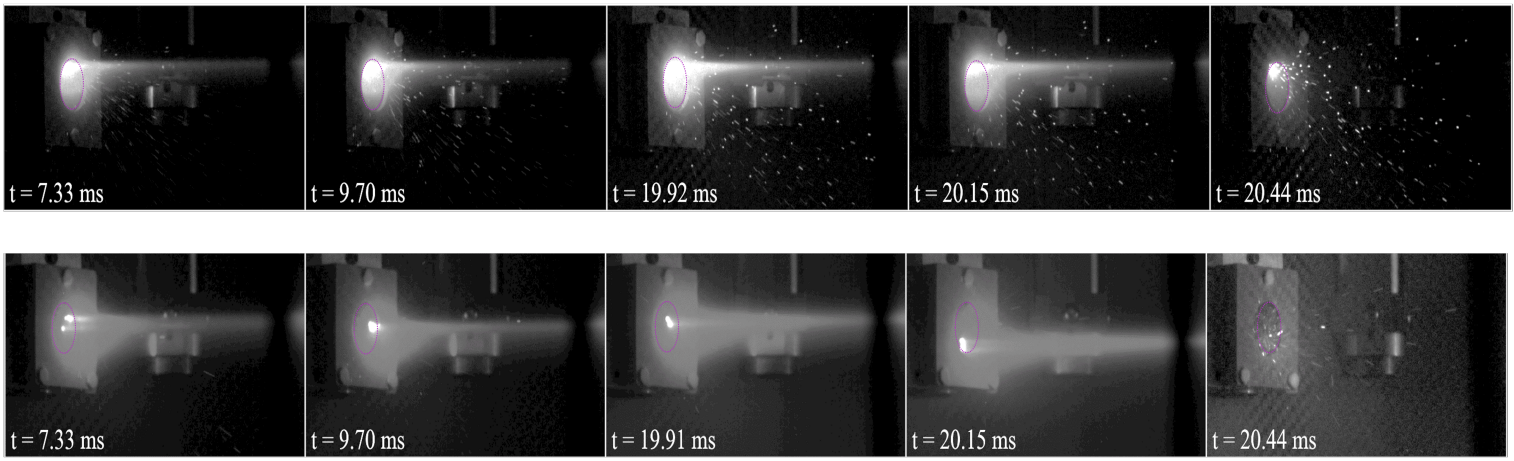

Figure 5.40: (top row) Flat W target during an arcing event. The arc hot spot appears to stay at one location on the surface of the target throughout the length of the shot. (bottom row) VCM W target during arcing. The arc hot spot appears to move across the ligament surfaces during the plasma shot.

emitted particles ultimately reduced via geometric trapping.

5.8 Ongoing and future work

Many efforts are currently ongoing following this VCM as a high voltage electrode experiment in LAPD. Careful analysis of optical emission spectroscopy data is underway to investigate the presence of W in the near-surface region of a VCM with and without an arc. Post-experimental microscopy and composition analysis as well as weight loss measurements confirm the reduction of erosion from a VCM surface, and a modeling effort using COMSOL is underway to predict and understand arcing behavior. Lastly, arc tracking and erosion product tracking techniques of the fast-camera videos are being developed to learn how arc hot spots moves across a VCM surface.

CHAPTER 6

Conclusions

6.1 Summary

Designing plasma-favorable materials can lead to the mitigation of many PMI effects such as PMI-driven instabilities, material erosion and degradation, plasma contamination, and bulk plasma cooling. VCMs have shown to be promising candidates for plasma-facing components due to geometric trapping of emitted particles such as from secondary electron emission (SEE) and sputtering. In addition, recent advances in manufacturing may allow for tailored design and tuning of some PMI properties of a VCM. This dissertation has provided a deeper understanding of PMI and of electron emission from VCM surfaces, the contribution and importance of a backplate component and the general behavior of material transport from sputtering within a VCM. Carbon was used as a baseline material as it is easily available in the reticulated foam space, and can be directly compared to previous studies on carbon complex surfaces. In addition, carbon can be a surrogate for other elements such as copper, tungsten or steel which can be manufactured into foam structures and whose SEE yields geometric trapping effects should behave similarly.

It is found that foam transparency of a primary electron beam to a backplate is a useful metric for characterizing sample geometry and SEE yield. An analytical exponential decay expression was developed and verified experimentally to describe foam transparency as a function of PPI, sample thickness, and foam aspect ratio A_R. In this work, SEM imaging was used to determine SEE yield trends of carbon foams with varying geometries, however, in combination with foam transparency, it is also possible to distinguish and quantify the backplate SEE contribution. For

a foam with a fixed aspect ratio of $D/d = 5$, it is found that higher PPI foams show better SEE suppression due to lower transparency and thus reduced backplate SE contribution. Foams with higher or lower aspect ratios might show different SE suppression trends with PPI, and this was studied with a direct measurement approach. The isotropic nature of reticulated foams allows sustained suppression with angular primary electron beam tilt, similar to fuzz surfaces.

VCMs could be designed for use in concert with other roughened or SEE-reducing surface backplates. Instead of requiring increased thickness for reducing transparency and yield, thin samples of a few pores could be used with low SEE yield backplates. This design concept could achieve SEE yield reduction of over 70% by utilizing versatile foam surfaces at moderate PPI and thickness. A simple exponential expression was also found to approximate transparency as a function of D, d and t (or PPI and t), in good agreement with optical and SEM experiments. PPI has not been found to affect yield as much as transparency, which is supported by theoretical models.

By using a direct measurement setup, the SEE yield of reticulated carbon foams with PPI ranging from 5 to 100 and with different aspect ratios was found to be reduced by up to 43% compared to flat graphite, which is in agreement with previous work and analytical models [68, 6, 4]. An optimal regime was found for maximum SEE suppression (or minimum SEE yield) for a reticulated carbon foam with 40 PPI. This optimal geometric configuration is for an aspect ratio of $A_R = 8.4$ and a foam thickness of 6.25 mm, which has been validated by models. Foams may display multi-scale behavior when ligaments are pores are in the mm range compared to the *mu* m range: for large ligaments, foams display "fiber-like" behavior and a directional with incident electron beam angle. Smaller pores and ligaments, such as in foams of 100 PPI, behave similar to fuzzes and display a loss of angular dependence of SEE yield with primary angle of incidence. A dedicated model, AMPS-E, was developed to support and investigate the experimental results of SEE.

Electron spectroscopy was experimentally performed to understand the contribution to SEE yield of low and high energy secondary electrons. The backscattered electron reduction is larger

for a foam than the true SE reduction: foams may be emissive in the low energy range due to angled and tilted surfaces, but are effective at redirecting BSEs back into the foam more than trapping true SEs. This could be important in applications where BSEs are the only SEs of interest, such as in backscattered electron detectors of SEMs. Lastly, the contribution of true SEs to total SEE yield has been found to be higher for a foam than for a flat surface.

A new compact device at UCLA capable of rapid erosion, sputtering and complete with a suite of plasma and material diagnostics is available at UCLA. Results and predictions of foam material transport will be compared to currently developed models which include atomic simulation data generated from TRIDYN as described in [115, 113, 112]. Experimental dissimilar stacked foam experiments are in qualitative agreement with analytical predictions of forward and back sputter behavior based on plasma-infusion parameters [9, 55]. A new diagnostic was also commissioned for visualizing plasma-erosion and measuring surface recession using depth-from-focus algorithms and an LDM. Using this diagnostic with an Al foam exposed to Xe plasma sputtering has demonstrated intermediate erosion mechanisms and provides insight which otherwise cannot be measured with pre/post situ sample analysis. A user facility was used in a collaboration project with UCLA Physics to investigate the effect of biased tungsten foams in a pulsed He plasma on material erosion and arcing in comparison with a planar surface. By using fast-frame imaging and by acquiring plasma discharge and sample I-V traces for $\approx$ 3000 20 ms long He plasma shots, it was found that foams can withstand up to 600 V negative bias. W foams also showed significant reduction of arcing events when comparing to planar W surfaces.

6.2 Future Work and Potential Applications

The VCM-plasma interactions studied and results found in this work have many applications in the field of plasma technologies and beyond: metallic and conductive VCMs design can be extended to dielectric materials for advancing RF component manufacturing, as well as EP thruster na dspacecraft component development. Electrodes made with VCMs can also be used [116, 117]

to withstand extreme conditions such as fusion device walls, divertors and edge-biasing electrodes for mitigating arcing, ablation, contamination and erosion. By using advanced modeling techniques and simulations, it may also be possible to tailor properties such as ligament geometry to tune the direction of back and forward sputtered particles within a VCM for self-healing designs.

AMPS-E as a rapid analytical model option can be used to model combinations of foam surfaces with roughened or multi-featured backplates for further electron emission yield tunability and optimization. These results, techniques and measurements are also applicable to environments where surfaces experience photoelectron emission, such as for in-space outer-facing materials on satellites, charged particle diagnostic components, and other spacecraft surfaces.

Ongoing efforts based on the work presented in this thesis include using high fidelity models for multiphysics simulations in complex geometries, such as with COMSOL. Thermal modeling has been performed of regular VCM-like structures to monitor heat loads onto target foams during plasma experiments. By using the particle tracing module in COMSOL combined with sputter theory from [118] for the angular distribution and sputter yield of incident ions on a material surface, Monte-Carlo modeling can be performed on complex geometries. The publicly available Monte Carlo simulation program, TRIDYN [119] is also used to verify the analytical functions input into our COMSOL models.

Future related experiments and studies of SEE of complex surfaces extend to pulsed setups for measuring non-conductive surfaces, and electron spectroscopy can be repeated using a CMA or LEEDS optics [79] on a wide range of materials for analyzing secondary electron energy distributions. These analyses are helpful for applications where it is critical to predict low energy (cold) electron population introduction into a system compared with specularly reflected primary electrons. This is important, for example, in electron microscopy.

The plasma-VCM experiments described in this thesis have presented a qualitative initial understanding of the behavior of plasma-infusion and sheath physics on complex structures. Future techniques may include the use of emissive probing to monitor the sheath thickness [62] near the VCM surface as a function of surface morphology evolution during plasma ion sputtering. This

time-depending experiments would inform the lifetime and durability of VCM-based components.

Overall, it is my hope that ongoing and future work in related experiments, theory, and modeling can leverage the results of this thesis to continue the improvement and understanding of PMI for a wide range of applications.

Bibliography

[1] A. Ottaviano, A. Thuppul, J. Hayes, C. Dodson, G. Z. Li, Z. Chen, and R. E. Wirz, "In situ microscopy for plasma erosion of complex surfaces," *Review of Scientific Instruments*, vol. 92, no. 7, p. 073701, 2021.

[2] A. Piel, *Plasma physics: an introduction to laboratory, space, and fusion plasmas*. Springer, 2017.

[3] J. I. Goldstein, D. E. Newbury, J. R. Michael, N. W. Ritchie, J. H. J. Scott, and D. C. Joy, "Secondary electrons," in *Scanning Electron Microscopy and X-Ray Microanalysis*. Springer, 2018, pp. 29–37.

[4] C. Swanson and I. D. Kaganovich, "Modeling of reduced secondary electron emission yield from a foam or fuzz surface," *Journal of Applied Physics*, vol. 123, no. 2, p. 023302, 2018.

[5] A. Ottaviano and R. Wirz, "Modeling of secondary electron emission from volumetrically complex surfaces," in *International Electric Propulsion Conference*. ERPS, 2022, p. 525.

[6] A. Ottaviano and R. E. Wirz, "Secondary electron emission of reticulated foam materials," *Journal of Applied Physics*, vol. 133, no. 10, p. 103302, 2023.

[7] W. Gekelman, H. Pfister, Z. Lucky, J. Bamber, D. Leneman, and J. Maggs, "Design, construction, and properties of the large plasma research device- the lapd at ucla," *Review of scientific instruments*, vol. 62, no. 12, pp. 2875–2883, 1991.

[8] M. Konopliv, A. Thuppul, and R. Wirz, "Validation of collisional radiative models for low temperature xenon plasmas," in *APS Division of Plasma Physics Meeting Abstracts*, vol. 2021, 2021, pp. PP11–012.

[9] G. Z. Li, "Plasma sputtering behavior of structured materials," Ph.D. dissertation, UCLA, 2020.

[10] M. T. N. Fusion and undefined 2018, "Assessment for erosion of and impurity deposition on first mirrors in a fusion reactor Related content," *iopscience.iop.org*, 2018. [Online]. Available: https://doi.org/10.1088/1741-4326/aac95c

[11] A. Alba, R. M. Aguilar-Ponce, J. F. Vigueras-Gómez, and E. Arce-Santana, "Phase correlation based image alignment with subpixel accuracy," in *Lecture Notes in Computer Science (including subseries Lecture Notes in Artificial Intelligence and Lecture Notes in Bioinformatics)*, vol. 7629 LNAI, no. PART 1, 2013, pp. 171–182.

[12] I. Levchenko, S. Xu, G. Teel, D. Mariotti, M. Walker, and M. Keidar, "Recent progress and perspectives of space electric propulsion systems based on smart nanomaterials," *Nature communications*, vol. 9, no. 1, pp. 1–19, 2018.

[13] R. E. Wirz, J. R. Anderson, D. M. Goebel, and I. Katz, "Decel grid effects on ion thruster grid erosion," *IEEE transactions on plasma science*, vol. 36, no. 5, pp. 2122–2129, 2008.

[14] D. M. Goebel and I. Katz, *Fundamentals of electric propulsion: ion and Hall thrusters*. John Wiley & Sons, 2008, vol. 1.

[15] D. Sydorenko, A. Smolyakov, I. Kaganovich, and Y. Raitses, "Kinetic simulation of secondary electron emission effects in hall thrusters," *Physics of Plasmas*, vol. 13, no. 1, p. 014501, 2006.

[16] Y. Raitses, A. Smirnov, D. Staack, and N. Fisch, "Measurements of secondary electron emission effects in the hall thruster discharge," *Physics of Plasmas*, vol. 13, no. 1, p. 014502, 2006.

[17] R. Wirz, A. Collins, Z. Chen, C. Huerta, G. Li, S. Samples, A. Thuppul, P. Wright, N. Uchizono, H. Huh *et al.*, "Electric propulsion activities at the ucla plasma & space propulsion laboratory," in *The 36th International Electric Propulsion Conference, IEPC-2019*, vol. 547, 2019.

[18] G. Li, C. Dodson, R. Wirz, T. M. n. A. . . . , and undefined 2016, "Implementation of in situ diagnostics for sputter yield measurements in a focused plasma," *arc.aiaa.org*. [Online]. Available: https://arc.aiaa.org/doi/pdf/10.2514/6.2016-4841

[19] M. Patino, Y. Raitses, R. W. A. P. Letters, and undefined 2016, "Secondary electron emission from plasma-generated nanostructured tungsten fuzz," *aip.scitation.org*. [Online]. Available: https://aip.scitation.org/doi/abs/10.1063/1.4967830

[20] M. Patino, Y. Raitses, and R. Wirz, "Secondary electron emission from plasma-generated nanostructured tungsten fuzz," *Applied Physics Letters*, vol. 109, no. 20, nov 2016.

[21] M. Campanell, A. Khrabrov, and I. Kaganovich, "Absence of debye sheaths due to secondary electron emission," *Physical review letters*, vol. 108, no. 25, p. 255001, 2012.

[22] A. Vasilyev, A. Arakcheev, , I. B. N. M. . . . , and undefined 2017, "In-situ imaging of tungsten surface modification under ITER-like transient heat loads," *Elsevier*. [Online]. Available: https://www.sciencedirect.com/science/article/pii/S235217911630117X

[23] A. Ottaviano, G. Z. Li, C. E. Huerta, A. Thuppul, Z. Chen, C. A. Dodson, and R. E. Wirz, "Plasma-Material Interactions for Electric Propulsion: Challenges, Approaches and Future," Tech. Rep., 2019. [Online]. Available: http://electricrocket.org/2019/517.pdf

[24] J. M. Sattler, R. A. Coutu Jr, R. Lake, T. Laurvick, T. Back, and S. Fairchild, "Modeling micro-porous surfaces for secondary electron emission control to suppress multipactor," *Journal of Applied Physics*, vol. 122, no. 5, p. 055304, 2017.

[25] G. Z. Li, R. E. Wirz, T. S. Matlock, M. Goebel, R. Conversano, and R. E. Wirz, "Plasma Sources Science and Technology A dc plasma source for plasma-material interaction experiments Recent citations Persistent Sputtering Yield Reduction in Plasma-Infused Foams A dc plasma source for plasma-material interaction experiments," *Plasma Sources Science and Technology Plasma Sources Sci. Technol*, vol. 23, p. 11, 2014. [Online]. Available: https://iopscience.iop.org/article/10.1088/0963-0252/23/2/025014/meta

[26] T. S. Matlock, D. M. Goebel, and R. E. Wirz, "Near anode plasma in the plasma interaction facility at ucla," in *33rd International Electric Propulsion Conference*, 2013.

[27] A. Thuppul, M. Konopliv, and R. Wirz, "Plasma interactions and sputtering erosion for plasma-infused volumetrically-complex surfaces," *Bulletin of the American Physical Society*, vol. 66, 2021.

[28] A. Ottaviano, G. Li, C. Huerta, A. Thuppul, Z. Chen, C. Dodson, and R. Wirz, "Plasma-material interactions for electric propulsion: challenges, approaches and future," in *The 36th International Electric Propulsion Conference, Austria*, 2019.

[29] C. Huerta, M. Patino, and R. Wirz, "Secondary electron emission from textured surfaces," *Journal of Physics D: Applied Physics*, vol. 51, no. 14, p. 145202, 2018.

[30] M. G. L. Gustafsson, "Surpassing the lateral resolution limit by a factor of two using structured illumination microscopy," Tech. Rep., 2000. [Online]. Available: https://onlinelibrary.wiley.com/doi/abs/10.1046/j.1365-2818.2000.00710.x

[31] G. Hobbs and J. Wesson, "Heat flow through a langmuir sheath in the presence of electron emission," *Plasma Physics*, vol. 9, no. 1, p. 85, 1967.

[32] I. Adamovich, S. D. Baalrud, A. Bogaerts, P. Bruggeman, M. Cappelli, V. Colombo, U. Czarnetzki, U. Ebert, J. G. Eden, P. Favia *et al.*, "The 2017 plasma roadmap: Low temperature plasma science and technology," *Journal of Physics D: Applied Physics*, vol. 50, no. 32, p. 323001, 2017.

[33] A. T. Forrester, "Large ion beams: fundamentals of generation and propagation," *New York, Wiley-Interscience, 1988, 338 p.*, 1988.

[34] C. Williams and O. Becklund, "Introduction to the optical transfer function," 2002. [Online]. Available: https://books.google.com/books?hl=en&lr=&id=b5tVkUq3j4EC&oi=fnd&pg=PA1&ots=m7Qa1tWzDZ&sig=YXL5tWgKP6Nu97zllwD26MJDt1A

[35] T. Sheridan and J. Goree, "Collisional plasma sheath model," *Physics of Fluids B: Plasma Physics*, vol. 3, no. 10, pp. 2796–2804, 1991.

[36] I. Lee, M. Mahmood, T. C. M. And, and undefined 2015, "Robust focus measure operator using adaptive log-polar mapping for three-dimensional shape recovery," *search.proquest.com*. [Online]. Available: https://search.proquest.com/openview/cb3a4dabae54efaa7f12eb9a58e86104/1?pq-origsite=gscholar&cbl=33692

[37] M. Patino, Y. Raitses, and R. Wirz, "Secondary electron emission from plasma-generated nanostructured tungsten fuzz," *Applied Physics Letters*, vol. 109, no. 20, p. 201602, 2016.

[38] C. Huerta, M. Patino, R. W. J. o. P. D. Applied, and undefined 2018, "Secondary electron emission from textured surfaces," *iopscience.iop.org*, 2018. [Online]. Available: https://doi.org/10.1088/1361-6463/aab1ac

[39] C. Swanson, "Control of secondary electron emission flux through surface geometry," 2018.

[40] A. Ottaviano, S. Banerjee, and Y. Raitses, "A rapid technique for the determination of secondary electron emission yield from complex surfaces," *Journal of Applied Physics*, vol. 126, no. 22, p. 223301, 2019.

[41] C. Jin, A. Ottaviano, and Y. Raitses, "Secondary electron emission yield from high aspect ratio carbon velvet surfaces," *Journal of Applied Physics*, vol. 122, no. 17, nov 2017.

[42] G. Z. Li, C. A. Dodson, R. E. Wirz, T. S. Matlock, and D. M. Goebel, "Implementation of in situ diagnostics for sputter yield measurements in a focused plasma," in *52nd AIAA/SAE/ASEE Joint Propulsion Conference, 2016*. American Institute of Aeronautics and Astronautics Inc, AIAA, 2016. [Online]. Available: http://arc.aiaa.org

[43] G. Z. Li, R. E. Wirz, T. S. Matlock, M. Goebel, R. Conversano, and R. E. Wirz, "Plasma Sources Science and Technology A dc plasma source for plasma-material interaction experiments Recent citations Persistent Sputtering Yield Reduction in Plasma-Infused

Foams A dc plasma source for plasma-material interaction experiments," *Plasma Sources Science and Technology Plasma Sources Sci. Technol*, vol. 23, p. 11, 2014. [Online]. Available: https://iopscience.iop.org/article/10.1088/0963-0252/23/2/025014/meta

[44] T. M. Biewer, J. C. Sawyer, C. D. Smith, and C. E. Thomas, "Dual laser holography for in situ measurement of plasma facing component erosion (invited)," *Review of Scientific Instruments*, vol. 89, no. 10, oct 2018.

[45] M. Roth and M. Schollmeier, "Ion acceleration-target normal sheath acceleration," *arXiv preprint arXiv:1705.10569*, 2017.

[46] M. Goeckner, J. Goree, and T. Sheridan, "Measurements of ion velocity and density in the plasma sheath," *Physics of Fluids B: Plasma Physics*, vol. 4, no. 6, pp. 1663–1670, 1992.

[47] A. Von Keudell and V. Schulz-Von Der Gathen, "Foundations of low-temperature plasma physics—an introduction," *Plasma Sources Science and Technology*, vol. 26, no. 11, p. 113001, 2017.

[48] R. Franklin, "The plasma–sheath boundary region," *Journal of Physics D: Applied Physics*, vol. 36, no. 22, p. R309, 2003.

[49] S. D. Baalrud, B. Scheiner, E. V. Barnat, M. Hopkins, and B. T. Yee, "Interaction of biased electrodes and plasmas: sheaths, double layers and fireballs," *Plasma Sources Science and Technology*, 2020.

[50] F. F. Chen *et al.*, *Introduction to plasma physics and controlled fusion*. Springer, 1984, vol. 1.

[51] E. Jaeger, L. Berry, J. Tolliver, and D. Batchelor, "Power deposition in high-density inductively coupled plasma tools for semiconductor processing," *Physics of Plasmas*, vol. 2, no. 6, pp. 2597–2604, 1995.

[52] J. Andrews and J. Allen, "Theory of a double sheath between two plasmas," *Proceedings of the Royal Society of London. A. Mathematical and Physical Sciences*, vol. 320, no. 1543, pp. 459–472, 1971.

[53] B. Scheiner, S. D. Baalrud, B. T. Yee, M. M. Hopkins, and E. V. Barnat, "Theory of the electron sheath and presheath," *Physics of Plasmas*, vol. 22, no. 12, p. 123520, 2015.

[54] K. Stephens and C. Ordonez, "Sheath and presheath potentials for anode, cathode and floating plasma-facing surfaces," *Journal of applied physics*, vol. 85, no. 5, pp. 2522–2527, 1999.

[55] G. Z. Li and R. E. Wirz, "Persistent sputtering yield reduction in plasma-infused foams," *Physical Review Letters*, vol. 126, no. 3, p. 035001, 2021.

[56] H. Bruining, *Physics and Applications of Secondary Electron Emission: Pergamon Science Series: Electronics and Waves—a Series of Monographs*. Elsevier, 2016.

[57] J. Scholtz, R. Schmitz, B. Hendriks, and S. De Zwart, "Description of the influence of charging on the measurement of the secondary electron yield of mgo," *Applied surface science*, vol. 111, pp. 259–264, 1997.

[58] J. Scholtz, D. Dijkkamp, and R. Schmitz, "Secondary electron emission properties," *Philips journal of research*, vol. 50, no. 3-4, pp. 375–389, 1996.

[59] Y. Raitses, L. Dorf, A. Litvak, and N. Fisch, "Plume reduction in segmented electrode hall thruster," *Journal of Applied Physics*, vol. 88, no. 3, pp. 1263–1270, 2000.

[60] A. Dunaevsky, Y. Raitses, and N. Fisch, "Secondary electron emission from dielectric materials of a hall thruster with segmented electrodes," *Physics of Plasmas*, vol. 10, no. 6, pp. 2574–2577, 2003.

[61] C. Ordonez, "Fully kinetic plasma-sheath theory for a cold-electron emitting surface," *Physics of Fluids B: Plasma Physics*, vol. 4, no. 4, pp. 778–783, 1992.

[62] S. Langendorf and M. Walker, "Effect of secondary electron emission on the plasma sheath," *Physics of Plasmas*, vol. 22, no. 3, p. 033515, 2015.

[63] L. Oksuz and N. Hershkowitz, "Plasma, presheath, collisional sheath and collisionless sheath potential profiles in weakly ionized, weakly collisional plasma," *Plasma Sources Science and Technology*, vol. 14, no. 1, p. 201, 2005.

[64] L. Schiesko, M. Carrère, G. Cartry, and J.-M. Layet, "Experimental study and modeling of the electron-attracting sheath: the influence of secondary electron emission," *Physics of Plasmas*, vol. 15, no. 7, p. 073507, 2008.

[65] C. Jin, A. Ottaviano, and Y. Raitses, "Secondary electron emission yield from high aspect ratio carbon velvet surfaces," *Journal of Applied Physics*, vol. 122, no. 17, p. 173301, 2017.

[66] Z. S. Hartwig, H. S. Barnard, R. C. Lanza, B. N. Sorbom, P. W. Stahle, and D. G. Whyte, "An in situ accelerator-based diagnostic for plasma-material interactions science on magnetic fusion devices," *Review of Scientific Instruments*, vol. 84, no. 12, p. 123503, 2013.

[67] G. Federici, C. H. Skinner, J. N. Brooks, J. P. Coad, C. Grisolia, A. A. Haasz, A. Hassanein, V. Philipps, C. S. Pitcher, J. Roth *et al.*, "Plasma-material interactions in current tokamaks and their implications for next step fusion reactors," *Nuclear Fusion*, vol. 41, no. 12, p. 1967, 2001.

[68] D. Dickstein, H.-Y. Chang, J. Marian, M. Feldman, A. Hubble, R. Spektor, and N. Ghoniem, "Secondary electron emission from reticulated cellular copper surfaces," *Journal of Applied Physics*, vol. 128, no. 12, p. 123302, 2020.

[69] M. B. Mitchell Hall, Denver Schaffarzick Pacifica, "Erg aerospace corporation duocel foam manufacturing," 10920299 Nov 9 2019.

[70] V. S. Deshpande and N. A. Fleck, "Isotropic constitutive models for metallic foams," *Journal of the Mechanics and Physics of Solids*, vol. 48, no. 6-7, pp. 1253–1283, 2000.

[71] C. Körner and R. F. Singer, "Processing of metal foams—challenges and opportunities," *Advanced Engineering Materials*, vol. 2, no. 4, pp. 159–165, 2000.

[72] H. Suzuki, N. Matsunami, H. Sugai *et al.*, "In-situ measurements of secondary electron emission coefficient in plasma surface interaction," *Annual Report of National Institute for Fusion Science*, p. 89.

[73] J. Cazaux, "Calculated influence of work function on se escape probability and secondary electron emission yield," *Applied Surface Science*, vol. 257, no. 3, pp. 1002–1009, 2010.

[74] M. Furman and M. Pivi, "Probabilistic model for the simulation of secondary electron emission," *Physical review special topics-accelerators and beams*, vol. 5, no. 12, p. 124404, 2002.

[75] H. Seiler, "Secondary electron emission in the scanning electron microscope," *Journal of Applied Physics*, vol. 54, no. 11, pp. R1–R18, 1983.

[76] O. Hachenberg and W. Brauer, "Secondary electron emission from solids," in *Advances in electronics and electron physics*. Elsevier, 1959, vol. 11, pp. 413–499.

[77] M. Patino, Y. Raitses, and R. Wirz, "Electron emission from nano and microstructured materials for plasma applications," in *APS Annual Gaseous Electronics Meeting Abstracts*, 2016, pp. QR2–003.

[78] C. Swanson and I. D. Kaganovich, "Modeling of reduced effective secondary electron emission yield from a velvet surface," *Journal of Applied Physics*, vol. 120, no. 21, p. 213302, 2016.

[79] M. Patino, Y. Raitses, B. E. Koel, and R. Wirz, "Analysis of secondary electron emission for conducting materials using 4-grid leed/aes optics," *Journal of Physics D: Applied Physics*, vol. 48, no. 19, p. 195204, 2015.

[80] P. Palmberg, "A combined esca and auger spectrometer," *Journal of Vacuum Science and Technology*, vol. 12, no. 1, pp. 379–384, 1975.

[81] C. Körner and R. F. Singer, "Processing of Metal Foams Ð Challenges and Opportunities," Tech. Rep.

[82] D. K. Rajak, M. Gupta, D. K. Rajak, and M. Gupta, "Manufacturing methods of metal foams," *An Insight Into Metal Based Foams: Processing, Properties and Applications*, pp. 39–52, 2020.

[83] Randy and Randy, "Operation and calibration procedures," Mar 2023. [Online]. Available: https://www.rbdinstruments.com/blog/category/operation-and-calibration-procedures/

[84] T. Matlock, D. Goebel, R. Conversano, and R. Wirz, "A dc plasma source for plasma–material interaction experiments," *Plasma Sources Science and Technology*, vol. 23, no. 2, p. 025014, 2014.

[85] G. Z. Li, T. S. Matlock, D. M. Goebel, C. A. Dodson, C. S. Matthes, N. M. Ghoniem, and R. E. Wirz, "In situ plasma sputtering and angular distribution measurements for structured molybdenum surfaces," *Plasma Sources Science and Technology*, vol. 26, no. 6, p. 065002, 2017.

[86] W. Gekelman, P. Pribyl, Z. Lucky, M. Drandell, D. Leneman, J. Maggs, S. Vincena, B. Van Compernolle, S. Tripathi, G. Morales *et al.*, "The upgraded large plasma device, a machine for studying frontier basic plasma physics," *Review of Scientific Instruments*, vol. 87, no. 2, p. 025105, 2016.

[87] R. Wirz *et al.*, "Electron and ion induced electron emission from volumetrically complex materials for plasma facing surfaces," *Bulletin of the American Physical Society*, 2022.

[88] S. Barengolts, G. Mesyats, and M. Tsventoukh, "The ecton mechanism of unipolar arcing in magnetic confinement fusion devices," *Nuclear Fusion*, vol. 50, no. 12, p. 125004, 2010.

[89] A. Ottaviano and R. Wirz, "Secondary electron emission and arcing from volumetrically complex materials," in *APS Division of Plasma Physics Meeting Abstracts*, vol. 2021, 2021, pp. PP11–036.

[90] E. Everson, S. Vincena, and T. Carter, "Bapsflib: An open-source python package for the basic plasma science facility," in *APS Division of Plasma Physics Meeting Abstracts*, vol. 2020, 2020, pp. JM10–004.

[91] E. Barnat, G. Laity, and S. Baalrud, "Response of the plasma to the size of an anode electrode biased near the plasma potential," *Physics of Plasmas*, vol. 21, no. 10, p. 103512, 2014.

[92] M. J. Assael, A. Kalyva, S. Monogenidou, M. L. Huber, R. A. Perkins, D. G. Friend, and E. F. May, "Reference values and reference correlations for the thermal conductivity and viscosity of fluids," *Journal of physical and chemical reference data*, vol. 47, no. 2, p. 021501, 2018.

[93] E. W. Lemmon, I. H. Bell, M. Huber, and M. McLinden, "Nist standard reference database 23: reference fluid thermodynamic and transport properties-refprop, version 10.0, national institute of standards and technology," *Standard Reference Data Program, Gaithersburg*, 2018.

[94] J. Brooks, T. Sizyuk, J. Elder, T. Abrams, A. Hassanein, D. Rudakov, and W. Wampler, "Modeling, analysis, and code/data validation of DIII-D tokamak divertor experiments on ELM and non-ELM plasma tungsten sputtering erosion," *iopscience.iop.org*, 2020. [Online]. Available: https://doi.org/10.1088/1741-4326/abb39c

[95] A. Alba, R. Aguilar-Ponce, J. V.-G. .... C. o. A. ..., and undefined 2012, "Phase correlation based image alignment with subpixel accuracy," *Springer*. [Online]. Available: https://link.springer.com/chapter/10.1007/978-3-642-37807-2_15

[96] M. Boshtayeva, D. Hafner, J. W. P. Recognition, and undefined 2015, "A focus fusion framework with anisotropic depth map smoothing," *Elsevier*. [Online]. Available: https://www.sciencedirect.com/science/article/pii/S0031320314003987

[97] C. T. Jr, T. Biewer, L. B. R. o. S. ..., and undefined 2016, "Design of a digital holography system for PFC erosion measurements on Proto-MPEX," *aip.scitation.org*. [Online]. Available: https://aip.scitation.org/doi/abs/10.1063/1.4960488

[98] A. Eksaeva, D. Borodin, materials, J. R. N. ..., and undefined 2019, "Surface roughness effect on Mo physical sputtering and re-deposition in the linear plasma device PSI-2 predicted by ERO2. 0," *Elsevier*. [Online]. Available: https://www.sciencedirect.com/science/article/pii/S2352179118302679

[99] J. Coenen, G. Arnoux, B. Bazylev, G. Matthews, A. Autricque, I. Balboa, M. Clever, R. Dejarnac, I. Coffey, Y. Corre, S. Devaux, L. Frassinetti, E. Gauthier, J. Horacek, S. Jachmich, M. Komm, M. Knaup, K. Krieger, S. Marsen, A. Meigs, P. Mertens, R. Pitts, T. Puetterich, M. Rack, M. Stamp, G. Sergienko, P. Tamain, V. Thompson, and J.-e. Contributors, "ELM-induced transient tungsten melting in the JET divertor Related content," *Nuclear Fusion*, p. 023010, 2015. [Online]. Available: http://iopscience.iop.org/0029-5515/5310/104002.

[100] R. B. Lobbia and B. E. Beal, "Recommended practice for use of langmuir probes in electric propulsion testing," *Journal of Propulsion and Power*, vol. 33, no. 3, pp. 566–581, 2017.

[101] Y. Yamamura, "Theory of sputtering and comparison to experimental data," *Nuclear Instruments and Methods in Physics Research*, vol. 194, no. 1-3, pp. 515–522, 1982.

[102] B. Billiot, F. Cointault, L. Journaux, J.-C. Simon, and P. Gouton, "3D Image Acquisition System Based on Shape from Focus Technique," *Sensors*, vol. 13, pp. 5040–5053, 2013. [Online]. Available: www.mdpi.com/journal/sensorsArticle

[103] S. Nayar, Y. N. I. T. on Pattern, and undefined 1994, "Shape from focus," *ieeexplore.ieee.org*. [Online]. Available: https://ieeexplore.ieee.org/abstract/document/308479/

[104] ——, "Shape from focus," *ieeexplore.ieee.org*. [Online]. Available: https://ieeexplore.ieee.org/abstract/document/308479/

[105] W. Hu, S. Dai, A. Kirschner, , D. W. N. M. Energy, and undefined 2017, "Surface roughness effects on plasma near a divertor plate and local impact angle," *Elsevier*. [Online]. Available: https://www.sciencedirect.com/science/article/pii/S2352179116300631

[106] I. H. Hutchinson, "Principles of plasma diagnostics," *Plasma Physics and Controlled Fusion*, vol. 44, no. 12, p. 2603, 2002.

[107] A. Malik, T. C. P. Recognition, and undefined 2008, "A novel algorithm for estimation of depth map using image focus for 3D shape recovery in the presence of noise," *Elsevier*. [Online]. Available: https://www.sciencedirect.com/science/article/pii/S0031320308000058

[108] M. G. Gustafsson, "Surpassing the lateral resolution limit by a factor of two using structured illumination microscopy," *Journal of Microscopy*, vol. 198, no. 2, pp. 82–87, 2000.

[109] C. E. Thomas, R. Kaita, L. Baylor, S. Meitner, E. M. Granstedt, R. Kaita, R. Majeski, L. R. Baylor, S. J. Meitner, and S. K. Combs, "High-speed digital holography for neutral gas and electron density imaging Experimental Plasma physics, particle fuelling in the TJ-II Stellarator View project Reflectance polarization characterization of imaged samples View project High-speed digital holography for neutral gas and electron density imaging High-speed digital holography for neutral gas and electron density imaging," *Article in Review of Scientific Instruments*, vol. 87, no. 5, p. 53507, may 2016. [Online]. Available: http://dx.doi.org/10.1063/1.4949505http://scitation.aip.org/content/aip/journal/rsi/87/5?ver=pdfcov

[110] G. Li, "UCLA UCLA Electronic Theses and Dissertations Title Plasma Sputtering Behavior of Structured Materials," Tech. Rep., 2020. [Online]. Available: https://escholarship.org/uc/item/21s7b8v4

[111] V. H. Chaplin, M. Konopliv, T. Simka, L. K. Johnson, R. B. Lobbia, and R. E. Wirz, "Insights from collisional-radiative models of neutral and singly-ionized xenon in hall thrusters," in *AIAA Propulsion and Energy 2021 Forum*, 2021, p. 3378.

[112] G. Sabiston and R. Wirz, "Volumetrically complex materials for reducing electric propulsion facility effects," in *International Electric Propulsion Conference*. ERPS, 2022, p. 594.

[113] A. Thuppul, *Plasma-Material Interactions for Electric Propulsion and Plasma-Facing Components*. University of California, Los Angeles, 2022.

[114] A. L. C. G. S. G. W. S. V. T. L. P. T. J. G. P. P. T. C. R. E. W. Angelica Ottaviano, Mary F Konopliv, "Electron emission and arc behavior of plasma-robust volumetrically complex materials (vcms)," in *APS Division of Plasma Physics Meeting Abstracts*, vol. 2022, 2022, pp. PP11–036.

[115] R. Wirz, G. Wan, G. Sabiston, M. Konopliv, A. Thuppul *et al.*, "Persistent sputtering yield reduction in plasma-infused materials for plasma propulsion and fusion," *Bulletin of the American Physical Society*, 2022.

[116] S. C. Hsu, "Us fusion energy development via public-private partnerships," *Journal of Fusion Energy*, vol. 42, no. 1, p. 12, 2023.

[117] S. Smolentsev, T. Rhodes, Y. Jiang, P. Huang, and C. Kessel, "Status and progress of liquid metal thermofluids modeling for the us fusion nuclear science facility," *Fusion Science and Technology*, vol. 77, no. 7-8, pp. 745–760, 2021.

[118] Y. Yamamura and S. Shindo, "An empirical formula for angular dependence of sputtering yields," *Radiation effects*, vol. 80, no. 1-2, pp. 57–72, 1984.

[119] W. Möller and W. Eckstein, "Tridyn—a trim simulation code including dynamic composition changes," *Nuclear Instruments and Methods in Physics Research Section B: Beam Interactions with Materials and Atoms*, vol. 2, no. 1-3, pp. 814–818, 1984.